A new crustal fault formed the modern Corinth Rift

David Fernández-Blanco, Gino de Gelder, Robin Lacassin and Rolando Armijo

Université de Paris, Institut de physique du globe de Paris, CNRS, F-75005 Paris, France

A new crustal fault formed the modern Corinth Rift

David Fernández-Blanco, Gino de Gelder, Robin Lacassin and Rolando Armijo

Université de Paris, Institut de physique du globe de Paris, CNRS, F-75005 Paris, France

Abstract

This review shows how collective analysis of morphotectonic elements on uplifting rift margins can constrain the mechanical behaviour of continents during early rifting. This is shown for the modern Corinth Rift, one of the fastest-extending and most seismically active continental regions worldwide. We reconstruct the growth of the normal fault system that accommodates most of the rift strain and the uplift of the rift margin it bounds, from onset to present and at rift scale. Our approach allows first-order inferences on the mechanics and evolution of the rift, and can be used in other areas of early continental rifting.

We review and re-assess known geologic evidence in the Corinth Rift, and compile morphotectonic elements into a new map. We analyse the rift topo-bathymetry, and the footwall relief, river catchments and tectonic knickpoints in its uplifting margin. We also review studies that constrain the growth of normal faults using morphotectonic elements in their footwall, and propose a novel theoretical framework to reconstruct fault time-evolution during early rifting. We couple known and new data to derive fault displacement profiles in time, and use the theoretical framework to infer the history of growth and linkage of rift border faults, in turn constraining rift growth mechanics and evolution.

Our rift-scale morphotectonic investigation shows that the current rift-bounding faults are kinematically coherent at depth and constitute a fault >80 km in length. This composite master fault grew along-strike from the rift centre, linking and integrating individual fault segments that developed co-linearly at earlier times. The observed fault elastic flexure, footwall relief wavelength and high uplift and slip rates throughout the rift margin suggest the border fault is steep and highly localized in strain, and transects the entire seismogenic layer growing in a long-term strong elastic lithosphere.

Integration of previous and our new findings suggest the Corinth Rift evolved in two distinct extensional phases. These extensional phases are delimited by the fast, overwriting growth of the new rift-forming fault, that switched rift mechanics in a ~300 kyr timespan, and controls rift evolution thereafter. The new rift-forming fault enlarges the modern rift as an asymmetric half-graben, along and across strike, superimposed onto the preceding ~4 My distributed extension.

Keywords: Continental rift; Normal fault; Extensional footwall; Footwall uplift; Fault mechanics; Morphotectonics

1 Introduction

The kinematics, spatial distribution and geometry of normal faults control the mechanics and evolution of intracontinental rifts, as defined by the strength of the continental lithosphere. In continents, the thickness and rheological strength of lithospheric layers set the dip and geometry of normal faults (Buck, 1991, 1993; Brun, 1999; Gueydan et al., 2008), and the seismogenic thickness and effective elastic thickness of the crust regulate the maximum fault slip and along-axis segmentation of the resulting asymmetric grabens (Scholz and Contreras, 1998). Concurrently, the kinematics, spatial distribution, and geometry at depth of normal faults, expressed as footwall uplift and uplift rate, control the maximum elevation and morphology of mountain fronts (Wallace, 1978; Armijo et al., 1986, 1991), as well as the presence, geometry and wavelength of footwall up-warping (King and Ellis, 1990; Resor and Pollard, 2012; De Gelder et al., 2019). Normal border faults also control footwall relief, fluvial catchment drainage area and spacing (Densmore et al., 2004, 2005; Cowie et al., 2006), and the distribution and height of river long-profile convexities (e.g., Boulton and Whittaker, 2009; Kent et al., 2016; Gallen and Wegmann, 2017). It follows that morphotectonic elements in extensional footwalls record the growth of border faults and have the potential to characterise rift mechanics and evolution, and thus to provide insights into continental lithospheric behaviour to a first order.

Intracontinental rift mechanics can be generally abridged as two end-members (Fig. 1). High-angle faults commonly accommodate extensional strain at early stages of continental rifting (Bell et al., 2017), in an overall-strong lithosphere with the largest rheological strength in the lower crust or upper lithospheric mantle (Fig. 1A) (De Gelder et al., 2019). Contrarily, low-angle faults commonly tend to occur at late stages of rifting due to rotation by continued stretching (e.g., Jackson and McKenzie, 1983; Buck, 1993) in an overall-weak lithosphere with maximum strength in the upper crust (Fig. 1B) (Brun, 1999; Burov and Watts, 2006; Gueydan et al., 2008). Exceptionally, low-angle faults can occur during early rifting by magmatism or presence of favouring inherited structures (Bell et al., 2017 and references therein). Both faulting mechanisms have been proposed to accommodate rifting in tensionally-stressed, continental regions like the Basin and Range (e.g., Allmendinger et al., 1983; Stein and Barrientos, 1985), East African Rift (e.g., Ebinger, 1989; Morley, 1989), Baikal Rift (e.g., Mats, 1993; van der Beek, 1997), Central Apennines (e.g., Ghisetti and Vezzani, 1999; Boncio and Lavecchia, 2000) and the Corinth Rift (e.g., Armijo et al., 1996; Sorel, 2000).

Figure 1

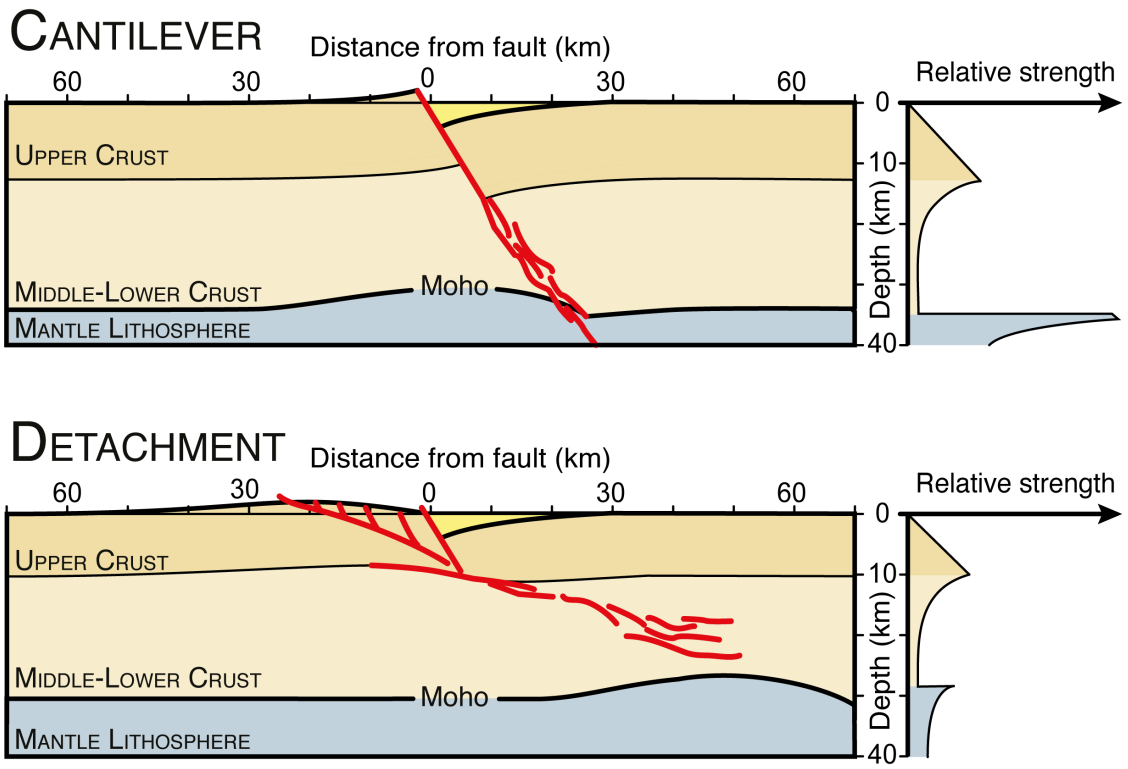

Fig. 1 *End-member models for intracontinental rifts and representative strength profiles. In the upper section is the flexural-cantilever rift model (Kusznir et al., 1991), and in the lower section is the core complex-detachment rift model (Buck, 1991). Their representative strength profiles are shown to the right of each model.*

The asymmetric continental rift of Corinth is young and amagmatic, and studies have reported both high- and low-angle faults transecting nearly orthogonally the pre-existing structural grain of the thickened Hellenic orogenic wedge (e.g., Armijo et al., 1996; Flott. and Sorel, 2001). The rift is one of the fastest extending regions accessible on land worldwide and one of the most seismically active (e.g., Dan McKenzie, 1978; Collier and Dart, 1991; Papazachos et al., 1992; Armijo et al., 1996; Avallone et al., 2004; Bernard et al., 2006; Leeder et al., 2008; Jolivet et al., 2010; Charalampakis et al., 2014). Therefore, the Corinth Rift is an outstanding natural laboratory for intracontinental rifting and a key site to gain an enhanced understanding of normal fault mechanics and continental tectonics.

Models of mechanics and evolution in the Corinth Rift are diverse, despite an impressive volume of research that spans from the fifth century BC philosophical arguments on mythological attributions given to karstic features in the mountains south of the Corinth Gulf (Herodotus “History”; e.g., Clendenon, 2009) to present-day results of the IODP Expedition 381

in the gulf itself (McNeill et al., 2019). Models lack a coherent view on growth history, kinematics and mechanics of the latest, currently active, rift border fault system and its significance for the Corinth Rift and for generic rift growth processes. Reconstructing the growth of these rift-bounding faults is possible by assessing, collectively and at rift scale, well-preserved geomorphic strain markers that record rift margin uplift.

Here we constrain the modern Corinth Rift mechanics and evolution, analysing at rift-scale the growth of active, collinear faults that bound the rift southern margin. First, we review previous geologic knowledge, and reassess, (re)map and integrate geologic and morphotectonic data into a new map. Second, we analyse relief along and across the rift axis to characterize rift morphology and study its relation with rift geology. We then review approaches that use the geomorphology of extensional footwalls to constrain normal fault mechanics, and put forward a theoretical framework to reconstruct normal fault growth history during early rifting of continents. Finally, we correlate time-strain markers and tectonic knickpoints at rift margin scale. With all the above, we derive the kinematic evolution and along-strike sequence of growth of modern border faults in the rift, as well as rates, wavelength and amplitude of fault uplift. Data and interpretation are coherent with the growth of a new, high-angle, rift-scale border fault that controls and progressively develops the modern Corinth Rift atop antecedent extension.

2 Geologic background: Corinth Rift & proposed models

Progressive rollback of the downgoing African slab and concomitant southward migration of the Hellenic trench since ~30–45 Ma lead to widespread extension in NW Greece, in the Cyclades and W Turkey (e.g., Le Pichon and Angelier, 1981; Reilinger et al., 2009; Brun and Sokoutis, 2010; Jolivet and Brun, 2010; Jolivet et al., 2013; Brun et al., 2016). In N Greece, however, this extension is overwritten by younger, steep normal faults that are active at present and formed in relation to the westward propagation of the North Anatolian Fault (NAF) into the North Aegean Trough (NAT) (e.g., Armijo et al., 1999; Koukouvelas and Aydin, 2002). The age of stress change from older to younger faulting is unclear but can be broadly bracketed between 430 ka in the southwestmost NAT (Saporades Basin; Ferentinos et al., 2018) and ~4 Ma at the NAT front (Olympos-Ossa-Pelion Range; Lacassin et al., 2007). The Corinth Rift is located to the NE of the Hellenic subduction trench, to the NW of a south-arched bathymetric trough formed by a detachment of the Aegean Sea, and to the SW of the

southmost NW-SE-trending extensional trough of the NAF (Fig. 2). The rift, with an overall strike of N105°E, transects almost orthogonally the thickened continental crust of the Eocene-to-Miocene Hellenides nappes (e.g., Jacobshagen et al., 1978; Bonneau, 1984; Jolivet et al., 2010).

Figure 2

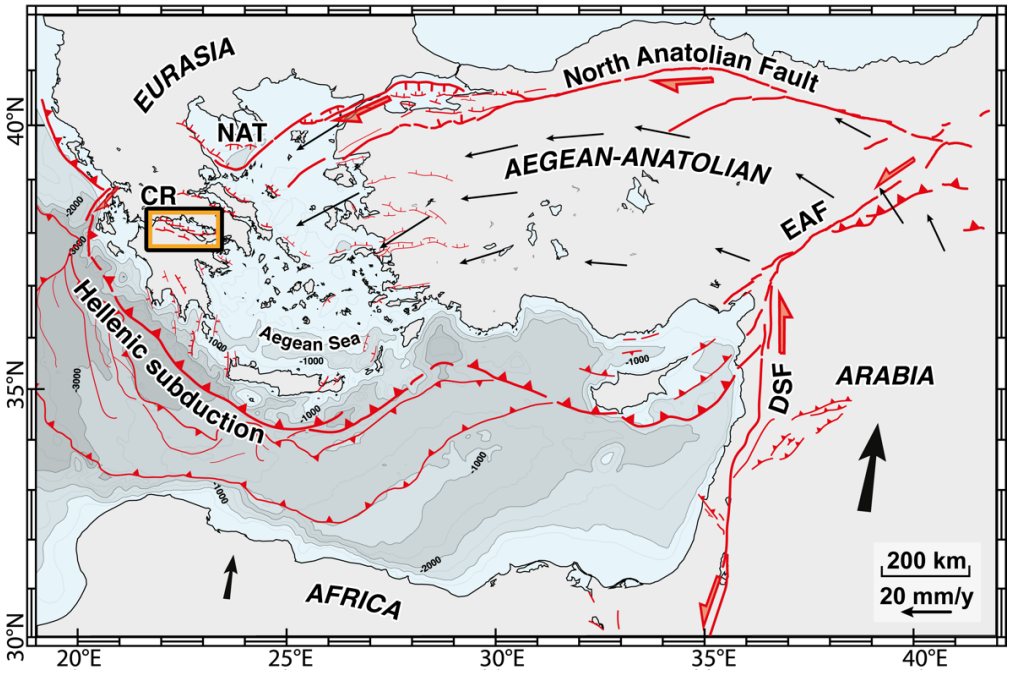

Fig. 2 *Active tectonic faults and GPS velocities of the W Turkey-Greece region. The map shows the main tectonic units, plate boundaries and active faults in the region, and the location of the Corinth Rift (CR). The bathymetry is modified from Huguen et al. (2004). The GPS vectors, with a fixed Eurasian Plate, are simplified from Le Pichon and Kreemer (2010). The map of active faults comes from Armijo et al. (1999) and Flerit et al. (2004) for the Aegean and North Anatolian areas, and Kreemer & Chamot-Rooke (2004) for the Mediterranean Ridge area. Line thickness and arrow size represent amount of slip to a first-order. NAF and EAF are the North and East Anatolian faults.*

Normal faults with overall north dips control the south coast of the Gulf of Corinth and govern present-day extension in the Corinth Rift (e.g., Doutsos and Piper, 1990). Rift border faults arranged in en-chelon segments ~10–25 km-long have a ~130 km cumulative length and along-rift strikes that vary from NE-SW to ENE-WSW in the easternmost rift to WNW-ESE to E-W in the central and west rift (Fig. 3). These active normal faults cut not only the Hellenic nappes at a high angle, but also a former set of normal faults with WNW-ESE trends that bounded (now exposed) Plio-Pleistocene basins (e.g., Collier et al., 1992; Armijo et al., 1996). These relationships are readable in the rift eastern end, where ESE-striking extensional faults bounding former depocenters are cross-cut by the younger fault system (e.g., Leeder et al.,

1991; Gawthorpe et al., 1994). Similar observations are not clear in the central and west rift, where both antecedent and presently active fault systems are sub-parallel to each other.

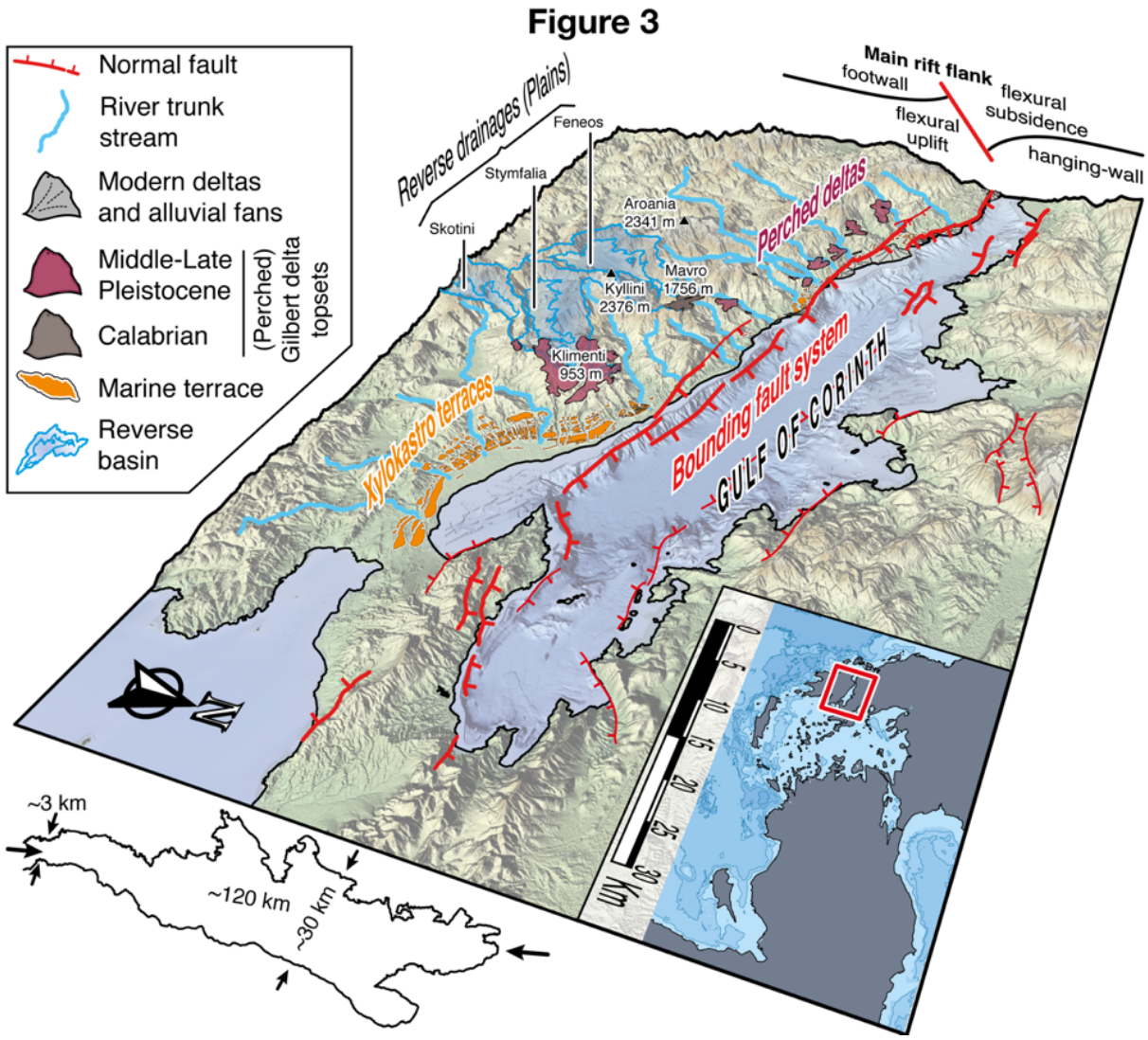

Fig. 3 *3D view of the Corinth Rift with representation of the main morphotectonic elements of the southern margin.*

Whereas active north-dipping rift-bounding faults set a markedly asymmetric half-graben in the rift center (e.g., Armijo et al., 1996; De Gelder et al., 2019), conjugate faults dipping south set more symmetric rift sectors at rift ends (e.g., Sakellariou et al., 1998, 2007; McNeill et al., 2005; Bell et al., 2011) (Fig. 3). The rift basin is broader and has its maximum basement subsidence at its centre where the whole-crust extension is greater (e.g., Bell et al., 2011), and the highest summits bound reversed, endorheic drainages (Fig. 3). Westwards along the rift axis, the wide, asymmetric half-graben changes into a symmetrical and narrow

graben, as the gulf width changes from ~30 km to ~3 km and its seafloor depth decreases from ~850 m to ~200 m (Fig. 3). By contrast, modern deltaic systems are significantly more developed in the west than in the rift centre (e.g., Seger and Alexander, 2009). Similarly, the extent of now-exposed marine Plio-Pleistocene rocks reduces westward (e.g., Ori, 1989), whereas syn-tectonic sedimentary wedges of the rift-bounding fault decrease in thickness (e.g., Nixon et al., 2016). In the same direction, overall fault orientations change from N105°E to N090°E and mean topography reduces by ~400 m. Rift morphology towards the east is more complex, for rift border faults change their orientation to N045°E-N055°E and the orientation of other faults is more variable (Fig. 3). Both east and west rift ends are highly active seismically (Jackson et al., 1982; Ambraseys and Jackson, 1990; Hubert et al., 1996; Bernard et al., 2006; Godano et al., 2014; Duverger et al., 2015).

2.1 Corinth Rift mechanical models

We discriminate proposed mechanical and evolutionary models for the Corinth Rift by two key characteristics: mechanics at depth and evolutionary continuity (Fig. 4). Despite the specificities of each model, we define mechanical models by proposed fault geometry at depth, and evolutionary models by proposed continuity between early distributed extension and the youngest, fastest rifting phase of highly localised strain.

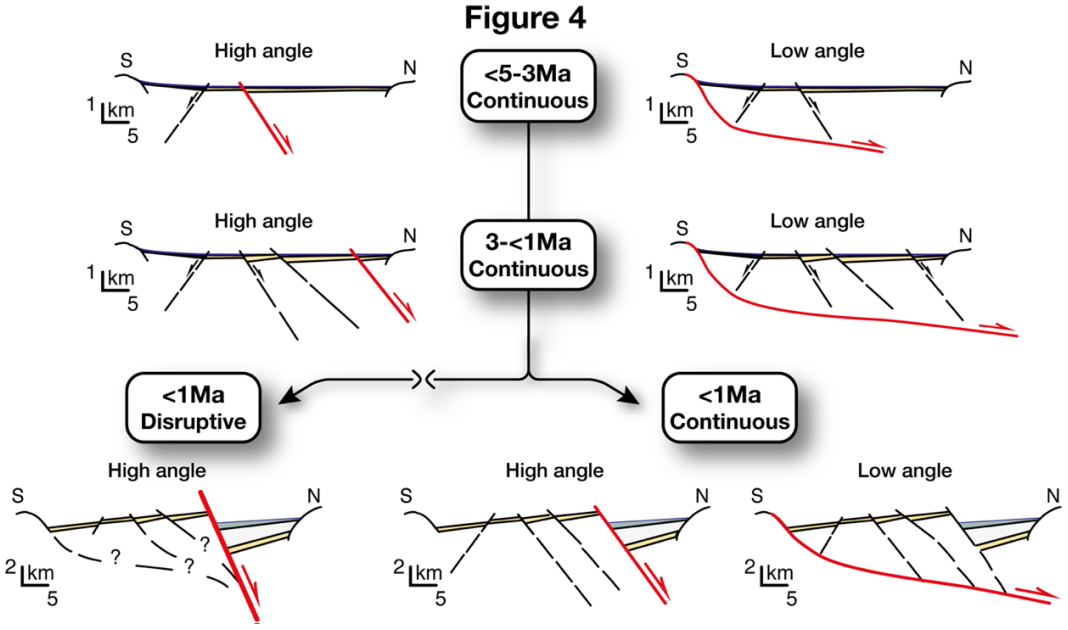

Fig. 4. *Types of models proposed for the Corinth Rift in time, when classified by two key characteristics: mechanics at depth and evolutionary continuity.*

2.1.1 High-angle faults: Evidence and models

High-angle planar faults predominate in the Corinth Rift (e.g., Jackson et al., 1982; Armijo et al., 1996). At present, extension is largely accommodated by faults that have dips of 40°-60° north and rupture the surface seismically during the Holocene, especially along the gulf southern coast (e.g., Hubert, 1996; Rigo et al., 1996; Stewart and Vita-Finzi, 1996). Whereas these active border faults lead to the rift marked asymmetry (Armijo et al., 1996), mostly-inactive faults located southwards also dip ~40°-60° north at the surface and delimit narrow tilted blocks with little footwall relief (Rohais et al., 2007; Bell et al., 2008; Ford et al., 2012). Individual faults imaged by offshore seismic studies are planar and remain steep at least until ~3 km depth (e.g., Taylor et al., 2011; Nixon et al., 2016) (Fig. 4).

In the east rift, border faults accommodate elastic flexure of lithosphere (elastic-plastic flexure *sensu stricto*, given inelastic strain above the brittle-ductile transition and plastic strain below it). Onshore-offshore strain markers accurately record elastic flexure at glacial-interglacial intervals (~120 ky; De Gelder et al., 2019) (Fig. 5A). Elastic flexure derived from these markers delineate an uplift/subsidence ratio of 1:1.2-2.4 along the SE rift margin (De Gelder et al., 2019) that agrees well with ratios of 1:1.2-2.2 estimated along the SW rift margin with geological features (McNeill et al., 2005). Coupled flexural footwall uplift south of the border faults (rates up to ~1.7±0.1 mm×yr^{-1} near the Xylokastro Fault) (Armijo et al., 1996; De Gelder et al., 2019) and flexural hanging-wall subsidence to their north (rates of ~3.6 mm×yr^{-1} in the gulf center) (Moretti et al., 2004) mark the ~4.8 km high-amplitude structural relief that exists in the rift centre-east in relation with the latest phase of faulting (Armijo et al., 1996; De Gelder et al., 2019) (Fig. 5A). This modern relief is in stark contrast with the antecedent "proto-gulf" low-amplitude relief inferred from stratigraphic data (e.g., Ori, 1989). The wavelength of elastic flexure in the east rift implies a high-angle (40°-60°) planar fault reaching the base of the seismogenic layer (Armijo et al., 1996; Bell et al., 2017; De Gelder et al., 2019).

Mechanical models derived from the data above propose the rift is controlled by elastic flexure along the border fault system since their onset (e.g., Armijo et al., 1996), probably by the Middle Pleistocene (Ford et al., 2016). The model is supported by the geometry of marine terraces, river catchments and topography (Armijo et al., 1996; De Gelder et al., 2019; Fernández-Blanco et al., 2019b) (Fig 5A), and the distribution of large earthquakes in the east and west rift with focal mechanisms that indicate normal faulting at 40°-60° angles (e.g., Jackson et al., 1982; King et al., 1985; Lyon-Caen et al., 2004). High-angle faulting is similarly supported by the correlation between observations of basement subsidence and crustal

thinning, and rift total extension, calculated by computing fault heaves under the assumption of planar faulting (McNeill et al., 2005; Bell et al., 2011; Ford et al., 2012). Moreover, finite-element models reproduce the vertical displacements and subsidence-uplift ratios observed in nature in simulations with high-angle planar faults reaching the brittle-ductile transition, but not in those with low-angle faults (Bell et al., 2017). Different seismic imaging methods show a minimum in regional Moho depths <30 km below the east and central gulf and elongated along axis (Zelt et al., 2005; Sachpazi et al., 2007; Pearce, 2015) that is coherent with the single, high-angle fault model (Fig. 5A).

2.1.2 Low-angle faults: Evidence and models

At the southern end of the rift margin, field observations led to the proposal of a low-angle fault (0° to 30°) dipping north at shallow depths (0-2km) (e.g., Sorel, 2000; Flotté and Sorel, 2001; Flotté et al., 2005) (Fig. 5B). These studies suggest that high-angle normal faults root into such low-angle detachment, interpreted to deepen northward from the surface to 2-3 km depth at the gulf southern coast, and proposed to be active from Pleistocene to Present. More recent research by Jolivet et al. (2010) considers the outcropping detachment as one of three decollements active before formation of border faults in the gulf southern coast (Fig. 5B). These studies extend the low-angle structure farther north into a microseismicity cloud imaged in the west rift (see below). Between the two sites, a low-angle basement fault compatible with the detachment has been interpreted in reflection seismics (Sachpazi et al., 2003; Taylor et al., 2011), although the structure is not mapped by other studies (Bell et al., 2008, 2009), even if using the same seismic lines (Nixon et al., 2016).

In the west rift, high-angle border faults seem to reach a ~2.5-km-thick microseismicity cloud that increases in depth from ~6 km with a gentle northward dip (10°-20°) (Rietbrock et al., 1996; Rigo et al., 1996; Lyon-Caen et al., 2004; Bernard et al., 2006; Gautier et al., 2006) (Fig. 5B). Whereas short-term microseismicity swarms in the upper ~2 km of the cloud may be controlled by pore-pressures in a highly-fractured, fluid-saturated geologic layer, long-term microseismicity in regular multiples located to its base may be explained by aseismic slip (Gautier et al., 2006; Duverger et al., 2015).

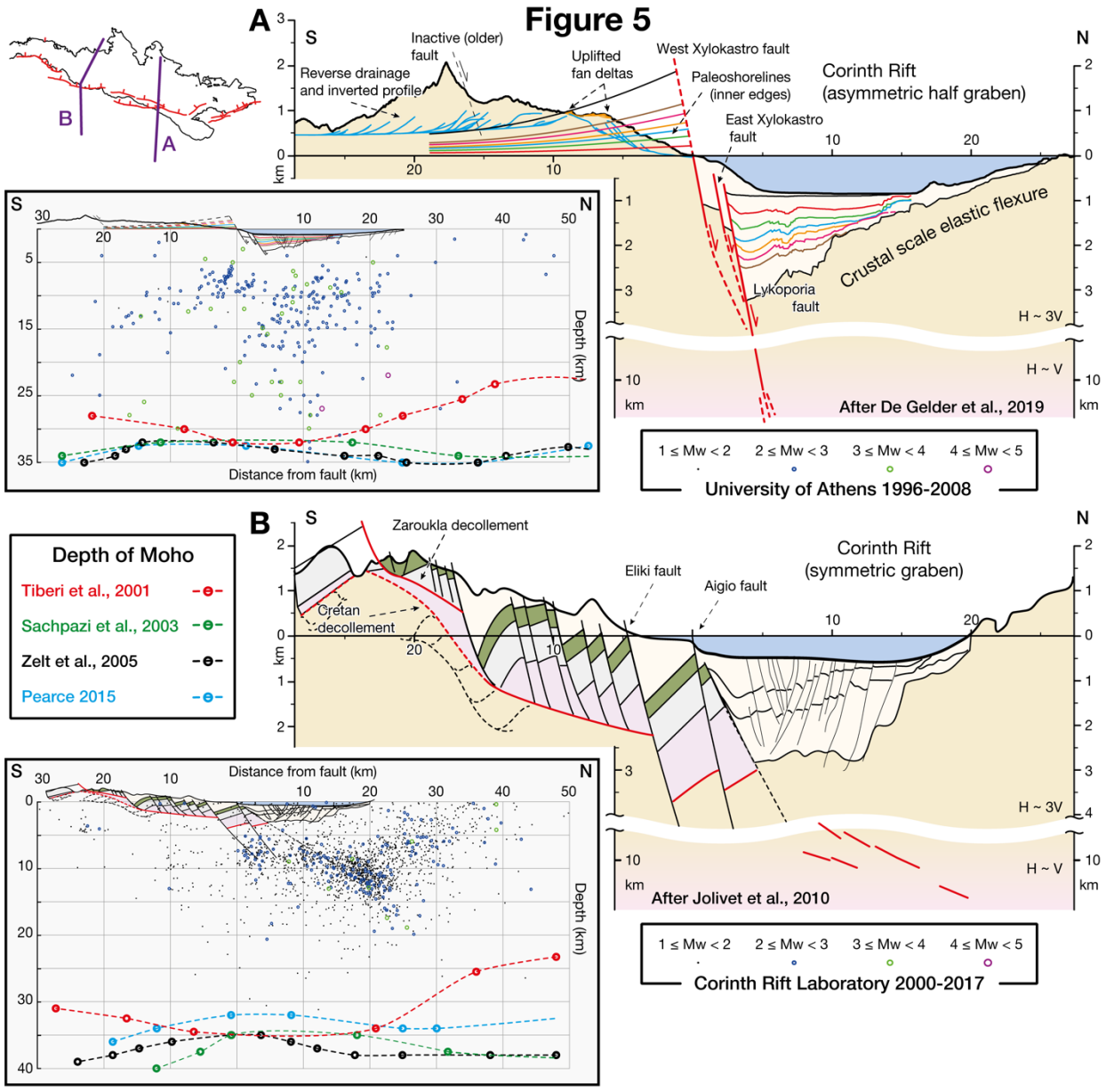

Fig. 5. *Cross sections across the **(A)** centre-east and **(B)** west sectors of the Corinth Rift. Sections are modified from De Gelder et al. (2019) and Jolivet et al. (2010) respectively, and scaled for direct comparison. The top 3-4km below the surface is exaggerated 3 times, and show the main elements as highlighted by the original studies. Notice the different set of elements and constraints used to reproduce each section. The bottom of the sections show the interpreted geometry of normal faults at the brittle-ductile transition at 1:1 scale. Fault geometry for (A) is proposed, and for (B) is shown as nodal planes of extensional focal mechanisms of large earthquakes that are parallel to the interpreted low-angle structure (as plotted in Jolivet el al., 2010). Panels at the bottom left of each section are crustal transects at 1:1 scale that extent the sections northward (~25 km). We use geophysical studies with maps of the Moho depth (Tiberi et al., 2001; Zelt et al., 2005; Sachpazi et al., 2007; Pearce, 2015) to derive Moho depth below each section, and plot seismicity along a 10 km-wide swath that is centered in the section. Seismicity data comes from the **(A)** 1996-2008 University of Athens and the **(B)** 2000-2017 Corinth Rift Laboratory seismic catalogues.*

Mechanical models derived from the data above propose the rift is controlled by the low-angle north-dipping structure and that high angle faults root and are mechanically linked to it (Fig. 5B). The structure is interpreted as a detachment, either related to the brittle-ductile transition (Hatzfeld et al., 2000) or to shear (e.g., Rigo et al., 1996; Sorel, 2000; Bernard et al., 2006), occurring along either an inherited crustal-scale detachment (Jolivet et al., 2010) or a local incipient detachment (Lambotte et al., 2014). Most of these studies consider that the structure transitions into the ductile middle crust, since seismicity is reduced below the microseismicity cluster (e.g., Duverger et al., 2015). Contrarily, active structures 1-2 km in length imaged at that depth are suggested to relate to significant strain (Lambotte et al., 2014). The low-angle fault models are supported by extensional focal mechanisms of large earthquakes in the west rift with one nodal plane parallel to the low-angle structure (e.g., Bernard et al., 1997) (Fig. 5B) and the weakening and fluid circulation usually associated with shallow-dipping detachments (e.g., Morrison and Anderson, 1998). A gravity inversion study, showing a shallower Moho north of the gulf (Tiberi et al., 2001), is also compatible with low angle fault models (Fig. 5B).

2.2 Evolutionary models for the Corinth Rift

Early distributed extension (e.g., Seger and Alexander, 2009; Gawthorpe et al., 2017b) and basinward fault migration (e.g., Gawthorpe et al., 1994; Goldsworthy and Jackson, 2001) occurred before the marked present-day strain localization that characterizes the modern Corinth Rift (e.g., Armijo et al., 1996; Hubert et al., 1996). Present-day extension rates in the rift are among the largest geodetic rates measured on any continental site (cf., Briole et al., 2000; Tetreault and Buiter, 2018), with GPS velocities increasing westward from ~11 $mm \times yr^{-1}$ in the Xylokastro area to ~16 $mm \times yr^{-1}$ in Aigion (e.g., Avallone et al., 2004). However, modern extension rates have increased by up to more than one order of magnitude since extension started (e.g., Ford et al., 2012) and geodetic data is at variance with finite strain and long-term average extension rates (e.g., Bell et al., 2011). These discrepancies, together with uncertainties over the age, (un)disruptive nature and overall tectonic relevance of the modern rift-bounding fault(s) leads to different rift evolutionary models (Fig. 4).

2.2.1 Evolutionary models of continuous rift development

The onset of distributed extension is poorly constrained to 3.6-5 Ma with radiometric dating of syn-extension volcanics in the east rift (Collier, 1990; Collier and Dart, 1991; Leeder et al.,

2008), and led to protected-setting continental and shallow water deposits (e.g., Gawthorpe et al., 2017a). In the southern flank of the modern rift, these deposits were uplifted in extensional footwalls that are sequentially younger northward, thereby recording basinward migration of normal faults and block tilting (e.g., Gawthorpe et al., 1994; Goldsworthy and Jackson, 2001; Ford et al., 2012).

Continuous rift models (Fig. 4) suggest self-organization of normal faults and progressive strain localization since the onset of distributed extension in a 20–30 km-wide area south of the present rift (e.g., Jolivet et al., 2010; Ford et al., 2016; Nixon et al., 2016; Gawthorpe et al., 2017b). In these models, increased rate and strain localization in the border fault system results from sequential rift development (e.g., Nixon et al., 2016). Continuous rift models frame the last faulting event within an undisrupted sequence of fault migration and block tilting in two-to-four continuous rift phases, i.e. the "Great Breaching" event at 0.6 Ma, within R2 phase starting at 2.2 to 1.8 Ma (Gawthorpe et al., 2017b); Phase 3 onset at 0.7±0.2 Ma (Ford et al., 2016); or Syn-rift 2 at 0.8 Ma (Rohais and Moretti, 2017). In these models, the rift evolves in response to retreat of the Hellenic slab and crustal collapse as an early form of a core complex similar to those in the Cyclades (Jolivet et al., 2010). For these models, the last faulting event is not necessarily indicative of a relevant kinematic change in response to large-scale tectonic boundary conditions (Jolivet, 2001).

2.2.2 Evolutionary models of disruptive, non-continuous rift development

Early distributed strain with low extensional rates (0.6–1 mm×yr^{-1}) (Ford et al., 2012) preceded the development of the modern, strain-localised border fault (Armijo et al., 1996). The onset of activity on the border fault is still disputed. Estimations based on lateral chrono-/bio-stratigraphic correlations of syn-extensional deposits in the uplifted margin give an upper boundary age of 2.2–1.8 Ma for fault initiation (Gawthorpe et al., 2017b). An age of ~1 Ma is derived from linear extrapolation of Late Pleistocene marine terraces (Armijo et al., 1996; De Gelder et al., 2019) and datation of calcite cements (Causse et al., 2004). Depositional ages (Rohais et al., 2007a, b; Ford et al., 2009, 2016) and U-Th dating of tufa (Brasier et al., 2011) in perched conglomeratic deltas onshore, and depocenter coalescence in the offshore (Nixon et al., 2016) give a lower boundary of ~0.7–0.6 Ma. Given the uncertainty involved in assigning chronostratigraphic significance to systems tracts when marked spatial variations in vertical motions exits (Gawthorpe et al., 2017a), we here consider an age between ~1 Ma and ~0.6 Ma for the onset of fault activity. Border fault growth marked a dramatic increase in subsidence

and a first-order switch in rift tectonostratigraphy, with a sharp sedimentation contrast both onland and in the offshore, and to a rift-scale angular unconformity (e.g., Ori, 1989; Sachpazi et al., 2003).

Disruptive, non-continuous rift models (Fig. 4) suggest a strongly-localized strain since border fault onset (De Gelder et al., 2019), and discriminate an early proto-Gulf from a modern Corinth Rift (Ori, 1989). Increased rates and strain localization results from disruptive growth of a new high-angle, rift-forming fault driving the elastic flexure along the rift margin (Ori, 1989; Armijo et al., 1996). Disruptive rift models frame the last faulting event as discontinuing comparatively minor antecedent extension, and controlling the rift geometry and most defining features thereafter (e.g., Armijo et al., 1996). In these models, the modern rift evolves in response to propagation of the NAF and lithospheric flexure, accommodating extension at the fault tip, much like those extensional throughs to the NE (Armijo et al., 1996, 1999). This evolution implies a marked kinematic change that disrupts previous extension in response to the process zone of the lithospheric-scale transform fault (Hubert-Ferrari et al., 2003; Flerit et al., 2004).

2.3 Implications

Different models imply different behaviour of the continental lithosphere below the rift (Fig. 1 & 5). Continuous low-angle detachment models assume combined shear (Barbier et al., 1986) in the rift, transiting eastwards to simple shear rifting (Wernicke, 1981) in the central Aegean. Continuous high-angle fault models infer pure shear rifting (McKenzie, 1978a) south of the present rift evolving to a flexural cantilever model (Kusznir et al., 1991) in its rift-bounding fault. Disruptive models infer a flexural cantilever rift that overwrites prior extension (whether pure or simple shear) at younger times, implying a temporal modern rift that is sustained by protracted seismicity (King et al., 1988).

3 The modern Corinth Rift

We compiled, reassessed and (re)mapped active tectonic, tectonomorphic and geologic information from 30+ suitable papers, compilation papers, and published maps into a new map at the scale of the rift (Fig. 6). We provide in the supplementary material a detailed account on the data used (Suppl. material A), a comparison with the map of offshore faults by Nixon et al. (2016) (Suppl. material B), as well as shapefiles and KML files (topobathymetric DEM, 5-level

hierarchy active faults, marine terraces, Gilbert-delta topsets, and river streams and catchments) (Suppl. material G to K).

We differentiate two rift sectors that correlate with the strike of the rift border fault system (Fig. 7). Whereas faults trend NE-SW to ENE-WSW in the "easternmost rift" (Perachora peninsula and offshore north of it), faults trend WNW-ESE to E-W in the "rift southern margin" (W of the Perachora peninsula). We further identify three footwall sectors in the rift southern margin, where we perform our analyses, using position and distance of the coast and main morphological elements from the active fault system; "east" (east of Kiato), "central" (from Kiato to Akrata) and "west" (from Akrata to Psathopyrgos) (Fig. 7). For the latter, we differentiated as needed between "E west" sector, related to the Eliki Fault Array (Eliki FA) and "westermost" sector, related to faults farther west. Hereon, we distinguish individual faults (F) from fault arrays (FA).

3.1 Active normal faults

Geomorphic markers uplifting in the footwall of individual border faults have been extensively studied, often to derive fault uplift and/or slip rates (e.g., Collier et al., 1992; Armijo et al., 1996; Stewart, 1996; Stewart and Vita-Finzi, 1996; Koukouvelas et al., 2001; Stefatos et al., 2002; Houghton et al., 2003; Leeder et al., 2003; McNeill and Collier, 2004; Pantosti et al., 2004; Pavlides et al., 2004; Verrios et al., 2004; Palyvos et al., 2005, 2007, 2008; Turner et al., 2010; Karymbalis et al., 2016b; De Gelder et al., 2019). Details on fault activity, slip and uplift rates derived by these studies were compiled by other studies (see Table 1 & 2 in Bell et al., 2009 and e.g., Collier et al., 1992; Armijo et al., 1996; Stewart, 1996; Stewart and Vita-Finzi, 1996; Koukouvelas et al., 2001; Stefatos et al., 2002; Houghton et al., 2003; Leeder et al., 2003; McNeill and Collier, 2004; Pantosti et al., 2004; Pavlides et al., 2004; Verrios et al., 2004; Palyvos et al., 2005, 2007, 2008; Turner et al., 2010; Karymbalis et al., 2016b; De Gelder et al., 2019), and the overarching findings follow.

Uplift and slip rate are maximum in the rift centre (CRFA, Fig. 7 & 8), minimum in the east rift and intermediate yet high in the west rift (AiFA, EkFA, Fig. 7 & 8). Upward elastic flexure along the rift margin led to uplift rates that range from up to 1.5-2 $mm \times yr^{-1}$ to ~0.2-0.3 $mm \times yr^{-1}$ (e.g., Collier et al., 1992; Armijo et al., 1996; Stewart and Vita-Finzi, 1996; Leeder et al., 2003; McNeill and Collier, 2004; Pavlides et al., 2004; Turner et al., 2010; Karymbalis et al., 2016b; De Gelder et al., 2019). Except in the east rift, these values markedly overpass a

regional uplift signal, estimated between 0 and 0.3 mm×yr^{-1} (e.g., Armijo et al., 1996; Turner et al., 2010). Fault slip rates inferred are also consistently high along the entire rift margin, with minima ranging from 4 mm×yr^{-1} (McNeill and Collier, 2004) to 7 mm×yr^{-1} (Armijo et al., 1996).

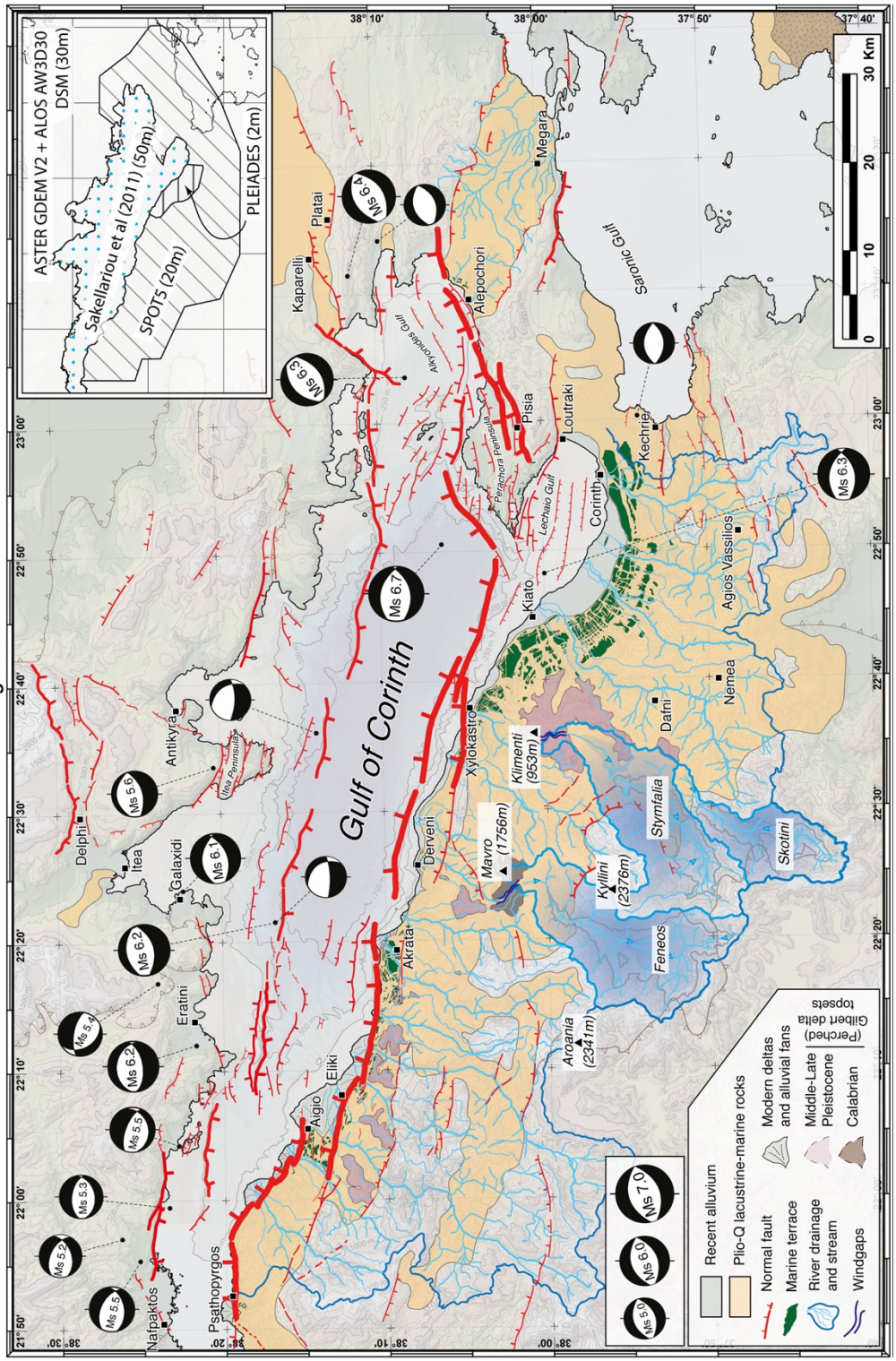

Figure 6

Fig. 6 (prev. page). *Tectonomorphologic and active tectonics map of the Gulf of Corinth. Based on a compilation, reassessment and remapping from 30+ contributions, and own mapping (see Suppl. material A). Inlet shows the different DEMs used for the topobathymetry.*

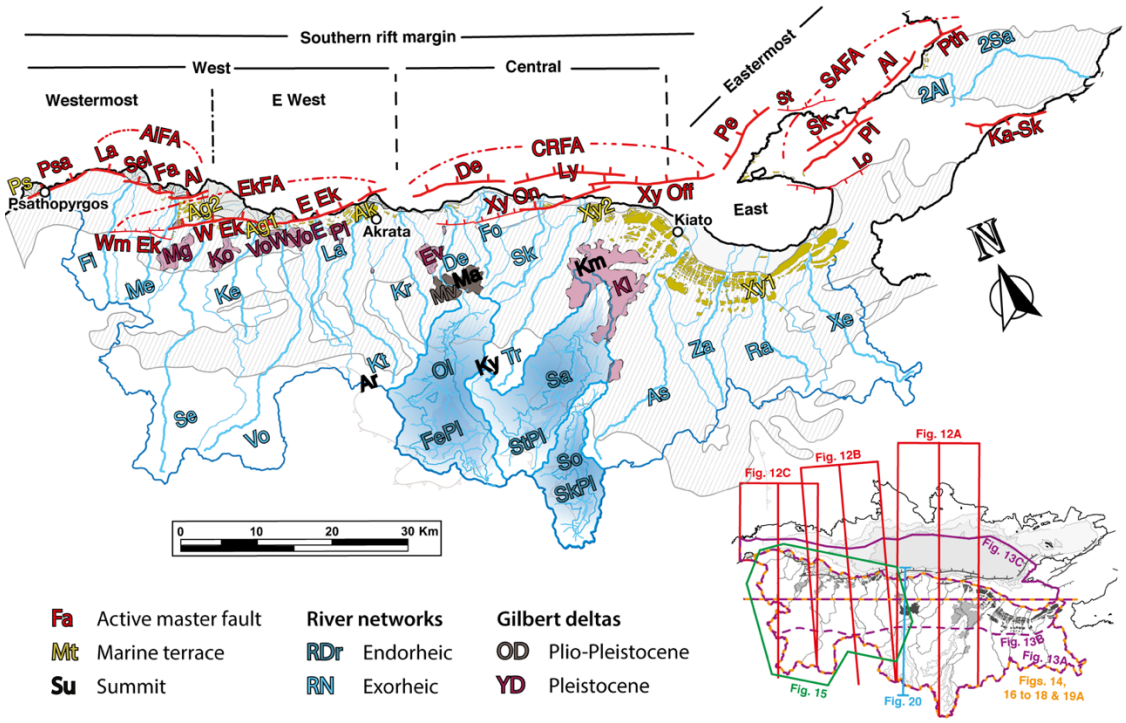

Fig. 7. *Index map, showing the main elements of the Corinth Rift considered in this review. The lower right inset shows the extent of the DEM for across-axis (red) and along-axis (purple) stacked swath profiles and their projection lines, as well as the location of other figures of the western rift (green), the full rift (orange), and cross sections (in blue). Abbreviation of the main elements, from east to west. Main active faults: Psatha (Pth); Kakia-Skala (Ka-Sk); Alepochori (Al) and Skinos (Sk); Strava (St); Pisia (Pi); Perachora (Pe); Loutraki (Lo); Central Rift Fault Array (CRFA) [composed of Xylokastro Onshore (Xy On), Xylokastro Offshore (Xy Off), Lykoporia (Ly) and Derveni (De)]; Eliki Fault Array (EkFA) [with the East Eliki (E Ek) and West Eliki (W Ek)]; and the Aigio Fault Array (AiFA) [inclusive of Aigio (Ai), Fasouleika (Fa), Selianitika (Sel), Lambiri (La) and Psathopyrgos (Psa)]. Marine terraces location: Xylokastro (Xy1 & Xy2), Akrata (Ak), Aigio (Ag1 & Ag2), and Psathopyrgos (Ps). Pleistocene perched Gilbert deltas: Klimenti (Kl), Evrostini (Ev), Platanos (Pl), Vouraikos East (VoE) and West (VoW), Kolokotronis (Ko) and Meganitis (Mg). Late Pliocene (perched) Gilbert delta: Mavro (Mv). Main drainage systems: Xerias (Xe), Raizanis (Ra), Zapantis (Za), Asopos (As), Trikalitikos (Tr), Fonissa (Fo), Skoupeiko (Sk), Dervenios (De), Krios (Kr), Krathis (Kt), Ladopotamos (La), Vouraikos (Vo), Kerinitis (Ke), Selinous (Se), Meganitis (Me) and Finikas (Ph). Internally drained basins and their plains: Soutini (So) and Skotini Plain (SkPl); Safenetos (Sa) and the Stymfalia Plain (StPl); and Olvios (Ol) and the Feneos plain (FePl). Main summits: Klimenti (Km) and Mavro (Ma) at the front and Kyllini (Ky) and Aroania (Ar) at the back.*

Fig. 8 (next page). *Map of Corinth Rift active faults with displaced relief.* ***(A)*** *Corinth Rift topobathymetry and the map of active faults. The topobathymetry is derived from a merged DEM, and the active faults map comes from own mapping and reassessment of fault maps from other contributions (see Suppl. material A).* ***(B)*** *Highlight of the three highest levels of our fault hierarchy.* ***(C)*** *Master fault (acronyms as in Fig. 7). In grey for all panels, a representation of a hypothetical composite master fault at seismogenic layer basal depths (~10 km) with similar high-angle north dips and planar attitudes than at-surface faults bounding the rift at present.*

Figure 8

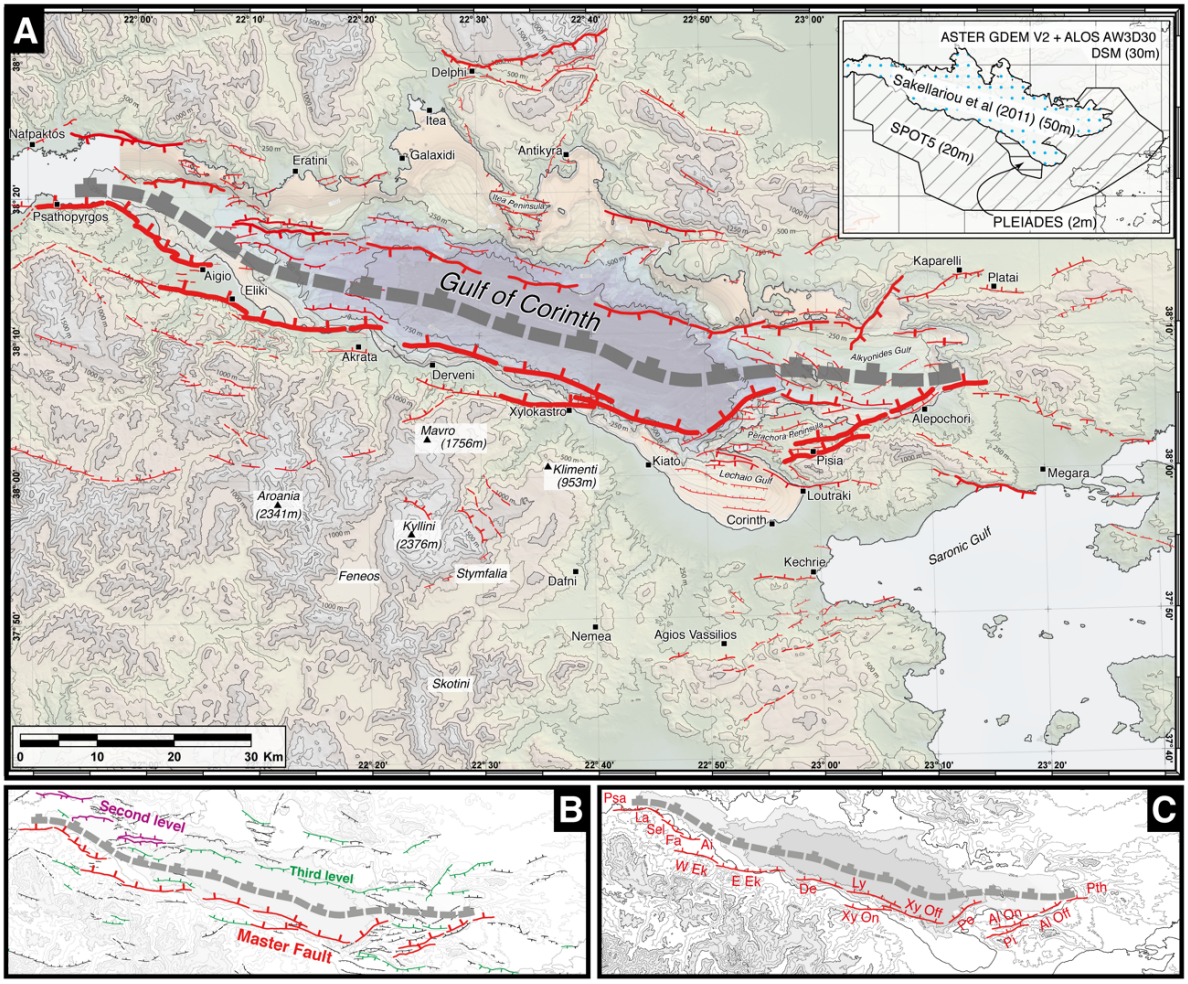

North of the border fault system, parallel faults dipping south and conjugate faults are kinematically linked to the border fault system and passively accommodate its motion (Fig. 8) (e.g., Stefatos et al., 2002). These smaller active faults are either synthetic or antithetic to the border fault and trend roughly parallel to it along most of the rift, or conjugate faults in the rift eastern and western terminus (Figs. 6 & 8). With the exception of faults in the westernmost rift (e.g., Beckers et al., 2015), these south-dipping faults develop smaller syntectonic sedimentary wedges that the border faults (e.g., Nixon et al., 2016). Among these faults, the system with largest offsets locates north of the bathymetric low and is composed of E-W trending faults with south dips. This fault set produces small reliefs and has no associated pattern of onshore uplift and offshore subsidence (e.g., Stefatos et al., 2002). In fact, the irregular northern coastline of the gulf (Fig. 6) is dominated by subsidence (Bell et al., 2009; Elias et al., 2009).

3.2 Uplifted Quaternary marine terraces

Sequences of uplifted marine terraces correlated to sea level highstands up to ~400 ka outcrop near the coast all along the rift-bounding fault footwall, from Alepochori to Psathopyrgos (Figs. 6, 7 & 9A). The best-developed marine terrace sequence outcrops in a ~6-8 km wide strip trending NW-SE, parallel to the gulf southern coast west of Corinth for ~40 km (Fig. 9A). This wave-cut marine terrace flight, carved into Plio-Pleistocene marls, is correlated to sea level highstands up to ~400 ka. It has large lateral variations NW-wards as distance to the master fault decreases from ~20 km to ~3 km; i.e. the marine terrace sequence increases in the number of levels, from a few-low laying levels in Kechrie to ~14 levels in the Onshore Xylokastro F footwall, and in elevation by a factor of 3-4, reaching as high as ~400 m (Armijo et al., 1996; De Gelder et al., 2019) (Figs. 6, 7 & 9A). The MIS 5e terrace at ~177 m is the highest of its age for the whole gulf (Fig. 9A).

In the west rift, marine terraces formed by wave erosion far from the outlets of major rivers, and depositional marine terraces developed at these locations over prograding delta fans (e.g., Hemelsdaël and Ford, 2016) (Figs. 6, 7 & 9A). Up to ten levels of relatively well-developed marine terraces with laterally consistent elevations of up to ~350 m lay along the coastline in the footwall of the West and East Eliki and Aigio faults (McNeill and Collier, 2004) (Figs. 6, 7 & 9A). The Eliki F footwall terraces show a relevant marine terrace sequence in Akrata that dims westwards. They outcrop typically within 5 km of the Eliki FA trace and their elevation varies westward from 135 to 150 m for MIS 5e level and from 240 to 255 m for the MIS 7e terrace (McNeill and Collier, 2004; for their preferred ~1.1 $mm \times yr^{-1}$ uplift rate) (Fig. 9A). Marine terraces lying between the Aigio F footwall and the hanging wall of the western sector of West Eliki F are at 160 m for MIS 5e, and 232 m for MIS 7e. Although a MIS 9 level at 360 m has been dated in the western sector of West Eliki F footwall, it is not confidently correlated laterally (De Martini et al., 2004). At the westernmost rift, seven narrow terrace levels reaching a maximum elevation of ~250 m are carved into the Plio-Pleistocene rocks of the Ps footwall, outcropping within 2 km of Ps trace, at ~90 m elevation (for MIS 5e) and ~160 m (for MIS 7e) (Houghton et al., 2003) (Figs. 6, 7 & 9A).

Figure 9

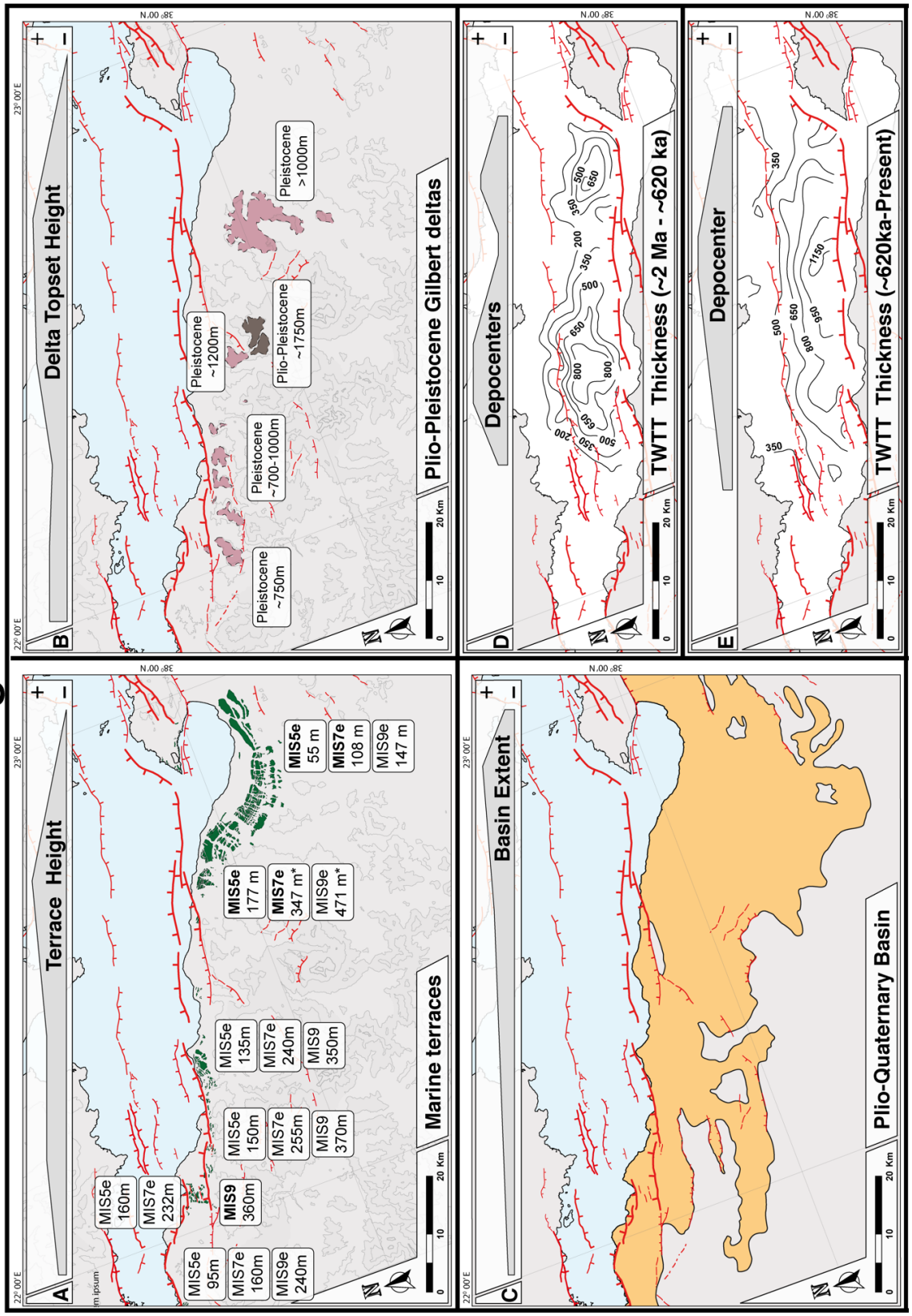
A
Terrace Height
MIS5e 160m
MIS7e 232m
MIS9 360m
MIS5e 95m
MIS7e 160m
MIS9e 240m
MIS5e 150m
MIS7e 255m
MIS9 370m
MIS5e 135m
MIS7e 240m
MIS9 350m
MIS5e 177 m
MIS7e 347 m*
MIS9e 471 m*
MIS5e 55 m
MIS7e 108 m
MIS9e 147 m
Marine terraces
B
Delta Topset Height
Pleistocene ~1200m
Plio-Pleistocene ~1750m
Pleistocene >1000m
Pleistocene ~700-1000m
Pleistocene ~750m
Plio-Pleistocene Gilbert deltas
C
Basin Extent
Plio-Quaternary Basin
D
Depocenters
TWTT Thickness (~2 Ma - ~620 ka)
E
Depocenter
TWTT Thickness (~620ka-Present)
22° 00'E
23° 00'E
38° 00'N
0
10
20 Km

Fig. 9 (prev. page). *Variations along the Corinth Rift axis, in map views highlighting different geologic elements. The main trend of each corresponding feature is shown schematically on top of each map.* ***(A)*** *The presence of known marine terraces, their estimated ages and elevations at six locations - bold highstands are dated levels, and the asterisks indicate elevations extrapolated in space to match the distance to the master fault of the MIS 5e terrace.* ***(B)*** *The presence and location of mapped topsets of Gilbert deltas, their age and rough elevations.* ***(C)*** *Extent of the Plio-Quaternary basin exposed onland.* ***(D)*** *and* ***(E)*** *Isochore maps showing two-ways travel times true vertical thickness for two seismic units, representing ~1.5-2 Ma to 620 ka, and 620 ka to Present, simplified from Nixon et al. (2016).*

3.3 Modern and perched Plio-Pleistocene Gilbert Deltas

Two families of coarse-grained Gilbert-type deltas with similar facies associations and geometries are differently distributed along the Corinth Rift southern flank (e.g., Seger and Alexander, 2009) (Figs. 6, 7 & 9B). Whereas Plio-Pleistocene deltas outcrop with varying angular unconformity atop of uplifted Plio-Pleistocene syn-rift and Hellenic basement rocks (e.g., Ori, 1989; Gawthorpe et al., 2017a), Holocene deltas lie in a narrow rim along the coast (Figs. 6 & 7). In the east rift, a large low lying plain passes seawards to a wide coastal platform in the absence of deltas (Figs. 6, 7 & 9B). In the rift center, prominent Plio-Pleistocene deltas display thick foresets packages (>700 m) at up to ~1750 m elevation, and down-step in stranded offlapping sequences that become younger towards the under-developed Modern deltas in the gulf shore (e.g., Rohais et al., 2007; Seger and Alexander, 2009). In the west rift, less-developed Plio-Pleistocene deltas crop out along a relatively continuous strip behind well-developed Modern deltas, which coalesce in a broad coastal delta plain (e.g., Ford et al., 2009, 2016) (Fig. 6). The shift in the locus of growth of large deltaic systems from the rift center in the Plio-Pleistocene to the west in the Holocene may relate with changes in master fault activity and differential footwall uplift or changes in sediment supply.

3.4 Plio-Pleistocene (uplifted) basin extent

The extent of the exposed Plio-Pleistocene basin decreases westward along the rift southern flank strike, from an extensive area ~35 km long to a couple of strips each <10 km long (Fig. 9C). In the east rift, the Plio-Pleistocene rocks cover a large area of low relief (Figs. 6 & 9C). Towards the central rift, the uplifted syn-rift deposits are reduced to an extent of ~20 km. Similarly, the modern progradational coastal area loses extent until it is very limited or not existent between the towns of Kiato and Derveni (Karymbalis et al., 2016a, 2016b) (Fig. 9). However, in the west rift, the extent of the Plio-Pleistocene rocks presently outcropping onland is reduced in comparison to areas farther east, and they outcrop in elongated WNW-ESE areas alternating with basement rocks (Fig. 9C). Father west, the extent of the Pliocene marine basin

is reduced to a stripe of several kilometers, i.e., smaller than anywhere else in the southern margin of the Corinth Rift (Fig. 9C).

3.5 Hanging wall synrift deposits

The rift basin is markedly asymmetric and dominated by the north dipping master fault system (e.g., Brooks and Ferentinos, 1984; Stefatos et al., 2002; Taylor et al., 2011), except at the basin ends, where antithetic faults are relevant (Fig. 8) (e.g., Hubert et al., 1996; Benedetti et al., 2003; McNeill et al., 2005; Bell et al., 2008). In the west, the transition from asymmetric to roughly symmetric is located around the area where East Eliki F crosses onland (e.g., Nixon et al., 2016), and albeit asymmetric, larger symmetry is also recognized in the eastern end of the rift basin (Sakellariou et al., 2007).

A rift-scale unconformity with an estimated age of ~620 ka, bounds two units with distinct seismic character that mark a change in setting from lacustrine to mixed marine/lacustrine; a unit with non-coherent reflectors below the unconformity, and a unit with rhythmical alternations of low-/high-amplitude reflectors above it (Sachpazi et al., 2003; Lykousis et al., 2007; Sakellariou et al., 2007; Bell et al., 2008, 2009; Taylor et al., 2011; McNeill et al., 2018). Synrift depocenters traced for both units (Fig. 9 in Nixon et al., 2016) mark a switch from a complex rift zone with distributed depocenters (Fig. 9D) to a markedly asymmetrical rift (Fig. 9E). This switch towards the present asymmetric rift may have taken place by establishment of the north dipping faults by ~620 ka and their later linkage by ~340 ka (Nixon et al., 2016). The upper unit is laterally continuous along the rift, with two exceptions; a second unconformity (~340 ka) exists in the west, and only the upper part of the sequence can be traced in the Alkyonides Gulf (Fig. 8) (e.g., Bell et al., 2008, 2009).

3.6 Topo-bathymetry

We analyse the morphology of the Corinth Rift in relation to its current bounding fault system, and its interrelation with geological and morphological elements, using stacked swath profiles of average topography. Stacked swath profiles (Armijo et al., 2015) are a suite of parallel swath profiles plot orthogonally to their strike. We use a 20-m DEM to derive stacked swath profiles that are either parallel or perpendicular to border faults (Fig. 7). See details on the procedure followed to produce the stacked swaths in Suppl. material C.

3.6.1 Across the rift axis

Topographic variations in the rift central sector are the largest for both the maximum and minimum topographic envelopes (red and blue in Fig. 10A). The central rift has the highest mean elevations, the highest summit (Killini, 2376 m) and the former basin outcropping at the highest location (Mavro, 1756 m). In the south, flat-laying and gently south-dipping endorheic basins (Feneos, Stymfalia y Skotini plains; Figs. 6 & 7) remain overall at similar mean elevations for horizontal distances of ~40 km. Here, maximum and minimum topography show similar mean elevations (of ~1650 m and of ~650 m, respectively) for similar horizontal distances (Fig. 10A). The northward decreasing relief contains Gilbert delta topsets at ~1100-1200 m (Evrostini) and ~900-1000 m (Klimenti) (Figs. 6 & 7) and reaches in 10-15 km bathymetric depths in excess of –800 m, as close as 2 km away from the shore (Fig. 10A). This represents a relief change of ~2.5 km in <15 km in the horizontal, or >3 km in <25 km, measured from the rift highest topography to its lowest bathymetry, i.e. a slope of ~9.5° or ~7°, respectively. Northwards, the flat basin floor lays at approx. –850 m for ~10 km and the gulf is the widest at sea level. The envelope of maximum relief in the northern margin rises from –750 m to ~1000 m in a rounded convex-up shape (Fig. 10A).

Fig. 10 (next page). *Topobathymetry across the Corinth Rift in three "views" perpendicular to the current rift-bounding fault. Each ~26 km wide swath is composed of 400 swath profiles, stacked over a projection line perpendicular to the average strike of the main fault in each sector (see below). The width of each individual swath is calculated dynamically and of ~75 m. Relief is exaggerated ~8 times. Distance along each wide swath is measured from the master fault (positive northwards).* ***(A)*** *Topobathymetry associated with the Central Rift FA in a view looking towards N295°E.* ***(B)*** *Topobathymetry associated with the Eliki FA as seen looking in a N290°E direction.* ***(C)*** *Topobathymetry associated with the Aigio FA in a view looking towards N290°E. In all views the upper envelope (red line) and the lower envelope (blue line) represent the maximum and minimum topobathymetry, respectively. Each individual sector of the master fault is shown with a 55° north dip in red. Other associated features are shown: rivers and endorheic basins (dim red); topsets of Gilbert deltas in light brown (Late Pliocene - Early Pleistocene), blue (Mid-Late Pleistocene); and yellow for modern Gilbert Deltas.*

Figure 10

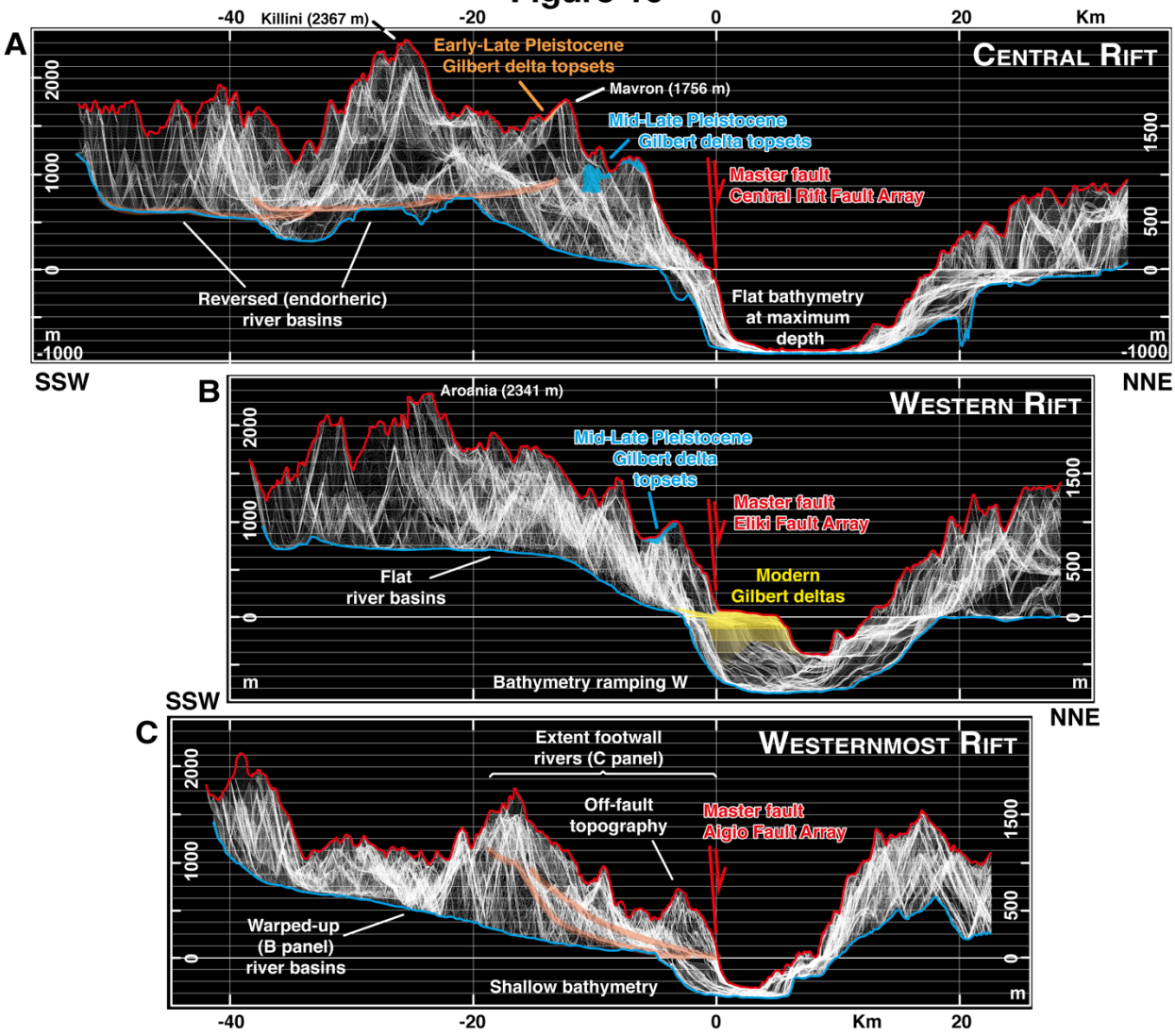

Topographic variations in the west rift are relevant in short horizontal distances, as marked by the maximum and minimum topography envelopes (Fig. 10B). The west rift contains the second highest summit (Aroania, 2341 m) and a northward decreasing topography with topsets of Mid-Late Pleistocene Gilbert deltas at ~700-1000 m heights and <5 km from the border fault. Rivers with flat upstream reaches and steep lower reaches set the minimum topography and feed large modern Gilbert-type deltas (Fig. 10B). A flat wide bathymetry at –750 m in the east changes westward to a narrower rugged bathymetry at shallower depths (approx. –375 m). This change occurs in both basin margins and not only in relation to deltas. The maximum topography envelope in the northern margin has a concave-up profile not paralleled by the minimum topography envelope (Fig. 10B).

The westernmost rift has the lowest variations in topography (Fig. 10C). Two topographic maxima bound two differentiated areas in the southern margin. In the area close to the master fault, a steep maximum relief envelope decays monotonically from the footwall river headwaters, except for a topographic high in its westernmost end ("off-fault topography" in Fig. 10C). The area farther away from the master fault has a minimum topography envelope in relation to longer rivers. The rift is here the narrowest and shallowest, with a width of ~8 km at sea level and a basin floor at depths between –250 m and –350 m (Fig. 10C). The maximum and the minimum topographic envelopes in the northern margin have a sharp triangular shape with its maximum ~15 km north of the coast.

3.6.2 Along the rift axis

Maximum drainage topography has variable along-strike average elevations of ~750 m in the east, ~2000 m in the center and ~1600 m in the west (Fig. 11A). The maximum relief within ~21 km of the rift-bounding fault (Fig. 11B) similarly varies along-strike at heights ~70-80% of those in the maximum drainage topography (Fig. 11A). Both profiles significantly increase in elevation between the east and central rift while only the maximum drainage topography decreases markedly west of Aroania summit (at ~2341 m) (Figs. 6, 7 & 11). Bathymetric depths show a sharp transition in the east, from depths of ~150 m to >800 m. Similar bathymetric depths are maintained westwards for ~40 km, and then decrease gently to <250 m in ~40 km (Fig. 11C).

Figure 11

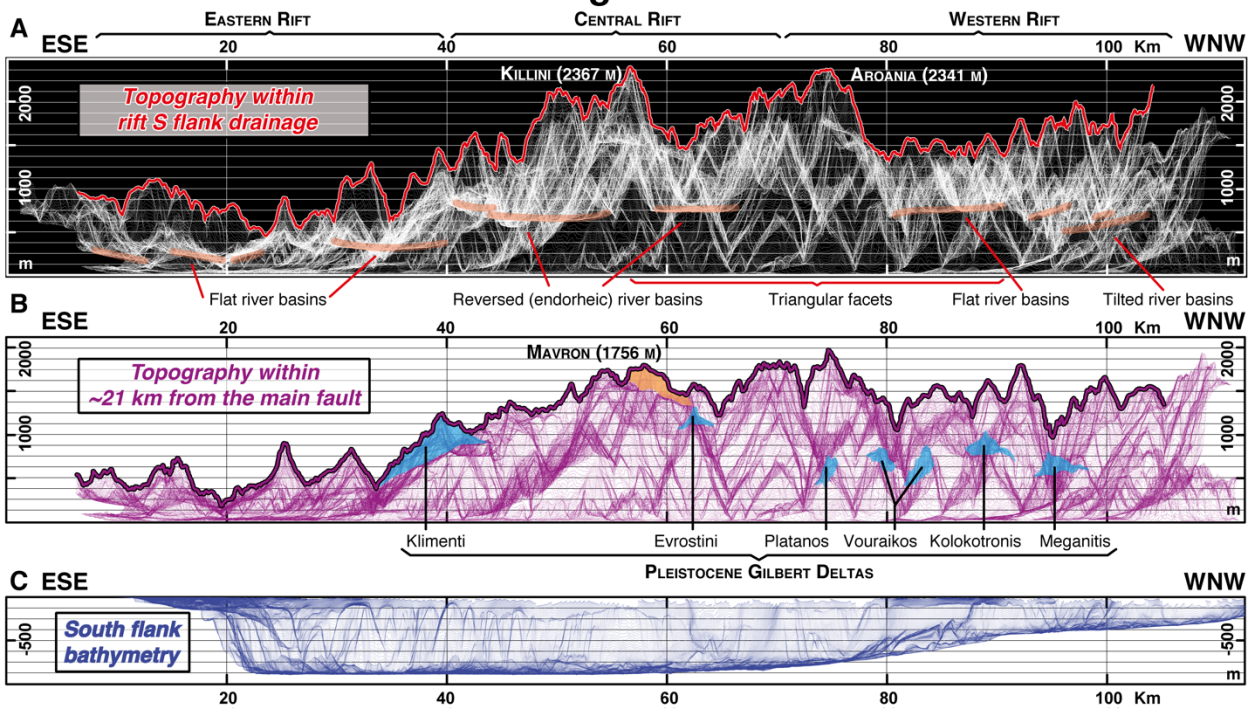

Fig. 11 (prev. page). *Stacked swath profiles of topography and bathymetry along the southern flank of the Corinth Rift in a view parallel to the master fault. The "view" is looking SSW, with a projection line N105°E, defined to represent the average strike of the master fault. Plotted profiles are exaggerated ~8 times. Relief in A and B panels is defined by 500 stacked swath profiles of estimated width ~90 m, on a 20m-resolution DEM.* ***(A)*** *Maximum relief within the rift flank drainage is obtained clipping the DEM to the extent of the river networks draining the southern coast of the Gulf of Corinth, including the endorheic river basins; and* ***(B)*** *Maximum relief within ~21 km from the fault is obtained clipping the DEM at ~21 km from the main fault and aims to approximate to the relief related to the bounding fault system. In these panels, no bathymetric data is used and there is no correction on the basis of master fault position, i.e. plotted relief is a good approximation to footwall relief only in the area where the fault is at or near sea level (from Akrata eastwards for ~7 km, Fig. 6). River basins are marked in red in panel A, and the topsets of Gilbert delta are marked in blue (Mid-Late Pleistocene) and light brown (Calabrian) in panel (B).* ***(C)*** *Bathymetry from north of the lower bathymetry axis to the south coast of the gulf, as seen by 500 stacked swaths profiles in a 50-m resolution bathymetry (see section 3.1).*

River drainages and triangular facets stand out in the stacked swaths of southern margin of the Corinth Rift (Fig. 11). River drainages (dimmed red lines; Fig. 11A) show significant differences along the main rift margin strike. Low laying drainages in the east exist at elevations below ~300 m. Flat concave-up drainages in the center lay at elevations between ~700 m and ~800 m in relation to the endorheic plains. Catchments farther west have similar morphologies decaying in elevation to ~600 m and tilting lightly to the east (Fig. 11A). Well-developed triangular facets in the center and west rift occur in four hierarchical levels and often have a perched Gilbert deltas laying at their triangular facets "tips" (Fig. 11B). The oldest Gilbert delta of the rift, Mavro (Figs. 6 & 7) outcrops at the highest fault-related relief (~1756 m) in relation to the highest set of triangular facets, with triangle tips at ~1600-1750 m (purple line; Fig. 11B). Gilbert delta topsets of younger age, Klimenti and Evrostini, outcrop to the sides of Mavro at heights coincident with the second highest tips of the triangular facets (at ~1000-1200 m). Gilbert deltas to the west (Platanos, Vouraikos, Kolokotronis and Meganitis) (Figs. 6 & 7) lay on top of triangular facets with tips at ~850-950 m (Fig. 11B). A fourth set of triangular facets, with tips at ~500 m elevation, is seen only in the center of the margin (Fig. 11B). Aforementioned first-order variations along the rift axis may result from changes in rift maturity potentially derived from decreasing slip rates and/or younger ages in border fault westwards.

3.7 Footwall river long profiles and tectonic knickpoints

We analyse the longitudinal profile geometry of the 16 largest rivers draining the southern margin of the rift, and picked tectonic knickpoints in their trunks (Fig. 12 & Table 1). We reproduce river profile geometry using Topotoolbox 2.0 (Schwanghart and Scherler, 2014), and perform knickpoint analysis with the χ-profiler package (Gallen and Wegmann, 2017). We

analyse knickpoints in river trunks to assess their tectonic origin, which we corroborate with knickpoints at similar heights in nearby tributary streams. See Suppl. material D for details on river profile analysis.

In the east rift, river longitudinal profiles are flat (<300 m elevation in upstream distances of >15 km) and show broad up-convexities (Fig. 12A, right). Here, all trunks show a knickpoint laying at low elevations (100-200 m) (Fig. 12B & Table 1), and a variable number of knickpoints with heights that lay at three elevations (two at ~275 m, two at ~450 m and one at ~700 m). In the central rift, the shortest and steepest longitudinal profiles (>1 km height in <15 km) flow towards the gulf at the front of wind-gaps bounding large endorheic plains of reversed rivers. Central rift exorheic and endorheic catchments, taken together, show the largest divergence from theoretical profiles in steady-state (Fig. 12A, center). Here, each river has either three or four tectonic knickpoints, and there are three families at different heights (Fig. 12B & Table 1). A set of knickpoints lay again at low elevations (100-200 m) for all but Trikalitikos R, which is the largest river network. Two other sets of tectonic knickpoints lay at ~1100-1200 m (Trikalitikos, Fonissa, Dervenios, Krios), and between ~1500 m and ~1700 m for the two river networks that reach that elevation (Trikalitikos, Krios) (Fig. 12B, Table 1). In between these knickpoints, their height is more distributed, but another set can be seen gaining elevation from east (500 m at Trikaitikos R) to west (700 m at Krios R) (Fig. 12B). Fonissa R has another tectonic knickpoint at ~375 m and Skoupeiko R at ~825 m.

In the west rift, rivers alternate long (≥35 km) and short (<15 km) longitudinal profiles except for the westernmost footwall river catchments. Short rivers catchments compare with the steep profiles of the central rift. Long rivers have morphologies with up-convexities departing from an inferred steady state profile geometry (Fig. 12A, left) and declining in steepness westwards (see Fernández-Blanco et al., 2019a for details). In the west rift, we differentiate two areas. Rivers transecting the Eliki FA have four tectonic knickpoints, except Ladopotamos R, with three (Fig. 12B, Table 1). With the exception of the latter, one set of knickpoints lies again at elevations between 100 m and 200 m. Tectonic knickpoints of the other three families lay at lower elevations for the longer trunks (Krathis, Vouraikos, Selenous) and at higher elevations for the shorter trunks (Ladopotamos, Kerinitis). Footwall rivers associated with the Aigio FA (Meganitis, Finikas) present two knickpoints each and none correspond to the low elevation knickpoints observed elsewhere in the southern rift flank (Fig 12B, Table 1). Contrarily, the uppermost set of tectonic knickpoints in both rivers is at a similar position than the set of tectonic knickpoints at highest elevations in all trunks eastwards.

Figure 12

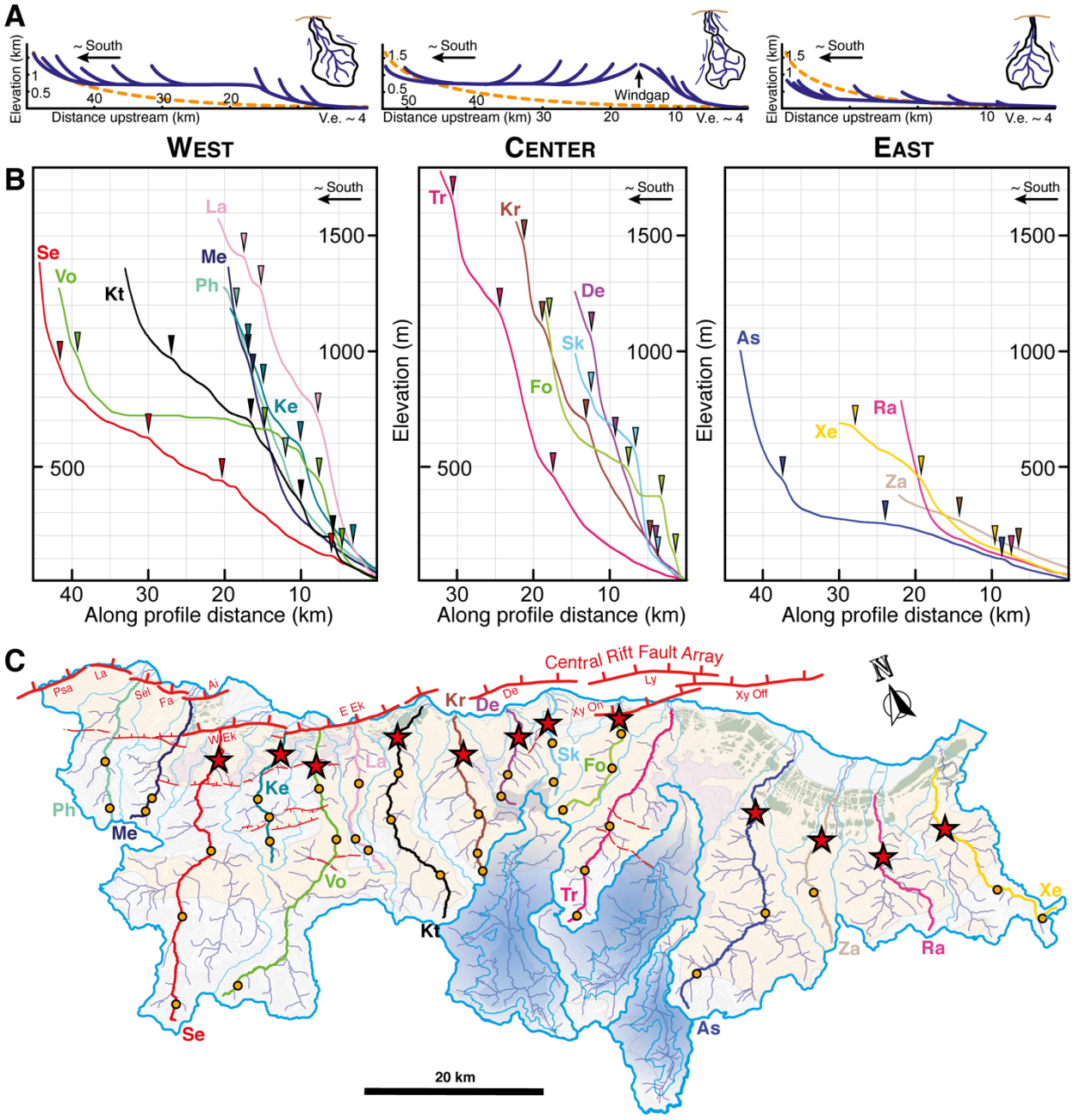

Fig. 12. *Sixteen largest river catchments in the southern margin of the Corinth Rift and tectonic knickpoints of their trunks.* ***(A)*** *Illustrative representations of main characteristics of river longitudinal profiles and plainviews per rift sector defined by this contribution; west (left), center (center) and east (right) rift, exaggerated 4 times in the vertical.* ***(B)*** *Main tectonic knickpoints of the trunks of the sixteen largest river catchments of the southern margin of the Corinth Rift in longitudinal profile view, grouped per rift sector. East: (Xe) Xerias, (Ra) Raizanis, (Za) Zapantis and (As) Asopos; Center: (Tr) Trikalitikos, (Fo) Fonissa, (Sk) Skoupeiko, (De) Dervenios and (Kr) Krios; West: (Kt) Krathis, (La) Ladopotamos, (Vo) Vouraikos, (Ke) Kerinitis, (Se) Selinous, (Me) Meganitis and (Fi) Finikas.* ***(C)*** *Location of tectonic knickpoints in map view. For this analysis we also used slope-area and χ plots . The stars mark the lower set of tectonic knickpoints seen in most river trunks at low elevations.*

4 Theoretical background: Footwall record of normal fault growth

Normal faults growing self-similarly by tip propagation have distinct individual displacement profiles with displacement maximum at the centre of the fault total length and displacement minima at its ends (e.g., Dawers et al., 1993; Manighetti et al., 2005; Childs et al., 2017). Elliptical to triangular fault displacement profiles are common, although mechanical restrictions like adjacent faults and/or original location of the fault nucleation point result in other shapes (e.g., Manighetti et al., 2001, 2005). The displacement profile of single normal faults is similarly modified during fault growth as local stress fields deviate at its tips by mechanical interactions with adjacent faults (e.g., Willemse, 1997; Gupta and Scholz, 2000). This intrinsic characteristics of normal fault displacement profiles help evaluate whether fault segments adjacent at the surface are connected at depth.

Whereas unconnected faults initiating mechanical interaction may have a displacement profile with more than one maxima and reduced aspect ratios, fault segments mechanically linked at depth show a single displacement profile for their summed fault lengths and normal aspect ratios (e.g., Anders and Schlische, 1994; Dawers and Anders, 1995; Gupta and Scholz, 2000; Manighetti et al., 2001, 2005). Faults that grew independently and later linked may show a large-wavelength composite displacement profile composed of fault displacement profiles with shorter wavelengths (e.g., Cowie and Roberts, 2001; Whittaker and Walker, 2015). Between initial mechanical interaction and full linkage of individual fault strands, increased aspect ratios and transient “under-recovered” displacement profiles briefly occur as lateral tip propagation and fault lengthening is limited while faster-than-normal displacement takes place at the linkage zone in order to reach a new “recovered” single-fault profile (e.g., Cartwright et al., 1995).

4.1 Footwall elements used as proxies for normal fault growth

Range front relief is the result of cumulative fault displacement and can be used to assess the dimensions and the history of growth and linkage of range-bounding normal faults (e.g., Dawers and Anders, 1995; Gupta and Scholz, 2000). If erosion is effective and fault tip propagation and slip rate are coupled, the range front relief maxima occurs at a uniform distance from their border faults (Densmore et al., 2005, 2007). We use an equivalent to range

front relief, footwall relief (Fig. 13B), defined as the height of the first major slope break in the extensional footwall, measured vertically from the trace of their active normal faults (e.g., Whittaker and Walker, 2015), and can be used as a proxy to upper-limit fault displacement profile (Fig. 13). Suppl. material E provides details about our procedure to calculate footwall relief.

While migrating upstream as a kinematic wave (Rosenbloom and Anderson, 1994), the knickpoint bounds steeper downstream river reaches adjusted or adjusting to the new uplift conditions from flatter upstream river reaches unaware of the uplift rate change (Fig. 13A) (e.g., Whipple and Tucker, 1999; Snyder et al., 2000). Whereas knickpoint retreat rates (map view) are fundamentally controlled by drainage area and bedrock erodibility (e.g., Wobus et al., 2006; Berlin and Anderson, 2007), knickpoint vertical propagation rates (profile view) are directly proportional to tectonic change amplitude (e.g., Whittaker et al., 2008). Hence, tectonic knickpoints migrate upwards predictably and have heights, measured from the active fault, that scale with the fault vertical displacement and footwall relief (e.g., Kent et al., 2016). A given set of tectonic knickpoints found in river drainages of extensional footwalls may be related to three fault-related events: fault initiation, fault linkage or fault slip rate increase (Whittaker and Walker, 2015; Gallen and Wegmann, 2017).

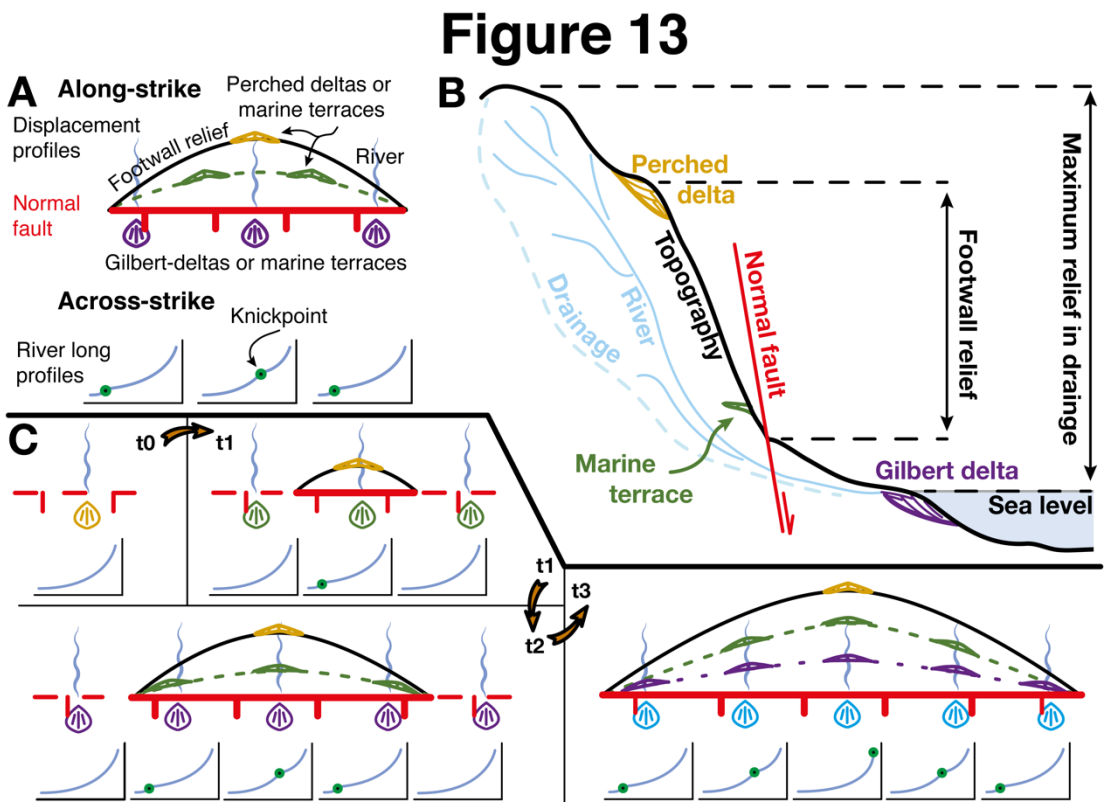

Fig. 13 (prev. page). (A) *Schematic representation of elements in extensional footwalls in relation with their active faults in an along-strike view and footwall rivers and their tectonic knickpoints in across-strike view.* ***(B)*** *Elements of an extensional footwall and their relation with the proxies of relief used in this study.* ***(C)*** *Self-similar growth of a normal fault, as shown by geomorphic features in its footwall, in four time-steps: (t0) steady-state of a river network - Gilbert delta system; (t1) initiation of normal fault activity and footwall flexural uplift propels formation of a tectonic knickpoint and uplifts former Gilbert deltas; (t2) lateral growth of the normal fault leads to inclusion of rivers in its footwall, and the formation of new tectonic knickpoints and uplift of new Gilbert-deltas; (t3) lateral self-growth and perpetuation of t2. Similar constraints by Gilbert-deltas on fault displacement profile (albeit more accurate) can be inferred using marine terraces. Other inferences on fault displacement profiles can be obtained from footwall relief and total topography. Assuming that geomorphic features formed at each time-step are not eroded and can be dated, their location and height provide key constraints on the fault growth and displacement profile in time.*

Fluvial geomorphology accounting for normal fault laws allow the evaluation of fault growth, linkage, and inferences of tectonic and fault throw rates (e.g., Boulton and Whittaker, 2009; Whittaker and Boulton, 2012; Whittaker and Walker, 2015; Kent et al., 2016; Gallen and Wegmann, 2017). For example, in detachment-limited rivers, a new local convexity or knickpoint forms in a footwall river after an increased uplift rate led by a fault slip increase.

Correlatable marine terraces and/or Gilbert-type deltas can be used as strain markers and allow reconstructions of coastal landscapes (Fig. 13C). Marine terrace shoreline angles, at

the intersection between the terrace and its inland-bounding cliff, best characterize sea level position during terrace formation, typically in sea level highstands (Lajoie, 1986; Anderson et al., 1999; Scott and Pinter, 2003). Similarly, Gilbert-type delta topset-foreset contacts set approximately at sea level (Gilbert, 1890) as proximal topsets extend the alluvial plain subaerially, and distal foresets prograde basinwards underwater. Sets of coeval morphotectonic markers, i.e. marine terraces of the same sea-level highstand or Gilbert deltas deposited at similar age, may form sequentially along uplifting coasts and lead to uplifted sets that down-step coastwards into younger sets (Figs. 13B, C). Land relative upwards motion between the formation of two sets of morphotectonic markers can be retrieved from the height difference between them, taking into account past sea-level positions. If coastal uplift occurs in extensional footwalls, the land upwards motion relative to the sea level is a proxy for fault displacement, and sets of coeval morphotectonic markers can be approximated to fault displacement profiles in time (Fig. 13C). Relative along-strike fault uplift rates can be derived using the age of the coeval morphotectonic sets.

4.2 Approach to reconstruct normal fault growth in time

We propose a conceptual framework to reconstruct growth and propagation history of active normal faults (Fig. 14). The framework uses the first-order morphological expression of topography, relief, river catchments and morphotectonic markers in extensional footwalls (Figs. 13 & 14), and is predicated on the response to fault linkage expected in fault displacement profiles and tectonic knickpoints of extensional footwall river profiles (e.g., Anders and Schlische, 1994; Dawers and Anders, 1995; Gupta and Scholz, 2000; Cowie and Roberts, 2001; Manighetti et al., 2001, 2005; Attal et al., 2008; Whittaker et al., 2008; Whittaker and Boulton, 2012; Whittaker and Walker, 2015; Gallen and Wegmann, 2017). This framework builds on these studies to discriminate, barring complicating factors, the relative time of activity of individual fault segments and linkage mode; simple, directed or propagated (Fig. 14). Co-linear normal faults that initiated activity concurrently and later interacted by simple (non-directed) linkage (Fig. 14C) present symmetrical fault displacement profiles throughout their evolutionary history, both as individual and composite faults. These normal faults show two sets of genetically-linked tectonic knickpoints. The oldest set of tectonic knickpoints forms at the moment of initiation of each fault and lays at higher elevations, roughly similar in all river networks. The youngest set of knickpoints develops when faults link and lays at lower

elevations, with knickpoint heights relatively higher for footwall river profiles in the area of fault linkage (Fig. 14C).

Although co-linear normal faults initiating activity at different times may develop similarly asymmetric end displacement profiles, we envisage characteristic tectonic knickpoint arrays depending on whether faults are initially unconnected and link successively or new fault segments become active by propagation. In the successive initiation case (Fig. 14D left), fault displacement profiles are symmetrical until the moment of linkage, and have a composite asymmetrical displacement profile from linkage until displacement profile "recovery" to single fault shape. The displacement maxima of the older fault sets at a higher position than the displacement maxima in the younger fault. Three families of knickpoints occur (Fig. 14D left); (i) an oldest set at the relative highest elevations exists solely in the oldest fault footwall; (ii) a second set appears at mid elevations solely in the youngest fault footwall; (iii) one last set of knickpoints occurs at the relative lowest elevations along the strike of the composite fault, with knickpoints that lay higher at its linkage zone and are absent at its tips.

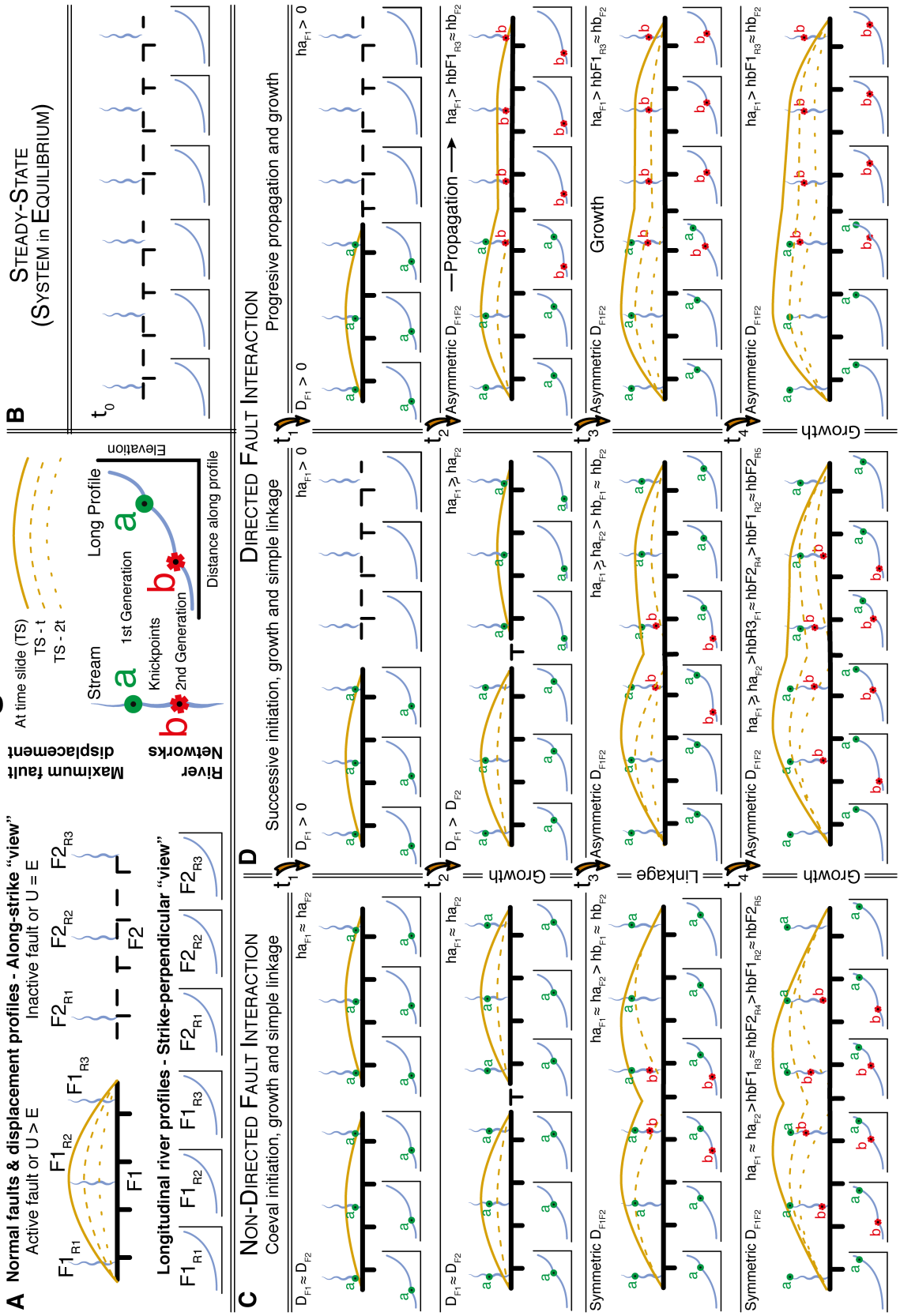
Figure 14
A Normal faults & displacement profiles - Along-strike "view"
Active fault or U > E
Inactive fault or U = E
Longitudinal river profiles - Strike-perpendicular "view"
Maximum fault displacement
River Networks
At time slide (TS)
TS - t
TS - 2t
Stream
1st Generation
Knickpoints
2nd Generation
Long Profile
Elevation
Distance along profile
B Steady-State (System in Equilibrium)
C Non-Directed Fault Interaction
Coeval initiation, growth and simple linkage
D Directed Fault Interaction
Successive initiation, growth and simple linkage
Progresive propagation and growth
Growth
Linkage
Propagation
Asymmetric
Symmetric

Fig. 14 (prev. page). *Diagrams for fault displacement and tectonic knickpoint height of footwall rivers associated with different modes of initiation, growth and linkage or propagation between adjacent normal faults.* ***(A)*** *Main features of the diagrams in the rest of the figure. Top-left: normal faults in an along-strike view, their displacement profiles in time, as expressed in top-right, and a simple representation of six footwall rivers, whose longitudinal river profiles are represented in the lower-left. Lower-right: legend for the main components of the longitudinal river profiles.* ***(B)*** *Initial state, t = 0, for all cases, representing steady-state equilibrium.* ***(C)*** *Non-directed fault interactions, showing coeval growth and link.* ***(D)*** *Directed fault interactions, with normal faults that initiate with a preferential direction (rightwards), either by growth and linkage (left column) or by propagation (right column). In all cases, only the second generation of knickpoints developed in the linkage zones are near the tips of the faults (and shows a convex outward knickpoint propagation mode). In all cases, F is for fault, D for fault displacement profile, R is for river, a and b are tectonic knickpoint sets, and h is elevation; thus,* D_{F1F2} *is a composite displacement profile including both faults, and* $ha_{F1} > hbF1_{F2} \cong hb_{F2}$ *means that the set a of tectonic knickpoints in fault 1 is at higher elevations than the set b of tectonic knickpoints in the third river of fault 1, which is at similar elevations than set b in fault 2.*

In the propagation case (Fig. 14D right), the displacement profile is always asymmetrical, except in the oldest fault segment at times before propagation. As long as new propagation takes place at a faster pace than displacement profile "recovery" to single composite fault form, the displacement profile remains elongated and relatively flat, with its lowest displacement maxima in the sense of propagation (Fig. 14D right). Knickpoint families are expected to occur at the moment of initiation of each fault segment, occupying relatively lower positions in the sense of propagation and effectively marking the extent of propagation at any given time.

5 Analysis of fault growth and relief response

We plot tectonic knickpoints of footwall catchment trunks (section 3.7) together with footwall relief (see section 4.1 & Suppl. material E) to explore their mutual relation and that with the border fault (section 4.2) (Figs. 15 & 16). We project the height of tectonic knickpoints of river trunks, measured vertically from border faults they cross, orthogonally to faults' strike at the point of intersection. Tectonic knickpoints belong to the 16 largest river trunks draining the gulf and to the trunks of the two largest reversed drainages (Olvios and Safenetos; Table 1). We tentatively correlate tectonic knickpoints across fault strike on the basis of cross-causality, not cross-coevality, i.e. equal numbers do not imply equal occurrence times but equal (interpreted) mode of tectonic perturbation in the border fault (initiation, linkage, slip rate increase). This correlation aims at reconstructing the main tectonic perturbations of the border fault since its formation and accounts for the considerations detailed below.

Reverse drainages in the central rift were footwall rivers that drained north and eventually disconnected from their original outlet, probably <1 Ma. Tectonic knickpoints in (now) endorheic river basins record tectonic perturbations in the border fault until the moment of inversion, and are thus relevant to understand the growth and evolution of border faults. In fact, these tectonic knickpoints have a longer "recording period" than other drainages. The two knickpoints in both reversed basins are at similar elevations of ~1200 m and ~1400 m, and the windgaps related to the disconnection of these basins are carved in topsets of Gilbert-type deltas of different ages perched at different elevations. The highest windgap is at ~1300 m in the Late Pliocene-Early Pleistocene Mavro Delta, and the lowest windgap is at ~850 m, carved in rocks of the Klimenti Delta, with an approximate age of Middle-Upper Pleistocene (e.g., Ford et al., 2016).

5.1 Border fault growth in the west rift

The Eliki FA footwall relief shows a broad (~7 km) maximum at ~1900 m in the east, and decays towards the west to a minimum value of ~600 m (Fig. 15). Between both ends, the footwall relief has three local maxima (at ~1900m, ~1500 m and ~1000 m) and four local minima that correlate with the extent of different faults (Figs. 6, 7 & 15), i.e. local maxima roughly coincide with the center of East Eliki (undifferentiated from the East Offshore Eliki), West Eliki and Westernmost Eliki faults, respectively, and local minima set between each fault segment (Fig. 15). Footwall relief westward decline is constant, with local minima sited below each local maximum, –400 m below eastwards and –800 m below westwards (Fig. 15). Minima at the tips of Westmost Eliki F are exceptional and both lay at similar elevations (~600 m below their local maximum).

The overall trend of Aigio FA footwall relief has a minimum at ~900 m in the east, and a maximum at ~1900 m in the west. The extent of the four single fault strands coincide with footwall relief individual "up-pointing triangles" (minima at tips and a maximum at center) (Figs. 6, 7 & 15). The overall trend is defined by local minima that lay roughly every ~7 km at heights of ~900 m (east of Aigio F), ~1100 m (between Aigio and Fasouleika faults), ~1200 m (between Fasouleika and Selianitika faults) and ~1300 m (between Selianitika and Lambrini faults). The trend set by local maxima is more complex, with the east Aigio F showing a maximum of ~1800 m, only ~100 m lower than the displacement maxima at the center of Lambrini F, in the west (Fig. 15). In between, footwall relief rises west more gently than the overall trend in mean

topography (~200 m height difference in ~10 km along strike in an overall trend of ~700 m in ~20 km) (Fig. 15).

The footwall relief patterns of both Eliki FA and Aigio FA can be attributed to individual growth of fault segments and subsequent link into a larger fault systems (see details in section 4.1). The east rising trend in footwall relief in the Eliki FA suggest that it behaves as the western termination of a larger fault and the footwall relief plateau in the overlap between Eliki and Aigio fault arrays points to recent linkage between both fault systems (section 4).

Figure 15

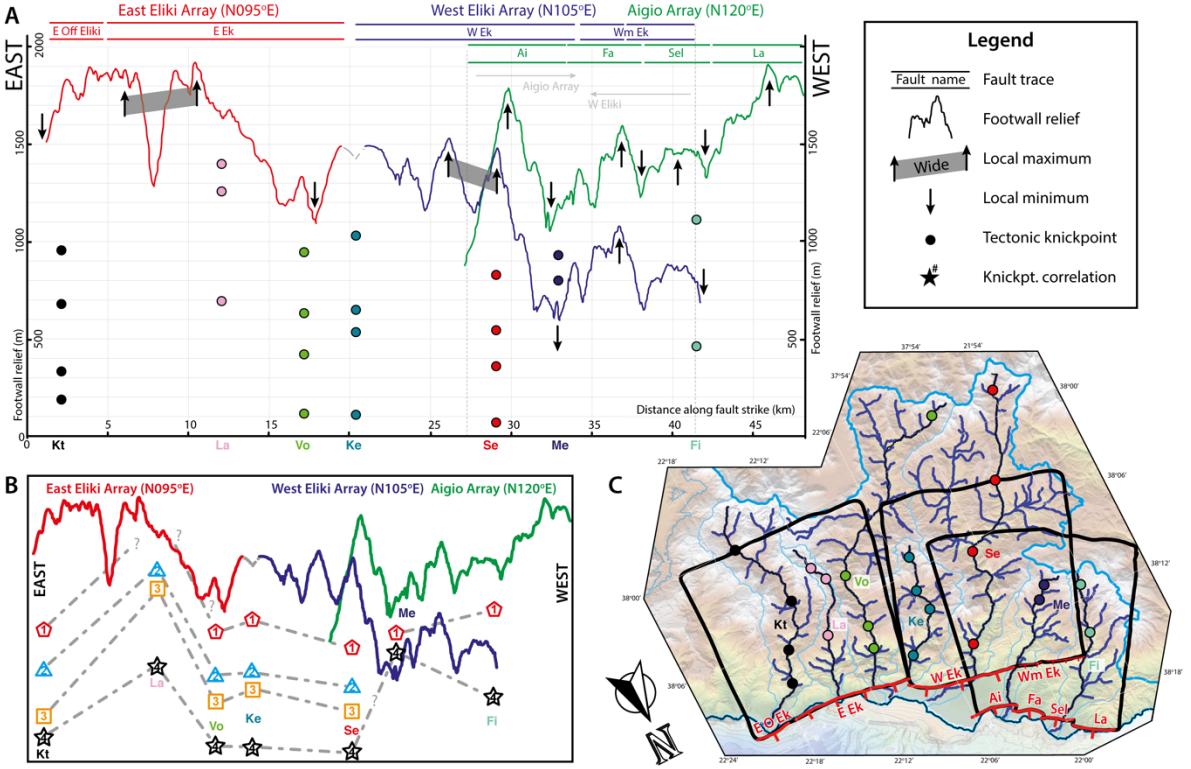

Fig. 15. (A) *Footwall relief associated with the Eliki FA and Aigio FA, and the heights of the tectonic knickpoints of river trunks intersecting them. The strike of each fault array was simplified for their whole length as N275·E for East Eliki F, N285·E for West Eliki F and N300·E for Aigio FA. Both footwall relief and knickpoint heights are measured vertically in relation to their active faults. Footwall relief is shown in different colours for each correlatable fault array. Tectonic knickpoint heights of Krathis (Kt), Ladopotamos (La), Vouraikos (Vo), Kerinitis (Ke), Selinous (Se), Meganitis (Me) and Finikas (Ph) rivers are projected perpendicularly to the strike of Eliki FA and Aigio FA at the point where the river crosses the fault. To avoid duplicity in the overlapping area between West Eliki Array and Aigio FA, tectonic knickpoints are plotted only as "seen" by the Aigio FA.* ***(B)*** *Tectonic knickpoints lateral correlation as per analogous tectonic perturbation in the main fault.* ***(C)*** *Map view, shown with north pointing down. Thick black boxes in the footwall of each fault segment mark the extent of the DEM areas used for the projection of the footwall relief. Tectonic knickpoints, with coloring is in agreement with panel (A), belong to the trunks (in black) of the river networks (in blue) that run through the active faults (in red).*

We recognised four groups of tectonic knickpoints in the west rift that show marked differences between Eliki FA and Aigio FA (groups 1 to 4 in Fig. 15B). In the Eliki FA, the three sets of tectonic knickpoints at highest positions (groups 1, 2 & 3 in Fig. 15) correlate with footwall relief, laying at higher and lower elevations in footwall relief maxima and minima, respectively. This leads to triangular patterns (grey dashed lines in Fig. 15B) in these three sets that roughly mimic footwall relief trends. Such a trend is less clear for tectonic knickpoints at lower and western positions, and potentially absent for the lower set (group 4 in Fig. 15B). Instead, this lower knickpoint set shows an apparent trend towards lower elevations at westward positions (Fig. 15 & Table 1). The highest tectonic knickpoints in river trunks transecting the Aigio FA (group 1 of Meganitis and Finikas in Fig. 15B) are close to the drainage divide, in a position comparatively similar to the highest set of tectonic knickpoints eastward (Table 1). The relative high elevation of the tectonic knickpoint set at low elevations in Meganitis and Finikas trunks may indicate that they developed in relation to recent fault linkage (see theoretical framework in section 4.2 and Fig. 14), and we have tentatively correlated them with the set at ~100-200 m farther east (group 4 in Fig. 15B).

Our interpretation implies that both footwall relief and tectonic knickpoints are genetically linked, with perhaps the exception of the westernmost two river catchments (Fig. 14). Group 1 lays at highest positions and closest to the drainage divide in all drainages. We interpret that it correlates with the initiation of tectonic activity at each individual fault segment. We consider that this group is absent in the Ladopotamos River due to river capture immediately above its drainage divide by the Vouraiko River stream that flows parallel to the coast (Fig. 15C). We interpret Group 2 as the result of hard linkage of individual fault segments into the Eliki FA, with no connection farther west. We suggest that Group 3 formed by linkage of the Eliki FA with fault segments in the central rift, i.e. by the effective connection of the main fault at larger scale (see section 5.2 below). We consider that the lowest set of tectonic knickpoints that exist in all rivers (Group 4) formed at the moment of westward inclusion of the Aigio FA (section 4.1; Figs. 7 & 14).

We defend that this sequence is the most plausible geologically. Correlatable sets of tectonic knickpoints will develop in composite faults from their linkage onwards (“b” sets in bottom two rows of Fig. 14), except at its tips or if the tectonic perturbation has not yet reached those rivers. Therefore, tectonic knickpoint sets on different faults can only be correlatable if linkage is already effective. For the west rift, the simplest scenario assumes that tectonic knickpoints laying at lower elevations in the west rivers (Group 4 in Meganitis &

Finikas, Figs. 15A,-B) formed coevally and hence both correlate with just one set of tectonic knickpoints farther east. If tectonic knickpoints laying at lower elevations in the west rivers would have formed coevally with older groups, other knickpoint sets developed at younger times should exist at lower elevations. Contrarily, our proposed tectonic disturbances for groups 2 and 3 respect the absence of tectonic knickpoints in the Aigio FA footwall rivers, laying farther west than our inferred fault tip at that time. Since linkage should be either the last or the second to last tectonic perturbation event in the sequence, on the basis of Fig. 15 only, the last two events could have taken place coevally or in a different order.

5.2 Border fault growth in the rift margin

Footwall relief has a wavelength that correlates with the rift southern margin, with a maximum in vertical displacement around its center and minima at both ends (Fig. 16; see section 4). Several sets of up-pointing triangles contained in successively larger triangles exhibit similar footwall relief morphologies at smaller scales, within the rift-scale parabolic trend. Most first-order triangular morphologies can be tracked with confidence to their respective faults, with maximum around the centre of each fault segment and two minima at its tips (cf. Fig. 16A & 16B). For example, the ~12 km-wavelength individual up-pointing triangle that sets the maximum footwall relief is formed by three individual triangles, and correlates in lateral extent with the Derveni F, and (partially with) the West Onshore Xylokastro F traces (Fig. 16A,-B). This is indicative that either of these faults or both together have the largest slip and are the oldest fault segment(s) of the composite master fault, and suggest onset of activity in relation to three individual fault segments before linking into the Derveni F and/or the West Onshore Xylokastro F. Overall, the parabolic geometry of the footwall relief indicates that the border faults behave as a single fault at depth, and the different hierarchies of up-pointing triangles suggest that the fault grew by along strike fault linkage (section 4).

Most trunks show four tectonic knickpoints that ought to result from tectonic perturbations that occurred during the growth of the border faults of the Corinth Rift southern margin (see section 4.1). At least one of those perturbations affected the entire fault system, perhaps with the exception of the Aigio FA in the westernmost rift.

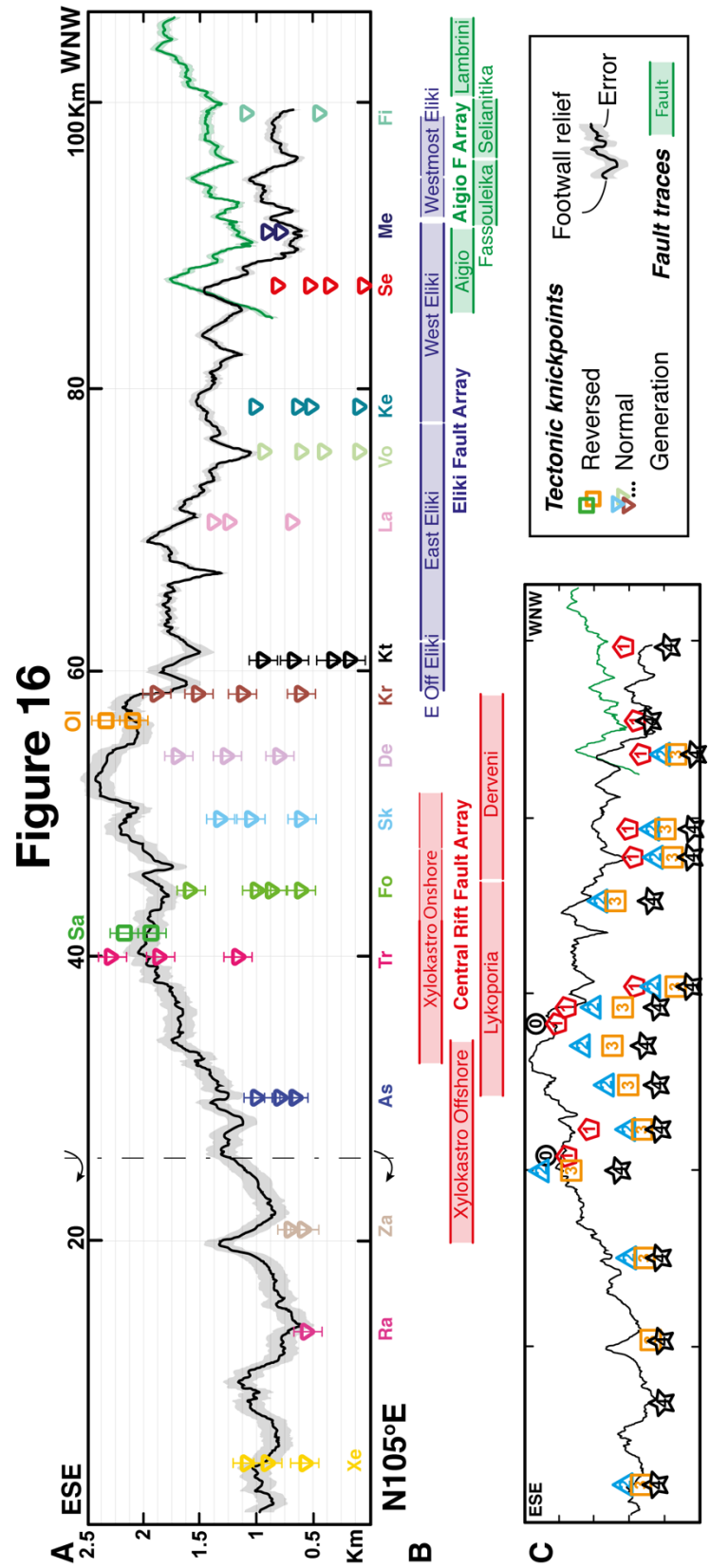
Figure 16
A
ESE
WNW
100 Km
80
60
40
20
Km
2.5
2
1.5
1
0.5
Sa
Ol
Xe
Ra
Za
As
Tr
Fo
Sk
De
Kr
Kt
La
Vo
Ke
Se
Me
Fi
B
N105°E
E Off Eliki
East Eliki
West Eliki
Westmost Eliki
Eliki Fault Array
Aigio
Aigio F Array
Lambrini
Fassouleika
Selianitika
Xylokastro Onshore
Xylokastro Offshore
Central Rift Fault Array
Lykoporia
Derveni
C
ESE
WNW
Tectonic knickpoints
Reversed
Normal
Generation
Footwall relief
Error
Fault traces
Fault

Fig. 16 (prev. page). *Projection along master fault strike (N105·E) of footwall relief, and tectonic knickpoints of footwall river trunks with regards to the location of main fault segments.* ***(A)*** *Footwall relief of the master fault, and heights of main tectonic knickpoints of footwall river trunks, measured from the main fault. Tectonic knickpoints of footwall rivers draining the gulf are plotted as triangles (see Table 1). Squares represent tectonic knickpoints seen for the trunks of the reversed rivers of (Sa) Safenetos (green) and (Ol) Olvios (orange). River networks are, from east to west: (Xe) Xerias, (Ra) Raizanis, (Za) Zapantis, (As) Asopos, (Tr) Trikalitikos, (Fo) Fonissa, (Sk) Skoupeiko, (De) Dervenios, (Kr) Krios, (Kt) Krathis, (La) Ladopotamos, (Vo) Vouraikos, (Ke) Kerinitis, (Se) Selinous, (Me) Meganitis and (Ph) Finikas. Tectonic knickpoints are projected perpendicularly to the master fault overall strike (N105·E) in two different manners. If the master fault is onshore, i.e. mapped with confidence, the intersection between river trunk and master fault sets the horizontal position of the projected knickpoint, while its height is measured vertically from the fault trace (as in Fig. 15). If the master fault is offshore and its trace is more uncertain, we derive horizontal position of the projected knickpoint as the average point of the projected lateral extent of its footwall catchment. Its vertical position is the tectonic knickpoint height measured vertically from the master fault trace, but we attached an estimative error equivalent to that used for the footwall relief. Further west than the vertical dashed line, elevations for both footwall relief and tectonic knickpoints are taken with respect to sea level, and raised to remain coherent with the easternmost end of the footwall relief in the central sector, and using the same errors. Errors are shown as an envelope for the footwall relief, and as bars for the heights of the knickpoints. Tectonic knickpoints in the reversed catchments are shown with the same error than rivers in the central area. Error bars for the eastern rivers (left of the dashed line) are maintained equal to those in the central sector. Error bars for the western rivers are smaller than the symbols.* ***(B)*** *Approximate location and extent of the main fault segments in the direction of projection.* ***(C)*** *Interpretation of the sequence of events associated with the tectonic knickpoints.*

In the center of the rift, footwall rivers below the highest footwall relief (Trikalitikos to Krios rivers, Fig. 16A) have their tectonic knickpoints at the highest elevations and either 3 or 4 sets of tectonic knickpoints. Here, four out of the five knickpoints with the highest elevations in the entire southern rift flank are in the endorheic river basins of Olvios and Safenetos (Table 1). Westwards, as mentioned above, all footwall rivers have 4 tectonic knickpoints (Krathis to Selinous) laying at lower elevations, with the exception of Ladopotamos River (Fig. 16A), whereas only two tectonic knickpoints exist in the two westernmost footwall rivers (Meganitis and Finikas; Fig. 16). Analysis in the east was not performed, as it is prone to comparatively large errors in relation with the increasing distance between river outlets and fault trace. Overall, tectonic knickpoint heights measured vertically from the bounding fault system show triangular patterns that correlate with footwall relief at full rift-margin scale, with the exception of the lowest set in the westernmost two drainages (Figs. 15, 16 & Table 1). This implies that tectonic knickpoints and the active fault are genetically related (Whittaker and Walker, 2015), and points to faults initiation as individual segments, and their subsequent linkage and growth at rift scale (section 4.1, Fig. 14).

Table 1

River	#	KP #	X coord	Y coord	Abs. Elevat. (m)	Smooth Abs. Elvt. (m)	Elevat. from fault (m)	Drainage area (km^2)	Distance fault (m)	Distance divide (m)	Chi
Xerias	1	1	666526	4191780	138	140	Underwater	110.2144	8543	23678	1.924745
Xerias	1	2	669726	4183420	460	460	Underwater	26.7408	19860	12361	6.268060
Xerias	1	3	673346	4178620	664	665	Underwater	2.7896	28123	4098	11.672004
Raizanis	2	1	658866	4191600	113	114	Underwater	115.8364	7680	16283	1.728496
Zapantis	3	1	653046	4195520	143	144	Underwater	54.6592	12156	17621	3.718770
Zapantis	3	2	650286	4190380	267	265	Underwater	19.214	14495	9658	5.167287
Assopos	4	1	647446	4200840	124	122	Underwater	246.9484	9839	35027	1.616133
Assopos	4	2	644386	4190120	266	265	Underwater	162.4516	24165	20701	4.221977
Assopos	4	3	634766	4186440	464	454	Underwater	15.4148	37689	7177	8.628353
Trikalitikos	5	1	631426	4205420	480	478	Underwater	66.6064	17937	16608	4.265542
Trikalitikos	5	2	627066	4201740	1180	1175	Underwater	25.022	24769	9776	6.856264
Trikalitikos	5	3	624446	4197280	1644	1641	Underwater	4.428	30843	3703	10.932628
Fonissa	6	1	636386	4216360	122	113	Underwater	50.3056	1700	19260	0.573023
Fonissa	6	2	636286	4214680	381	368	Underwater	46.5236	3554	17406	1.217854
Fonissa	6	3	633966	4211420	515	514	Underwater	26.3052	8510	12450	3.253888
Fonissa	6	4	627146	4208960	1101	1084	Underwater	1.7648	18240	2720	10.176852
Skoupeiko	7	1	628725	4218520	121	121	Underwater	34.6452	5956	12975	2.221048
Skoupeiko	7	2	628666	4216420	575	576	Underwater	25.2004	7047	10264	2.857482
Skoupeiko	7	3	627266	4212280	832	810	Underwater	8.0304	12808	4503	6.169165
Devrenios	8	1	625506	4218500	162	148	Underwater	35.224	4250	12744	1.637598
Devrenios	8	2	622726	4214860	623	613	Underwater	7.5708	9593	7401	4.289638
Devrenios	8	3	621186	4212840	1066	1054	Underwater	4.0536	12694	4299	7.122171
Krios	9	1	618606	4218760	195	185	Underwater	93.7536	5021	19608	1.220103
Krios	9	2	618086	4211840	714	707	Underwater	47.8124	13471	11158	3.759270
Krios	9	3	616446	4207780	1120	1116	Underwater	7.2472	19170	5459	6.981231
Krios	9	4	616286	4205700	1473	1463	Underwater	1.4496	21600	3029	10.100120
Kratis	10	1	612526	4222760	199	174	184	133.5284	5525	28997	1.194022
Kratis	10	2	611286	4219320	351	345	336	120.7608	9875	24648	2.180448
Kratis	10	3	608666	4214720	695	694	680	84.5236	16452	18071	3.842688
Kratis	10	4	611666	4206960	970	970	955	24.9636	26851	7672	7.331195
Ladopotamos	11	1	606706	4219800	708	706	693	19.0396	7607	15012	3.244866
Ladopotamos	11	2	604166	4214100	1274	1264	1259	8.4976	15110	7509	8.007839
Ladopotamos	11	3	605066	4212400	1411	1405	1396	5.676	17350	5269	9.856060
Vouraikos	12	1	602826	4223300	138	149	108	213.2052	4499	38531	0.773081
Vouraikos	12	2	602306	4220820	447	442	417	206.7072	7480	35550	1.307397
Vouraikos	12	3	602126	4214800	661	661	631	181.276	14559	28471	2.629612
Vouraikos	12	4	585986	4203300	975	968	945	7.2736	39183	3847	11.039972
Kerinitis	13	1	599366	4225820	161	158	111	69.9096	2785	17674	0.788818
Kerinitis	13	2	595446	4222140	581	585	531	46.256	9971	10835	3.080262
Kerinitis	13	3	595786	4219680	693	695	643	14.564	12564	7895	4.278960
Kerinitis	13	4	594986	4217560	914	911	864	8.9888	15241	5217	6.099830
Selinous	14	1	592866	4227640	146	145	66	295.148	5892	40143	0.884287
Selinous	14	2	588486	4218540	439	438	359	242.3104	19731	26304	3.107405
Selinous	14	3	582866	4212760	622	621	542	51.9428	29859	16176	5.767960
Selinous	14	4	578746	4203780	908	907	828	10.0236	41463	4572	10.910468
Meganitis	15	1	584247	4226074	853	848	803	8.1643	18527	5662	7.073409
Meganitis	15	2	583166	4225300	970	955	930	6.116	16733	4516	7.361968
Phoenix	16	1	580866	4232120	511	508	461	31.8224	11964	10382	3.927337
Phoenix	16	2	579506	4227040	1162	1153	1112	5.0552	18342	4005	8.081930

Table 1. *Data associated with the tectonic kickpoints identified in the trunks of the 16 river networks analysed in this study.*

We recognized five groups of tectonic knickpoints in the central rift (groups 0 to 4, Fig. 16C). Group 0 implies an extra tectonic perturbation not seen elsewhere in the rift shoulder, which we suggest relate to the formation of individual fault segments in the rift center. Knickpoints of the lowest set within the endorheic drainages (Group 1) lay at heights that coincide with the footwall topography (Fig. 16A,-C). Group 1 is ~100 m below the windgap in Mavro area, where footwall relief is maximum, and ~350 m above the windgap in the Klimenti area, where footwall relief is at lower heights. Therefore, we propose that Group 1 knickpoints belong to the second tectonic perturbation in a two-stage linkage process in the center of the rift.

This inference agrees well with other observations in the central rift rivers (from Trikalitikos to Krios; Figs. 12 & 16A), where two river trunks (Fonissa and Krios) have an extra, fourth knickpoint at the highest location, closer to the drainage divide than any other river in the rift (Table 1). This is, drainage reversal initiated earlier or was more pronounced in the present central rift, capturing one or two sets of tectonic knickpoints from (now) beheaded rivers. This is consistent with a fault slip rate increase that was more pronounced or older in the central rift, that we frame as fault linkage between two of the larger fault segments of the Central Rift FA, probably the Derveni-Lykoporia F or the Onshore Xylokastro F. We consider that the upper set of tectonic knickpoints seen in Fonissa and Krios is also related to this increase in fault uplift rate, and hence correlated as Group 1 in Fig. 16C.

We suggest that Group 2, i.e. the upper set of tectonic knickpoints of central rift rivers (Skoupeiko, Dervenios) and the third highest of Fonissa (Fig. 16A), results from the effective linkage of the Central Rift FA. Under this scenario, this second increase in uplift rate would result in the eventual disconnection of former river systems and led to the uppermost tectonic knickpoints in Trikalitikos, and would occur either prior or perhaps coeval with the third highest set of knickpoints (Group 3) in the river networks in the west. We propose that connection with the Eliki FA farther east results in the knickpoints of Group 3, which appear almost everywhere along the rift. This proposal is supported by the relative higher elevation of this set in the Ladopotamos River (Fig. 16A). Group 4 lays at the lowest heights and show a common behaviour along the entire rift border fault that included river basins in the westmost rift sector. Regardless of the exact time-sequence of events, we understand that the elevated position of the lowest tectonic knickpoint of the Meganitis (Figs. 15 & 16) reflects the fast vertical upstream propagation of the erosional wave (knickpoint area) expected for a linkage area (see for example Gallen and Wegmann, 2017) due to increased throw/uplift rates (e.g., Whittaker and Boulton, 2012). Similarly, the high elevations of the Aigio F footwall relief with regards to the overall west-rising trend of the Aigio FA footwall relief (Fig. 15) suggest the mechanical interaction between the Aigio FA and Eliki FA. Taken together with the footwall relief plateau existing in the overlapping area of the Eliki FA and Aigio FA, our interpretation points to an “under-recovered” fault displacement profile and thus, a young linkage age (see theoretical framework; Fig. 14D). Moreover, the presence of solely two sets of tectonic knickpoints in the westernmost rivers, in comparison to the four sets found in rivers further east (with similar or larger drainage areas and reaching similar or larger maximum heights) supports that the aforementioned linkage took place by propagation (Fig. 14D right).

Table 2. *Data associated with the paleoshoreline angles and the Gilbert delta topsets, including assumed age and derived uplift rates. All names for the "Site" column are explained in Fig. 4. Sources of the data are marked as McNe (McNeill and Collier, 2004), DeMa (De Martini et al., 2004), Houg (Houghton et al., 2003) and Own (this contribution).*

Table 2

Object	Site	Source	X coord	Y coord	Level	Age (ka)	Elevat. (m)	Ze (m)	AbsUpliftRate
Paleoshoreline angle - Marine terraces	*Xy1*	Own	657252	4199244	MIS 5e	124	55.32	1.03	0.45
	Xy1	Own	657449	4197907	MIS 7e	240	108.35	0.46	0.45
	Xy1	Own	657276	4197519	MIS 9e	326	146.86	2.88	0.45
	Xy2	Own	643328	4213762	MIS 5e	124	177.23	0.47	1.43
	Xy2	Own	n.a	n.a	MIS 7e	240	347	5	1.45
	Xy2	Own	n.a	n.a	MIS 9e	326	471	5	1.44
	Ak	McNe	613223	4225224	MIS 5e	124	135	5	1.09
	Ak	McNe	613014	4224383	MIS 7e	240	240	5	1.00
	Ak	McNe	611975	4223875	MIS 9	326	350	5	1.07
	Ag1	McNe	600178	4228598	MIS 5e	124	150	5	1.21
	Ag1	McNe	599843	4228011	MIS 7e	240	255	5	1.06
	Ag1	McNe	599575	4227668	MIS 9	326	370	5	1.13
	Ag2	DeMa	592506	4233848	MIS 5e	124	160	5	1.29
	Ag2	DeMa	591685	4232525	MIS 7e	240	232	5	0.97
	Ag2	DeMa	590492	4231081	MIS 9	326	360	5	1.10
	Ps	Houg	575679	4241583	MIS 5e	124	95	5	0.77
	Ps	Houg	575625	4241270	MIS 7e	240	160	5	0.67
	Ps	Houg	575545	4241047	MIS 9e	326	240	5	0.74
Gilbert delta topsets-foreset contacts	*Ki*	Own	640560	4200259	-	700	1,192	35	1.70
	Ki	Own	647564	4205230	-	700	380	35	0.54
	Ki	Own	638068	4207654	-	700	893	35	1.28
	Mv	Own	624537	4212086	-	1000	1,751	35	1.75
	Mv	Own	625408	4209556	-	1000	1,604	35	1.60
	Mv	Own	619703	4211123	-	1000	1,285	35	1.29
	Ev	Own	620247	4214600	-	700	1,253	35	1.79
	Ev	Own	622593	4216435	-	700	1,032	35	1.47
	Ev	Own	619275	4216912	-	700	1,058	35	1.51
	Pl	Own	610754	4224444	-	700	394	35	0.56
	Pl	Own	611651	4223930	-	700	416	35	0.59
	Pl	Own	609534	4224008	-	700	659	35	0.94
	Pl	Own	610171	4223192	-	700	716	35	1.02
	VoE	Own	606786	4223762	-	700	739	35	1.06
	VoE	Own	605490	4223472	-	700	839	35	1.20
	VoE	Own	605032	4225862	-	700	557	35	0.80
	VoE	Own	604127	4224097	-	700	605	35	0.86
	VoW	Own	603985	4226231	-	700	403	35	0.58
	VoW	Own	601081	4226465	-	700	632	35	0.90
	VoW	Own	601539	4225371	-	700	839	35	1.20
	Ko	Own	597942	4225616	-	700	803	35	1.15
	Ko	Own	596556	4227337	-	700	1,005	35	1.44
	Ko	Own	593328	4225181	-	700	673	35	0.96
	Mg	Own	592568	4229459	-	700	510	35	0.73
	Mg	Own	590827	4227958	-	700	778	35	1.11
	Mg	Own	587353	4228953	-	700	580	35	0.83

5.3 Vertical motions in time

We attempt to reconstruct fault displacement profiles in time along the border fault strike (Fig. 17 & 18), and a schematic time evolution of fault footwall uplift along the rift (Fig. 19). We determine the relative footwall displacement near the fault occurring in the time lapse between uplifted sets of coeval morphotectonic markers formed at sea level using the difference in elevation between markers and their age. We project the sets of coeval morphotectonic makers towards the bounding fault strike (N105°E) (Figs. 9A,-B & 17; Table 2) and plot them together with footwall relief (section 4; Fig. 14). Potential errors and uncertainties that exist in the time reconstruction are relatively minor in comparison with the main tectonic signal at full-rift scale. See Suppl. material F for detailed description on data constraints, manipulation, errors and uncertainties in the reconstruction of vertical motions in time (Figs. 17, 18 & 19A).

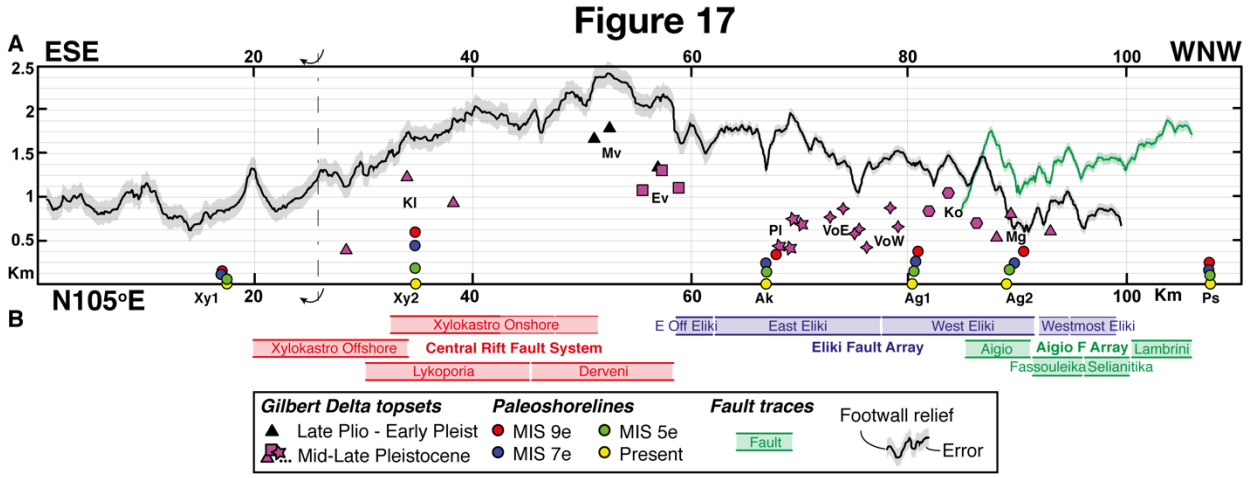

Fig. 17. *Projection along master fault strike (N105·E) of major morphotectonic features with known or correlated age with regards to the location of main fault segments.* ***(A)*** *Major morphotectonic elements of the master fault footwall and footwall relief. Filled circles represent the location of paleoshoreline angles of the MIS 5e (green), MIS 7e (blue) and MIS 9e (red) highstands of flights of marine terraces grouped by location. From E to W; Xy1 and Xy2, for Xylokastro area (paleoshoreline angles at low and maximum heights); Ak, for Akrata area; Aigio area, with Ag1 (paleoshoreline angles at the footwall of the Eliki FA) and Ag2 (with MIS 5e and MIS 7e at its hanging wall and MIS 9 at its footwall); and Ps for Psathopyrgos (based on Armijo et al., (1996); De Martini et al., (2004); Houghton et al., (2003); McNeill & Collier, (2004)). Circles with yellow fill are the present day shoreline angles simplified as modern sea level (at 0 m), and are used only as a reference for the reconstructions in Figs. 18 & 19. Distinct filled geometric symbols represent the projection of the highest, lowest, eastmost and westmost location of the topsets of each Gilbert delta, as mapped in Fig. 6. Gilbert-delta topsets of Pleistocene age are in purple, while black triangles represent the topsets of the Late Pliocene - Early Pleistocene Mavro Gilbert delta. Gilbert deltas are label from E to W as Kl (Klimenti), Mv (Mavro), Ev (Evrostini), Pl (Platanos), VoE and VoW (Vouraikos, east and west), Ko (Kolokotronis) and Mg (Meganitis). In all cases, symbols are larger than associated errors. Footwall relief is defined as in Fig. 15.* ***(B)*** *Approximate location and extent of the main fault segments in the direction of projection.*

Sets of contemporaneous marine terrace paleo-shorelines and Gilbert delta topset-foreset contacts have along-strike trends similar to those of footwall relief (Fig. 17), i.e. each set of correlatable morphotectonic markers has minimum heights in Xy1, maximum between Xy2 and Ak and intermediate heights between Ak and Ps. Correlatable morphotectonic markers thus point to self-similar vertical growth in the master fault since its onset with its nucleation point around the rift center (section 4; Figs. 13 & 14).

Overall, the reconstruction suggests at least ~100 m of onland uplift every ~110 ka all along the master fault footwall since its onset, except at the fault ends (Figs. 18A & 19A). We infer similar rates for the central rift between ~1 Ma and ~700 ka, while other areas along-strike lack footwall uplift during this period (Figs. 18A & 19A). Contrarily, footwall uplift seems to take place along the entire margin from ~700 ka to Present (Table 2; Fig. 14, D-right). Between ~700 ka and ~326 ka, a reconstructed onland uplift of ~60 m and ~90 m occurred every ~124 ka along most of the margin. We consider this inference with care, given the change in location, from Gilbert deltas to marine terraces, with respect to the bounding fault. The inferred vertical motion signal for this time frame lays almost flat, with larger heights at both ends. This unexpected signal for normal faults may be an artefact, as no motion is tracked farther along strike. Between 326 ka and 240 ka, the data has two maxima at ~150 m and ~135 m (Klimenti and Meganitis), and suggests a larger onland uplift for this period, which increases between 240 ka and 124 ka (Figs. 18A & 19A). Finally, between 124 ka and Present, onland uplift has two maximum, at ~180 m and ~155 m (Xylokastro 2 and Vouraikos West, respectively), and a minimum in Psathopyrgos at ~100 m. The overall profile is asymmetrical with the higher positions at the present rift center and lower elevations to the west.

Figure 18

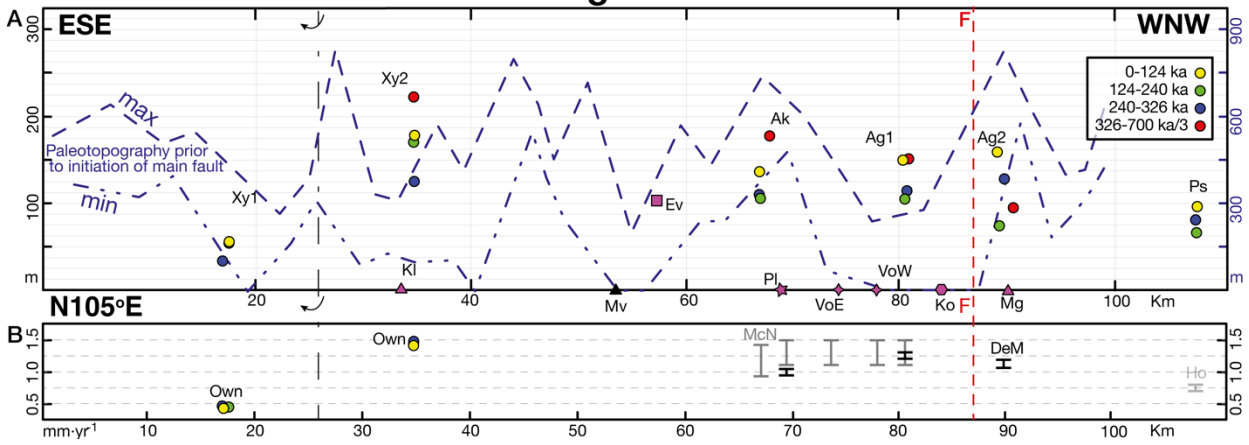

Fig. 18 (prev. page). *Flexure geometry and evolution in time of the rift-forming fault of the Corinth Rift along strike, marked by relative elevation and age constraints of footwall morphotectonic elements, and pre-fault paleotopography.* ***(A)*** *Reconstruction in time-frames of main fault relative vertical motions. Symbols represent the relative elevations between two consecutive sets of morphotectonic markers formed at sea level. We applied specific corrections to consecutive markers that represent longer time-steps to plot roughly equivalent time-steps (~110 ka). Yellow circles: Present to 124 ka (124 ka). Green: 240 ka to 124 ka (115 ka). Blue: 326 ka to 240 ka (91 ka). Red: ~700 ka to 326 ka / 3 (~123 ka). Purple symbols: ~1 Ma to ~700 ka / 3 (~100 ka). Envelopes of estimated maximum and minimum paleotopography prior to the formation of the main fault are shown as a blue line with triple vertical scale.* ***(B)*** *Uplift rates of the marine terraces during aforementioned time frames and equivalent colors to those in panel (A) for own analysed terraces, and proposed ranges of uplift rates from Houghton et al., 2003 (Ho), McNeill and Collier, 2004 (McN) and DeMartini et al., 2003 (DeM).*

6 Discussion on rift models and implications

6.1 Mechanical model of the modern Corinth Rift

The wavelength and amplitude of the master fault elastic flexure and footwall uplift (Figs. 10, 11, 17 & 18) can only be produced by steep planar faults (e.g., McNeill et al., 2005; Bell et al., 2011), reaching at least the brittle-ductile transition (Bell et al., 2017) (Fig. 5A) and developing in a strong lithosphere (King and Ellis, 1990; Buck, 1991, 1993; Resor and Pollard, 2012) (Figs. 1A & 19B). High uplift-subsidence ratios along the rift margin (McNeill and Collier, 2004) as well as a localised Moho rise (Zelt et al., 2005; Sachpazi et al., 2007; Pearce, 2015) further support this conclusion. Finally, fault down-dip depths derived with displacement-length ratios (Walsh and Watterson, 1988; Cowie and Scholz, 1992a, 1992b; Dawers et al., 1993) that use at-surface length and dip also suggest the border fault transects the seismogenic layer (~10-15 km), thus significantly surpassing depth of proposed detachments (~3-9 km) (e.g., Rigo et al., 1996; Sorel, 2000). Collectively, our evidence fails to support detachment fault geometries and thus, detachment models (e.g., Rietbrock et al., 1996; Rigo et al., 1996; Briole et al., 2000; Flotté and Sorel, 2001; Jolivet et al., 2010) that may apply further to the SE and in SW Turkey (Jolivet and Brun, 2010; Jolivet et al., 2013).

Fig. 19. *Time-evolution of the master fault footwall along strike (A), and its implication for the Corinth Rift formation (B).* ***(A)*** *Time-evolution of displacement profiles at ~110 ka. Each line represents a displacement profile of the master fault above a sea level, drawn joining the data points shown in Fig. 18, assuming continuity and smooth profiles among them. Each displacement profile represent ~110 ka. To maintain these comparable time-steps in the top two panels, we derived unconstrained profiles from the first constrained displacement profile by simple vertical addition 2 and 3 times, respectively.* ***(B)*** *Non-to-scale conceptual representation of Corinth Rift development in relation with a high-angle, propagating fault and its associated elastic flexure (left) and, in relation with a hypothetical detachment fault not supported by our data (right).*

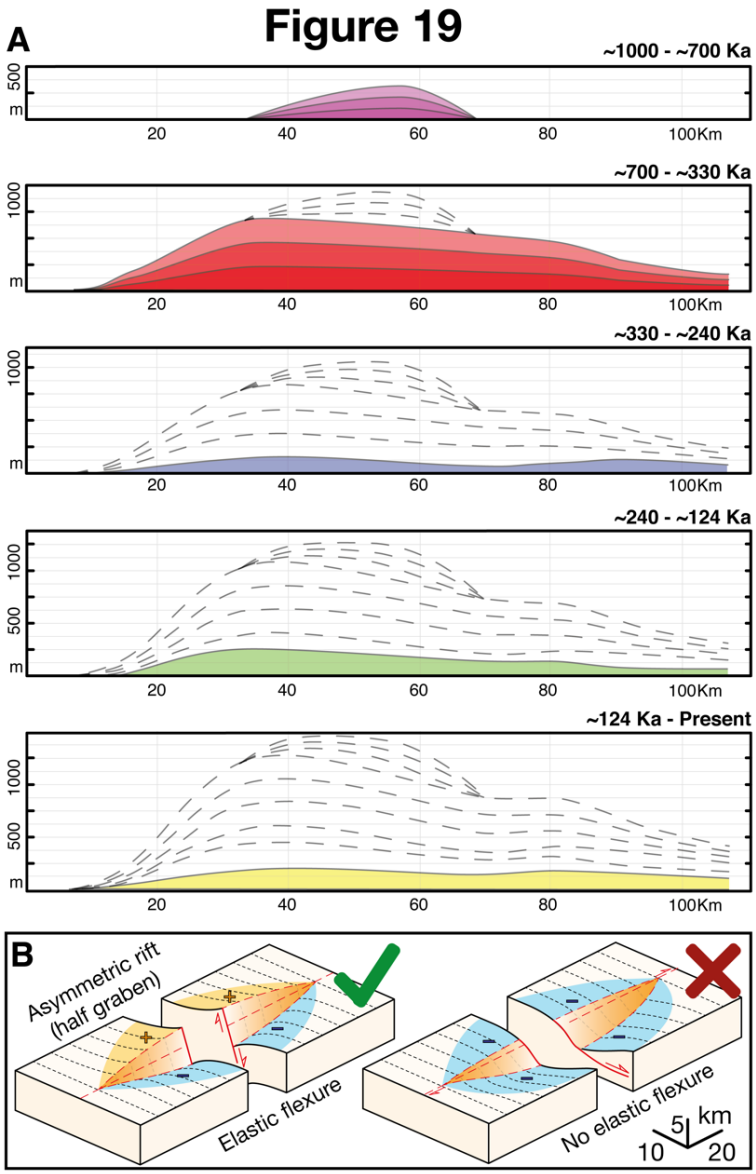

6.2 Evolutionary model of the Corinth Rift

Elastic flexure and fault dimensions, along-strike propagation and fast associated uplift rates since the onset of activity in the border fault suggest its growth halted early distributed extension in the area (Figs. 15 to 20). This is reported by correlations, geometrical relationships and spatiotemporal variations of geologic and geomorphologic features with the border fault at the scale of the entire rift (Figs. 8, 9E, 10, 11). Similarly, the along-strike dimensions and estimated vertical offsets of antecedent faults are small (e.g., Ori, 1989; Ford et al., 2012) when compared to the ~80-to-130 km along-strike length (Figs. 6 & 8), and ~4.8 km vertical offset along the active fault system (De Gelder et al., 2019). Also, whereas paleo-relief estimates with

mean elevations of ~300 m and maxima of ~700 m (Fig. 18) points to <1 km antecedent topography, the topography of the modern margin surpasses these heights often <10 km away from the border fault. Further, the distributed extension rates <1 mm×yr^{-1} accommodated by antecedent parallel faults for >3-4 Myr since extension onset (Ford et al., 2012) are at present more than one order of magnitude larger throughout the rift (>11 mm×yr^{-1}; Avallone et al., 2004) and highly localised in the rift-forming fault. We take our data and interpretation together with the observation that antecedent faults in the eastmost rift are cross-cut by the younger fault system (Figs. 6 & 8) to infer disruptive growth of a new steep border fault and a two-phase rift growth model.

We reconstruct the opening of the Corinth Rift since its onset, acknowledging our new findings and integrating them with previous studies (Fig. 20). Constraints prior to modern master fault onset come largely from other research and the reader is referred there for further details.

6.2.1 Antecedent distributed extension

Distributed extension tipping out to the west over Hellenic paleo-topography initiated <5 Ma (Fig. 20A) (e.g., Keraudren and Sorel, 1987; Doutsos and Piper, 1990; Rohais et al., 2007; Ford et al., 2016; Gawthorpe et al., 2017b). Distributed normal faulting may have started between 5 and 3.6 Ma south of the present rift (e.g., Collier, 1990; Collier and Dart, 1991; Leeder et al., 2008). Extension rates decreased westwards from estimates of 1.5-2.3 mm×yr^{-1} in the center to 0.6-1 mm×yr^{-1} in the west rift (e.g., Ford et al., 2016), suggesting a diachronic extension onset that tipped out to the west (Ford et al., 2012; Gawthorpe et al., 2017b). Well-established catchments drained N-to-NE inherited Hellenic paleotopography regionally plunging east, while local hanging-walls controlled along-strike sedimentary flow paths (Ford et al., 2012; Hemelsdaël and Ford, 2016; Gawthorpe et al., 2017b). The aforementioned evidence agrees well with the distributed extension at the NW tip of a south-arched extensional trough developing due to the Hellenic slab rollback.

New N- and S-dipping faults led to less distributed extension (Bell et al., 2009; Taylor et al., 2011; Nixon et al., 2016) after a ~10-30 km northward shift in extension locus at ~2 Ma (Fig. 20B) (e.g., Rohais et al., 2007; Leeder et al., 2008; Bell et al., 2009; Ford et al., 2009, 2012, 2016; Gawthorpe et al., 2017b). Fault migration poorly dated between ~2.2 and ~1.8 Ma (Malartre et al., 2004; Rohais et al., 2007 a, b; Leeder et al., 2008) resulted in a more-symmetrical extensional area that narrowed westward (e.g., Ford et al., 2016; Gawthorpe et al.,

2017b), suggesting potential diachronic onset of fault activity initiating earlier in the central rift (Gawthorpe et al., 2017a). Fault systems in the central rift (Central Rift FA) initiated at modern margin positions (Bell et al., 2009; Nixon et al., 2016) and have accumulated slip since then (Figs. 17 to 20; Ford et al., 2016). The Central Rift FA accumulated ~1/4 of its throw during this time (Nixon et al., 2016). The border fault system propagated west in a graben that narrowed from ~20-25 km in the center to ~10-15 km in the west (Ford et al., 2016). The fluvial network changed to N-flowing rivers that started reworking footwall uplifted sediments and Gilbert deltas formed in new hanging-walls (e.g., Ford et al., 2016; Gawthorpe et al., 2017b). For example, the Ilias and Evrostini deltas developed foresets of hundreds of meters after its feeding river cannibalised previously-depositing Killini and Mavro deltas (Ford et al., 2016). Evolution during this time frame is compatible with further entrenchment, westward propagation and southward arching of the Aegean detachment-led trough.

6.2.2 Change in extension mechanics

A basin-wide unconformity and sedimentation switch (e.g., Ori, 1989; Sachpazi et al., 2003) at ~800-600 ka (e.g., Ford et al., 2016; Nixon et al., 2016; Gawthorpe et al., 2017b) resulted from an abrupt onset of activity along the master fault and associated increase in rates of slip and associated vertical motions at rift scale (Fig. 20; Armijo et al., 1996). Over the short time span of ~300 ka, the antecedent complex and distributed rift structure shifted to the modern markedly asymmetrical rift growing in relation with N-dipping faults in the southern flank (Fig. 9D,-E; Figs. 8c and 11c in Nixon et al., 2016). During this tectonic event, fault activity focused on the Central Rift FA (Figs. 16 to 20), increased in the eastern Perachora and East Alkyonides faults (Nixon et al., 2016) and initiated in the western Eliki FA (e.g., Ford et al., 2016; Gawthorpe et al., 2017b) as well as in both Eratini faults (e.g., McNeill et al., 2005; Bell et al., 2008, 2009). Concomitantly, all antecedent faults of the southern margin died (Gawthorpe et al., 2017b) while S-dipping faults in the northern margin, like the Galaxidi Fault, significantly decreased activity and eventually deceased (Bell et al., 2008, 2009; Nixon et al., 2016). During this tectonic event, the dynamics of rift growth radically changed from slow-growing distributed faults to fast-growing elongated features that linked along strike to set the modern rift margin (Figs. 17 to 20). Border fault along-strike propagation consequently shuts down the activity of faults in its footwall while kinematically controlling relatively minor faults dipping against it.

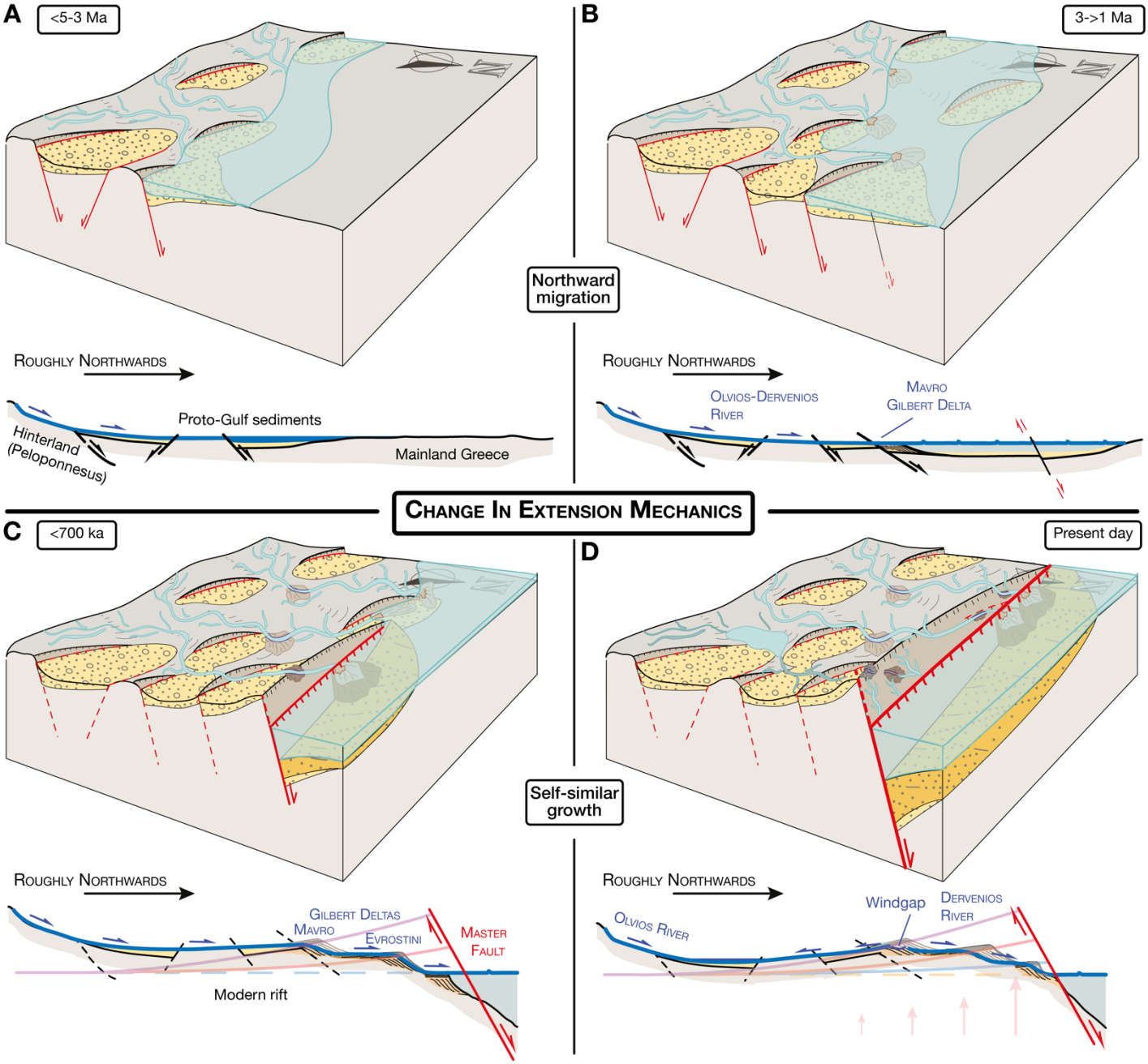

Fig. 20. *Conceptual evolutionary model in schematic 3D views (top) and cross-sections (bottom), with time steps:* ***(A)*** *<5 to 3 Ma and* ***(B)*** *3 to >1Ma,* ***(C)*** *<700 ka and* ***(D)*** *Present. Upper panels show the evolution from distributed extension along several normal faults and their associated low-amplitude vertical motions (A & B) to highly-localized extension along a new single fault and high-amplitude vertical motions associated to its disruptive growth (C & D). Bottom panels show a conceptual time-evolution of the footwall elastic flexure of the master fault in the centre of the rift and the associated evolution of Gilbert delta(s) and river profile(s) (near the frontal section in the 3D views of the top panels, and roughly at the location shown in Fig. 7). Drainage reversal is not specifically constrained, and could have taken place anytime after ~700 ka.*

6.2.3 The advent of the modern Corinth Rift

The change in extension mechanics and an abrupt increase in tectonic rates occurred diachronically as a new rift-forming fault grew by propagation, linking individual faults along-strike (Fig 20C, -D). We suggest that the Derveni, Lykoporia and Offshore Xylokastro faults linked into the Central Rift FA that became the principal focus of extension (Fig. 16; section 5.2). Here, fast fault lengthening and concomitant footwall flexure leads to the development of new footwall relief (Figs. 16 to 20), the abandonment and eventual perching of deltas, and disruption and reversal of large drainages (Fig 20D). In the central rift, the abandonment of the Evrostini delta and the defeat of its feeding river is estimated to have occurred some time after ~700 ka (Rohais et al., 2007; Ford et al., 2016). Lesser footwall relief existed in the west rift (Figs. 17 to 20) where homologous syn-rift deltas remained at hanging-wall positions of the bounding fault (Gawthorpe et al., 2017a). Here, rivers cannibalized their Gilbert deltas and the pre-rift units, and continue to flow north (Ford et al., 2016; Gawthorpe et al., 2017b), probably due to a relatively younger uplift rate change (Fig. 12). In other words, the master fault time-transgressive propagation along strike from the rift centre results in differential rift margin response and asymmetric fault footwall flexure (cf. Fig. 20C & 20D). This is readable in the heights of terraces and delta topsets, as well as the extent of the uplifted basin (Fig. 9A,-B,-C), the rift variable topography (Figs. 10 & 11), and the profiles of gulf-draining rivers (Fig. 12).

Rift across-axis asymmetry since ~400-300 ka (Nixon et al., 2016; Gawthorpe et al., 2017b) is sustained by high uplift rates in rift-forming faults propagating along-strike (Fig. 18). Subsidence and deposition of linked depocenters in the hanging-wall (Nixon et al., 2016) and the growth of footwall relief (Figs. 16 to 20) is controlled by north-dipping faults bounding the rift to the south. High uplift/subsidence ratios of 1:1.2-2.4 for the central rift (De Gelder et al., 2019) and 1:1.2-2.2 for the west rift (McNeill et al., 2005) result from highly localised strain and elastic flexure in the master fault (Fig. 8 & 20). Flexural uplift lead to uplift rates that surpass 1 $mm \times yr^{-1}$ along most of the rift, with the exception of its tips (Fig. 18B). The advent of rapid rates is coherent with a change in extension rates from ~1-2 $mm \times yr^{-1}$ to ~11-16 $mm \times yr^{-1}$ (Avallone et al., 2004; Ford et al., 2016). Overall relative low tectonic rates before ~700 ka might be related with slow growth of depocenters and regional uplift, while remarkably high tectonic rates at present along most of the margin relate with fault flexure and fast growth of an asymmetric rift basin.

Further master fault westward propagation along strike initiated the Aigio FA and the Psathopyrgos F. Here, fault activity started as well in the Marathias and Nafpakos faults of the

northern margin (Beckers et al., 2015). This resulted in a second unconformity in the area (Bell et al., 2008) and the opening of the Rion Strait at equivalent times (Ford et al., 2016). Flattening of the footwall relief profile in the west and the reduced number of tectonic knickpoints (Figs. 16 & 17) suggest fault activity in the area results from westward propagation of the master fault (Fig. 14). Changes in elevation of the longitudinal river profile major inflexions and the reduced magnitude of related river channel steepening are also consistent with this inference (Fernández-Blanco et al., 2019). Further supporting evidence are the recent hanging-wall uplift in the footwall of the Aigio F (Palyvos et al., 2005) and its age (50-60 ka; Cornet et al., 2004), as well as the large seismicity in the Aigio, Fassouleika and Psathopyrgos faults (Bernard et al., 2006; Boiselet et al., 2014; Duverger et al., 2018). Eastwards propagation is likely to have occurred at younger times than those suggested by Leeder et al. (2012). Activity of the easternmost faults is clearly evidenced by Holocene and historic fault ruptures in the Alepohori and Pisia faults (Jackson et al., 1982; Hubert et al., 1996; Mechernich et al., 2018) as well as in antithetic Kapareli Fault (Benedetti et al., 2003), and is probably limited in extent by mechanical restrictions further east, which we speculatively relate with the near-orthogonal orientation of faults belonging to the antecedent detachment-led trough.

6.2.4 The modern Corinth Rift at present

Continued self-similar growth of the master fault sets the modern Corinth Rift asymmetry, localising strain during its along strike propagation (Fig. 20D). Individual fault segments grew from the modern central rift along strike, and linked to form larger faults that eventually coalesced into the current master fault. In this sense, Nixon et al., 2016 suggest that full fault linkage occurred at ~130 ka. The master fault kinematic link at depth results in subsidence distributions (Nixon et al., 2016) and footwall relief (Fig. 16) that shows rift-scale parabolic shapes flattened to the west. Given that the master fault grew in a self-similar fashion, footwall-uplifted coeval morphotectonic features distributed self-consistently along the margin (Figs. 17), leading to a highly-localised asymmetric rift (Fig. 19B) (De Gelder et al., 2019). The rift asymmetry is marked along a northward transect by up-flexed topography with a border faults footwall width of ~15 km (Fig. 10) near its maximum footwall relief ~2.5 km (Fig. 16A) followed by pronounced syntectonic sedimentary wedges opening southwards (e.g., Taylor et al., 2011) and a northern coast dominated by subsidence (Bell et al., 2009; Elias et al., 2009). Contrarily to the above, symmetric cross-sectional geometries are maintained at both rift ends. Border fault growth lead to the development of new symmetrical rift sectors along the sense of

propagation, bounded by opposite-dipping faults, with active south-dipping faults in the northern rift margin (Benedetti et al., 2003; McNeill et al., 2005). Further propagation and strain localisation along the north-dipping border fault plane eventually overwrites these new rift sectors as their bounding faults link kinematically with the master fault. This transgressive switch in rift structural style is recorded in the along-strike differential rift geometry (Bell, 2008), and is documented in the west rift, albeit ascribed to westward rift propagation and northward fault migration (Ford et al., 2016).

In the west rift, strain is distributed among a few steep opposite-dipping faults (Nixon et al., 2016) where the youngest, ongoing propagation of the master fault takes place (Figs. 15, 16, 19 & 20). The west rift has the highest geodetic extension rates recorded for the rift (e.g., Avallone et al., 2004) and a north-dipping microseismicity layer with very high seismicity (Lambotte et al., 2014). Both features contrast with the relatively minor antecedent extensional strain for the area (e.g., Bell et al., 2011). The Aigio and Fassouleika faults show normal focal mechanisms dipping ~45° and 60° north at the interface with the microseismicity layer (Duverger et al., 2015). We speculate that if this layer is a low-dipping detachment of the antecedent extensional system (Rietbrock et al., 1996; Rigo et al., 1996), the new high-angle rift-forming fault documented here is in the process of transecting it at present. This would imply that the westernmost rift holds at depth the interface between the antecedent, distributed extension and the localised, modern Corinth Rift. Being this the case, both the high seismicity and the anomalously high geodetic extension rates in the area would result from the mechanical interaction between both faults and their summed capabilities to accommodate extensional strain. This hypothesis agrees as well with the quick decrease in Moho depth westwards (Zelt et al., 2005; Sachpazi et al., 2007; Pearce, 2015), as the modern rift-forming fault affecting the entire crust at its centre (Fig. 5A; section 5.2) tapers out towards its tips.

6.3 Tectonic implications

Our comprehensive model is compatible with early distributed extension at the northwestern tip of a detachment-controlled extensional through of the Aegean, followed by strain-localized, disruptive growth of a new fault system in relation to changes in external tectonic forcing. In other words, the early phase has an evolutionary structural style that can be explained by the self-organisation of a fault network known in continental settings (Cowie, 1998; Cowie et al., 2000, 2006; Gawthorpe et al., 2003, 2017b). Contrarily, the second phase involves drastic and

fast changes in normal fault dynamics in relation with the Corinth Rift tectonic setting (Armijo et al., 1996; Flerit et al., 2004; this contribution). The above supports the 'two-phase linear-elastic' Aegean model by which transtensional stresses, lead by the southwestward propagating tip of the North Anatolian lithospheric transform, are superimposed onto pre-existing extensional structures that guided the growth of new extensional fault systems (Hubert-Ferrari et al., 2003; Armijo et al., 2004; Flerit et al., 2004).

Our data supports that the modern Corinth Rift is a short-lived flexural cantilever rift (Fig. 17C) sustained by active seismicity during many earthquake cycles (King et al., 1988; Kusznir et al., 1991). Simulations constrained with coeval, elastically flexed time-strain markers across the border fault in the east rift, reproduce such flexure by coseismic strain along a 40°-60° planar normal fault, and postseismic viscous relaxation at the basal lower crust or upper mantle (De Gelder et al., 2019). These models suggests that continental lithosphere responding to fast, localized tensional strain on 10^3-10^4 yr timescales may be defined by rheologies holding significant strength for similar timescales (De Gelder et al., 2019). Similar U:S ratios at the Eliki FA location (McNeill et al., 2005) hint that a similar rheology may occur in the west rift. Evidence shown here, like the geometry and wavelength of rift margin topography, and its coherency in time with correlatable geological and geomorphological evidence (Figs. 9 to 11, 15, 16, 17C), supports significant long-term strength (Fig. 1, upper row) at the scale of the entire Corinth Rift, and since border fault onset (~10^6 yr).

Upper-crust and whole-crust extension estimates (Bell et al., 2011) suggest pure-shear (McKenzie, 1978b) during early extension in the area. This extension mechanism would imply a lithosphere with elevated rheological strength (e.g., Ziegler, 1988; Buck, 1991; Brun, 1999) also before the new border fault, suggesting a constant behaviour of the continental lithosphere under the Corinth Rift. Alternatively, early extension in relation to low-angle detachment(s) preceding a core-complex (Jolivet et al., 2010) would suggest combined shear (Barbier et al., 1986) or simple shear (Wernicke, 1981) and an overall weak continental lithosphere, as that of the central Aegean (Lister et al., 1984; Brun and Sokoutis, 2010; Jolivet et al., 2013). The discontinuation of viscous deformation by strain localisation and elastic failure of the continental lithosphere would imply strengthening of the lower crust and/or upper mantle in short time frame. Severe changes in composition or geothermal gradient that could explain such lower crust mechanical strengthening (Déverchère et al., 2001) are unlikely in ~10^6 yr timescales at rift scale. We thus favour that, if such change exists, it may relate with a relevant

increase in the near-field stresses, probably driven by an increase in earthquake activity in the seismogenic zone (Jamtveit et al., 2018).

7 Conclusions

This review reconstructs in detail the growth of an active rift border fault at the scale of an entire intracontinental rift, to provide constraints on rift evolution and mechanics, and understand its first-order lithosphere behaviour. To that end, we reviewed and re-assessed previous research in the Corinth Rift, as well as studies on the use of tectono-morphological approaches to constrain fault mechanics. This allows us to (i) use the rich record of strain markers and morphotectonic elements along the uplifting, southern margin of the Corinth Rift, and (ii) put forward a novel theoretical framework to characterise the lateral and vertical evolution of normal faults from the geomorphology of their footwalls. By these means, we characterise the kinematics and the evolution of the rift-forming fault, and propose a mechanical and evolutionary model for the rift. Similar frameworks and geomorphic compilations can be used to constrain the evolution of other active normal faults, and thus the growth and evolution of early rifting of continents elsewhere.

The active Corinth Rift border faults form a single composite master fault >80 km-length. Footwall relief is roughly symmetrical with a single maximum in fault throw, located in the Mavro area and correlated with the Central Rift FA, and its along-strike decay (Fig. 16A). Using fault footwall relief as a proxy for fault displacement profile (see section 4.1, Figs. 7 & 13) implies that discrete en-échelon surficial fault segments (Fig. 8) are hard-linked into a kinematically coherent fault at depth, that extends along strike, ad minimum, from the eastern end of Offshore Xylokastro F to the Westernmost Eliki F (Fig. 16A). This signal is also reflected in the decay in topographic and relief heights (Figs. 8, 9), the morphology of footwall catchments (Fig. 11A), and the along-strike heights of coeval marine terraces and perched Gilbert deltas (Figs. 9A,-B, 16 & 17), among other things. Such rift-scale displacement profile is coherent with a single, high-angle, composite master fault that has estimated down-dip depths well below the seismogenic layer.

The master fault grew from the rift center by simple linkage of individual faults into larger systems, and by propagation integrating younger, collinear faults along strike. Successive linkage of individual fault strands into larger fault segments is indicated by the overall correlation between individual fault segments and up-pointing triangles in the footwall

relief that compound triangles of larger wavelengths (cf. Fig. 16A & Fig. 16B; section 4). We infer that the Central Rift FA is the oldest fault segment of the rift master fault, for it has the largest along-strike lengths at surface (Figs. 8), maximum relief offset (Fig. 10) and footwall relief (Fig. 16A), and maximum fault displacement (Fig. 5A). We deduce along-strike propagation of border fault activity westwards, integrating the Eliki FA, and more recently, the Aigio FA (Figs. 13 & 14). Such westward propagation is primarily manifested by the asymmetry of its fault displacement profile in couple with the absence of tectonic knickpoints in catchments to the west. More specifically, the single-fault displacement profile is flat, and thus "unrecovered" in its westernmost end, where the along-strike correlation among tectonic knickpoints that is valid for the rest of the rift is not valid (Figs. 14 to 16).

We propose a sequence of fault growth and evolution that opens of the rift in time. Coupling footwall relief and tectonic knickpoints (Fig. 16) with fault displacement profiles in time (Fig. 18A) within the context of our theoretical framework (Fig. 14) allow us to propose a sequence of events: (i) initiation of individual fault segments in the central sector; (ii) growth and simple linkage of fault segments in the central rift, and initiation of individual fault segments in the west; followed by (iii) connection by simple linkage into the composite Central Rift FA in the rift centre, and that of the Eliki FA in the west rift; (iv) connection of both fault systems; and (v) propagation farther west, with the inclusion of the Aigio Fault Array in recent times.

The diachronic along-strike growth of rift border fault controls the modern rift along- and across-axis asymmetry (Figs. 8 to 12). The relationship between the envelope of maximum relief in drainage and maximum relief at ~21 km from the border fault (Figs. 11 & 18) suggests ~50-to-75% of the main margin topography is related to the current border fault, i.e. that ~1/2-to-3/4 of the present topography developed since the modern border fault onset, and thus in ~1/5 of the time since the onset of extension in the area (~700 ka out of 4-5 Ma). Most other features in the modern rift are also controlled by the border fault; from rift basin extent and geometry to the size and distribution of synsedimentary wedges, from the morphology of river catchments to the location and extent of coeval marine terraces and perched Gilbert deltas with respect to the border fault system (Figs. 6, 8 to 12, 15 to 18). Given that these features allow us to track the activity of active surficial fault segments back to border fault onset (Figs. 16 to 19A), this evidence collectively suggests that the border fault grew rapidly and controls the modern rift evolution, and implies that the antecedent distributed extension for the preceding ~4 My is subsidiary in the formation of the modern rift.

We propose a comprehensive two-phase rift growth model (Fig. 20). Distributed extension occurred symmetrically and at low rate atop the Hellenic basement since the Early Pliocene. During ~4 My, this extended area progressively migrated northwards and further entrenched westward. At ~800-600 ka, an abrupt tectonic event (spanning for ~300 ky) radically changed extension mechanics, and the resulting rift geometry and tectono-sedimentary dynamics. Since Middle Pleistocene, the synchronous onset of asymmetric rifting occurs at fast rates as the new fault system grows along strike from the present rift centre. This rift-forming fault, which correlates in length with the along-strike extent of the present rift, controls the active tectonics, morphology and geology of the rift to a first-order, indicating that its growth drives the modern Corinth Rift opening in time and its present-day rates and scale.

Acknowledgements

We thank reviewers Laurent Jolivet and Douwe J.J. van Hinsbergen for their comments and suggestions that improved the original version of the manuscript, and the skilled editorial management. We thank Dimitris Sakellariou for kindly providing the bathymetric data, and Sotiris Valkaniotis and Dimitris Papanastassiou for the seismic catalogues of the Corinth Rift Laboratory and University of Athens, respectively. We thank Conrad Childs for discussions on fault mechanics, and Rebecca Bell and Sean Gallen for proof reading the text. The research leading to these results received funding from the People Programme (Marie Curie Actions) of the European Union's Seventh Framework Programme under the ITN project ALErT (Grant FP7-PEOPLE-2013-ITN number 607996) and by the ISIS program of CNES. This study contributes to the IdEx Universit. de ParisANR-18-IDEX-0001. This is IPGP contribution 4061.

References

Allmendinger, R.W., Sharp, J.W., Von Tish, D., Serpa, L., Brown, L., Kaufman, S., Oliver, J., Smith, R.B., 1983. Cenozoic and Mesozoic structure of the eastern Basin and Range province, Utah, from COCORP seismic-reflection data. Geology 11, 532–536. doi:2.0.CO;2">10.1130/0091-7613(1983)11<532:CAMSOT>2.0.CO;2

Ambraseys, N.N., Jackson, J.A., 1990. Seismicity and associated strain of central Greece between 1890 and 1988. Geophys. J. Int. 101, 663–708.

Anders, M.H., Schlische, R.W., 1994. Overlapping Faults, Intrabasin Highs, and the Growth of Normal Faults. J. Geol. 102, 165–179. doi:10.1086/629661

Anderson, R.S., Densmore, A.L., Ellis, M.A., 1999. The generation and degradation of marine terraces. Basin Res. 11, 7–19.

Armijo, R., Flerit, F., King, G., Meyer, B., 2004. Linear elastic fracture mechanics explains the past and present evolution of the Aegean. Earth Planet. Sci. Lett. 217, 85–95. doi:10.1016/S0012-821X(03)00590-9

Armijo, R., Lacassin, R., Coudurier-Curveur, A., Carrizo, D., 2015. Coupled tectonic evolution of Andean orogeny and global climate. Earth-Sci. Rev. 143, 1–35.

Armijo, R., Lyon-Caen, H., Papanastassiou, D., 1991. A possible normal-fault rupture for the 464 BC Sparta earthquake. Nature 351, 137–139. doi:10.1038/351137a0

Armijo, R., Meyer, B., Hubert, A., Barka, A., 1999. Westward propagation of the North Anatolian fault into the northern Aegean: Timing and kinematics. Geology 27, 267. doi:2.3.co;2">10.1130/0091-7613(1999)027<0267:wpotna>2.3.co;2

Armijo, R., Meyer, B., King, G.C.P., Rigo, A., Papanastassiou, D., 1996. Quaternary evolution of the Corinth Rift and its implications for the Late Cenozoic evolution of the Aegean. Geophysical Journal International 126, 11–53. doi:10.1111/j.1365-246x.1996.tb05264.x

Armijo, R., Tapponnier, P., Mercier, J.L., Han, T.-L., 1986. Quaternary extension in southern Tibet: Field observations and tectonic implications. J. Geophys. Res. 91, 13803–13872. doi:10.1029/JB091iB14p13803

Attal, M., Tucker, G.E., Whittaker, A.C., Cowie, P.A., Roberts, G.P., 2008. Modeling fluvial incision and transient landscape evolution: Influence of dynamic channel adjustment. J. Geophys. Res. 113, F02010. doi:10.1029/2007JF000893

Avallone, A., Briole, P., Agatza-Balodimou, A.M., Billiris, H., Charade, O., Mitsakaki, C., Nercessian, A., Papazissi, K., Paradissis, D., Veis, G., 2004. Analysis of eleven years of deformation measured by GPS in the Corinth Rift Laboratory area. C. R. Geosci. 336, 301–311. doi:10.1016/j.crte.2003.12.007

Barbier, F., Duvergé, J., Le Pichon, X., 1986. Structure profonde de la marge Nord-Gascogne. Implications sur le mécanisme de rifting et de formation de la marge continentale. Bull. Cent. Rech. Explor. Prod. Elf Aquitaine 10, 105–121.

Beckers, A., Hubert-Ferrari, A., Beck, C., Bodeux, S., Tripsanas, E., Sakellariou, D., De Batist, M., 2015. Active faulting at the western tip of the Gulf of Corinth, Greece, from high-resolution seismic data. Mar. Geol. 360, 55–69. doi:10.1016/j.margeo.2014.12.003

Bell, R.E., 2008. Tectonic evolution of the Corinth Rift (phd). University of Southampton.

Bell, R.E., Duclaux, G., Nixon, C.W., Gawthorpe, R.L., McNeill, L.C., 2017. High-angle, not low-angle, normal faults dominate early rift extension in the Corinth Rift, central Greece. Geology. doi:10.1130/g39560.1

Bell, R.E., McNeill, L.C., Bull, J.M., Henstock, T.J., 2008. Evolution of the offshore western Gulf of Corinth. Geol. Soc. Am. Bull. 120, 156–178. doi:10.1130/B26212.1

Bell, R.E., Mc Neill, L.C., Bull, J.M., Henstock, T.J., Collier, R.E.L., Leederz, M.R., 2009. Fault architecture, basin structure and evolution of the Gulf of Corinth Rift, central Greece. Basin Res. 21, 824–855. doi:10.1111/j.1365-2117.2009.00401.x

Bell, R.E., McNeill, L.C., Henstock, T.J., Bull, J.M., 2011. Comparing extension on multiple time and depth scales in the Corinth Rift, Central Greece: Extension across the Corinth Rift. Geophys. J. Int. 186, 463–470. doi:10.1111/j.1365-246X.2011.05077.x

Benedetti, L., Finkel, R., King, G., Armijo, R., Papanastassiou, D., Ryerson, F.J., Flerit, F., Farber, D., Stavrakakis, G., 2003. Motion on the Kaparelli fault (Greece) prior to the 1981 earthquake sequence determined from 36Cl cosmogenic dating. Terra Nova 15, 118–124. doi:10.1046/j.1365-3121.2003.00474.x

Berlin, M.M., Anderson, R.S., 2007. Modeling of knickpoint retreat on the Roan Plateau, western Colorado. J. Geophys. Res. 112, F03S06. doi:10.1029/2006JF000553

Bernard, P., Chouliaras, G., Tzanis, A., Briole, P., -P. Bouin, M., Tellez, J., Stavrakakis, G., Makropoulos, K., 1997. Seismic and electrical anisotropy in the Mornos Delta, Gulf of Corinth, Greece, and its relationship with GPS strain measurements. Geophysical Research Letters. doi:10.1029/97gl02102

Bernard, P., Lyon-Caen, H., Briole, P., Deschamps, A., Boudin, F., Makropoulos, K., Papadimitriou, P., Lemeille, F., Patau, G., Billiris, H., Paradissis, D., Papazissi, K., Castarède, H., Charade, O., Nercessian, A., Avallone, A., Pacchiani, F., Zahradnik, J., Sacks, S., Linde, A., 2006. Seismicity, deformation and seismic hazard in the western rift of Corinth: New insights from the Corinth Rift Laboratory (CRL). Tectonophysics 426, 7–30. doi:10.1016/j.tecto.2006.02.012

Boiselet, A., Scotti, O., Lyon-Caen, H., 2014. Estimating the probability of occurrence of earthquakes (M>6) in the Western part of the Corinth rift using fault-based and classical seismotectonic approaches, EGU General Assembly Conference Abstracts.

Boncio, P., Lavecchia, G., 2000. A structural model for active extension in Central Italy. J. Geodyn. 29, 233–244. doi:10.1016/S0264-3707(99)00050-2

Bonneau, M., 1984. Correlation of the Hellenide nappes in the south-east Aegean and their tectonic reconstruction. Geological Society, London, Special Publications 17, 517–527. doi:10.1144/GSL.SP.1984.017.01.38

Boulton, S.J., Whittaker, A.C., 2009. Quantifying the slip rates, spatial distribution and evolution of active normal faults from geomorphic analysis: Field examples from an oblique-extensional graben, southern Turkey. Geomorphology 104, 299–316. doi:10.1016/j.geomorph.2008.09.007

Brasier, A.T., Andrews, J.E., Kendall, A.C., 2011. Diagenesis or dire genesis? The origin of columnar spar in tufa stromatolites of central Greece and the role of chironomid larvae. Sedimentology 58, 1283–1302. doi:10.1111/j.1365-3091.2010.01208.x

Briole, P., Rigo, A., Lyon-Caen, H., Ruegg, J.C., Papazissi, K., Mitsakaki, C., Balodimou, A., Veis, G., Hatzfeld, D., Deschamps, A., 2000. Active deformation of the Corinth rift, Greece- Results from repeated Global Positioning System surveys between 1990 and 1995. Journal of Geophysical Research: Solid Earth 105, 25605–25625. doi:10.1029/2000jb900148

Brooks, M., Ferentinos, G., 1984. Tectonics and sedimentation in the Gulf of Corinth and the Zakynthos and Kefallinia channels, Western Greece. Tectonophysics 101, 25–54. doi:10.1016/0040-1951(84)90040-4

Brun, J.P., 1999. Narrow rifts versus wide rifts: inferences for the mechanics of rifting from laboratory experiments. Philosophical Transactions of the Royal Society of London A: Mathematical, Physical and Engineering Sciences 357, 695–709. doi:10.1098/rsta.1999.0349

Brun, J.-P., Faccenna, C., Gueydan, F., Sokoutis, D., Philippon, M., Kydonakis, K., Gorini, C., 2016. The two-stage Aegean extension, from localized to distributed, a result of slab rollback acceleration. Can. J. Earth Sci. 53, 1142–1157. doi:10.1139/cjes-2015-0203

Brun, J.-P., Sokoutis, D., 2010. 45 m.y. of Aegean crust and mantle flow driven by trench retreat. Geology 38, 815–818. doi:10.1130/G30950.1

Buck, W.R., 1991. Modes of continental lithospheric extension. J. Geophys. Res. 96, 20161–20178.

Buck, W.R., 1993. Effect of lithospheric thickness on the formation of high- and low-angle normal faults. Geology 21, 933–936. doi:2.3.CO;2">10.1130/0091-7613(1993)021<0933:EOLTOT>2.3.CO;2

Burov, E.B., Watts, A.B., Others, 2006. The long-term strength of continental lithosphere:“ jelly sandwich” or“ crème brûlée”? GSA Today 16, 4.

Cartwright, J.A., Trudgill, B.D., Mansfield, C.S., 1995. Fault growth by segment linkage: an explanation for scatter in maximum displacement and trace length data from the Canyonlands Grabens of SE Utah. J. Struct. Geol. 17, 1319–1326. doi:10.1016/0191-8141(95)00033-A

Causse, C., Moretti, I., Eschard, R., Micarelli, L., Ghaleb, B., Frank, N., 2004. Kinematics of the Corinth Gulf inferred from calcite dating and syntectonic sedimentary characteristics. C. R. Geosci. 336, 281–290. doi:10.1016/j.crte.2003.11.017

Charalampakis, M., Lykousis, V., Sakellariou, D., Papatheodorou, G., Ferentinos, G., 2014. The tectono-sedimentary evolution of the Lechaion Gulf, the south eastern branch of the Corinth graben, Greece. Mar. Geol. 351, 58–75. doi:10.1016/j.margeo.2014.03.014

Childs, C., Holdsworth, R.E., -L. Jackson, C.A., Manzocchi, T., Walsh, J.J., Yielding, G., 2017. Introduction to the geometry and growth of normal faults. Geological Society, London, Special Publications 439, 1–9. doi:10.1144/SP439.24

Clendenon, C., 2009. Karst hydrology in ancient myths from Arcadia and Argolis, Greece. Acta Carsologica 38.

Collier, R., Dart, C., 1991. Neogene to Quaternary rifting, sedimentation and uplift in the Corinth Basin,Greece. J. Geol. Soc. London 148, 1049–1065. doi:10.1144/gsjgs.148.6.1049

Collier, R.E.L.L., 1990. Eustatic and tectonic controls upon Quaternary coastal sedimentation in the Corinth Basin, Greece. J. Geol. Soc. London 147, 301–314. doi:10.1144/gsjgs.147.2.0301

Collier, R.E.L., Leeder, M.R., Rowe, P.J., Atkinson, T.C., 1992. Rates of tectonic uplift in the Corinth and Megara Basins, central Greece. Tectonics 11, 1159–1167. doi:10.1029/92TC01565

Cornet, F.H., Doan, M.L., Moretti, I., Borm, G., 2004. Drilling through the active Aigion Fault: the AIG10 well observatory. C. R. Geosci. 336, 395–406. doi:10.1016/j.crte.2004.02.002

Cowie, P.A., 1998. A healing–reloading feedback control on the growth rate of seismogenic faults. J. Struct. Geol. 20, 1075–1087. doi:10.1016/S0191-8141(98)00034-0

Cowie, P.A., Attal, M., Tucker, G.E., Whittaker, A.C., Naylor, M., Ganas, A., Roberts, G.P., 2006. Investigating the surface process response to fault interaction and linkage using a numerical modelling approach. Basin Res. 18, 231–266. doi:10.1111/j.1365-2117.2006.00298.x

Cowie, P.A., Gupta, S., Dawers, N.H., 2000. Implications of fault array evolution for synrift depocentre development: insights from a numerical fault growth model. Basin Res. 12, 241–261.

Cowie, P.A., Roberts, G.P., 2001. Constraining slip rates and spacings for active normal faults. J. Struct. Geol. 23, 1901–1915. doi:10.1016/s0191-8141(01)00036-0

Cowie, P.A., Scholz, C.H., 1992a. Physical explanation for the displacement-length relationship of faults using a post-yield fracture mechanics model. J. Struct. Geol. 14, 1133–1148. doi:10.1016/0191-8141(92)90065-5

Cowie, P.A., Scholz, C.H., 1992b. Displacement-length scaling relationship for faults: data synthesis and discussion. J. Struct. Geol. 14, 1149–1156. doi:10.1016/0191-8141(92)90066-6

Dawers, N.H., Anders, M.H., 1995. Displacement-length scaling and fault linkage. J. Struct. Geol. 17, 607–614. doi:10.1016/0191-8141(94)00091-d

Dawers, N.H., Anders, M.H., Scholz, C.H., 1993. Growth of normal faults: Displacement-length scaling. Geology 21, 1107–1110. doi:2.3.CO;2">10.1130/0091-7613(1993)021<1107:GONFDL>2.3.CO;2

De Gelder, G., Fernández-Blanco, D., Melnick, D., Duclaux, G., Bell, R.E., Jara-Muñoz, J., Armijo, R., Lacassin, R., 2019. Lithospheric flexure and rheology determined by climate cycle markers in the Corinth Rift. Sci. Rep. 9, 4260. doi:10.1038/s41598-018-36377-1

De Martini, P.M., Pantosti, D., Palyvos, N., Lemeille, F., McNeill, L., Collier, R., 2004. Slip rates of the Aigion and Eliki Faults from uplifted marine terraces, Corinth Gulf, Greece. C. R. Geosci. 336, 325–334. doi:10.1016/j.crte.2003.12.006

Densmore, A.L., Dawers, N.H., Gupta, S., Guidon, R., 2005. What sets topographic relief in extensional footwalls? Geology 33, 453–456. doi:10.1130/G21440.1

Densmore, A.L., Dawers, N.H., Gupta, S., Guidon, R., Goldin, T., 2004. Footwall topographic development during continental extension. J. Geophys. Res. 109, F03001. doi:10.1029/2003JF000115

Densmore, A.L., Gupta, S., Allen, P.A., Dawers, N.H., 2007. Transient landscapes at fault tips. J. Geophys. Res. 112, F03S08. doi:10.1029/2006JF000560

Déverchère, J., Petit, C., Gileva, N., Radziminovitch, N., Melnikova, V., San'Kov, V., 2001. Depth distribution of earthquakes in the Baikal rift system and its implications for the rheology of the lithosphere. Geophysical Journal International. doi:10.1046/j.0956-540x.2001.1484.484.x

Doutsos, T., Piper, D.J.W., 1990. Listric faulting, sedimentation, and morphological evolution of the Quaternary eastern Corinth rift, Greece: First stages of continental rifting. Geol. Soc. Am. Bull. 102, 812–829. doi:2.3.CO;2">10.1130/0016-7606(1990)102<0812:LFSAME>2.3.CO;2

Duverger, C., Godano, M., Bernard, P., Lyon-Caen, H., Lambotte, S., 2015. The 2003–2004 seismic swarm in the western Corinth rift: Evidence for a multiscale pore pressure diffusion process along a permeable fault system. Geophys. Res. Lett. 42, 2015GL065298. doi:10.1002/2015GL065298

Duverger, C., Lambotte, S., Bernard, P., Lyon-Caen, H., Deschamps, A., Nercessian, A., 2018. Dynamics of microseismicity and its relationship with the active structures in the western Corinth Rift (Greece). Geophys. J. Int. 215, 196–221. doi:10.1093/gji/ggy264

Ebinger, C.J., 1989. Geometric and kinematic development of border faults and accommodation zones, Kivu-Rusizi Rift, Africa. Tectonics 8, 117–133. doi:10.1029/TC008i001p00117

Elias, P., Kontoes, C., Papoutsis, I., Kotsis, I., Marinou, A., Paradissis, D., Sakellariou, D., 2009. Permanent Scatterer InSAR Analysis and Validation in the Gulf of Corinth. Sensors 9, 46–55. doi:10.3390/s90100046

Ferentinos, G., Georgiou, N., Christodoulou, D., Geraga, M., Papatheodorou, G., 2018. Propagation and termination of a strike slip fault in an extensional domain: The westward growth of the North Anatolian Fault into the Aegean Sea. Tectonophysics 745, 183–195. doi:10.1016/j.tecto.2018.08.003

Fernández-Blanco, D., de Gelder, G., Gallen, S., Lacassin, R., Armijo, R., 2019a. Transient rivers characterize evolving crustal-scale flexure in the Corinth Rift. Retrieved from EarthArXiv, January 10, 2019. doi:10.31223/osf.io/8w7kf

Fernández-Blanco, D., de Gelder, G., Lacassin, R., Armijo, R., 2019b. Geometry of flexural uplift by continental rifting in Corinth, Greece. Retrieved from EarthArXiv, August 10, 2019. doi:10.31223/osf.io/e6dp5

Flerit, F., Armijo, R., King, G., Meyer, B., 2004. The mechanical interaction between the propagating North Anatolian Fault and the back-arc extension in the Aegean. Earth Planet. Sci. Lett. 224, 347–362. doi:10.1016/j.epsl.2004.05.028

Flotté, N., Sorel, D., 2001. Structural cross sections through the Corinth-Patras detachment fault-system in Northern Peloponnesus (Aegean Arc, Greece). Bulletin of the Geological Society of Greece. doi:10.12681/bgsg.17018

Flotté, N., Sorel, D., Müller, C., Tensi, J., 2005. Along strike changes in the structural evolution over a brittle detachment fault: Example of the Pleistocene Corinth–Patras rift (Greece). Tectonophysics 403, 77–94. doi:10.1016/j.tecto.2005.03.015

Ford, M., Hemelsdaël, R., Mancini, M., Palyvos, N., 2016. Rift migration and lateral propagation: evolution of normal faults and sediment-routing systems of the western Corinth rift (Greece). Geological Society, London, Special Publications 439. doi:10.1144/SP439.15

Ford, M., Rohais, S., Williams, E.A., Bourlange, S., Jousselin, D., Backert, N., Malartre, F., 2012. Tectono-sedimentary evolution of the western Corinth rift (Central Greece). Basin Res. 0, 1–23. doi:10.1111/j.1365-2117.2012.00550.x

Ford, M., Williams, E.A., Malartre, F., Popescu, S.-M., 2009. Stratigraphic architecture, sedimentology and structure of the Vouraikos Gilbert-type fan delta, Gulf of Corinth, Greece. Sedimentary processes, environments and basins: A tribute to Peter Friend: Oxford, Blackwell Publishing Ltd 49–90.

Gallen, S.F., Wegmann, K.W., 2017. River profile response to normal fault growth and linkage: An example from the Hellenic forearc of south-central Crete, Greece. Earth Surface Dynamics 5, 161. doi:10.5194/esurf-5-161-2017

Gautier, S., Latorre, D., Virieux, J., Deschamps, A., Skarpelos, C., Sotiriou, A., Serpetsidaki, A., Tselentis, A., 2006. A New Passive Tomography of the Aigion Area (Gulf of Corinth, Greece) from the 2002 Data Set. Pure Appl. Geophys. 163, 431–453. doi:10.1007/s00024-005-0033-7

Gawthorpe, R.L., Andrews, J.E., Collier, R.E.L., Ford, M., Henstra, G.A., Kranis, H., Leeder, M.R., Muravchik, M., Skourtsos, E., 2017a. Building up or out? Disparate sequence architectures along an active rift margin—Corinth rift, Greece. Geology 45, 1111–1114. doi:10.1130/G39660.1

Gawthorpe, R.L., Fraser, A.J., Collier, R.E.L., 1994. Sequence stratigraphy in active extensional basins: implications for the interpretation of ancient basin-fills. Mar. Pet. Geol. 11, 642–658. doi:10.1016/0264-8172(94)90021-3

Gawthorpe, R.L., Jackson, C.A.-L., Young, M.J., Sharp, I.R., Moustafa, A.R., Leppard, C.W., 2003. Normal fault growth, displacement localisation and the evolution of normal fault populations: the Hammam Faraun fault block, Suez rift, Egypt. J. Struct. Geol. 25, 883–895. doi:10.1016/S0191-8141(02)00088-3

Gawthorpe, R.L., Leeder, M., Kranis, H., Skourtsos, E., Andrews, J., Henstra, G., Mack, G., Muravchik, M., Turner, J., Stamatakis, M., 2017. Tectono-sedimentary evolution of the Plio-Pleistocene Corinth rift, Greece. Basin Research 30, 448–479.

Ghisetti, F., Vezzani, L., 1999. Depth and modes of Pliocene--Pleistocene crustal extension of the Apennines (Italy). Terra Nova 11, 67–72.

Gilbert, G.K., 1890. Lake Bonneville. US Government Printing Office.

Godano, M., Deschamps, A., Lambotte, S., Lyon-Caen, H., Bernard, P., Pacchiani, F., 2014. Focal mechanisms of earthquake multiplets in the western part of the Corinth Rift (Greece): influence of the velocity model and constraints on the geometry of the active faults. Geophys. J. Int. 197, 1660–1680. doi:10.1093/gji/ggu059

Goldsworthy, M., Jackson, J., 2001. Migration of activity within normal fault systems: examples from the Quaternary of mainland Greece. J. Struct. Geol. 23, 489–506.

Gueydan, F., Morency, C., Brun, J.-P., 2008. Continental rifting as a function of lithosphere mantle strength. Tectonophysics 460, 83–93. doi:10.1016/j.tecto.2008.08.012

Gupta, A., Scholz, C.H., 2000. A model of normal fault interaction based on observations and theory. J. Struct. Geol. 22, 865–879. doi:10.1016/s0191-8141(00)00011-0

Hatzfeld, D., Karakostas, V., Ziazia, M., Kassaras, I., Papadimitriou, E., Makropoulos, K., Voulgaris, N., Papaioannou, C., 2000. Microseismicity and faulting geometry in the Gulf of Corinth (Greece). Geophys. J. Int. 141, 438–456. doi:10.1046/j.1365-246x.2000.00092.x

Hemelsdaël, R., Ford, M., 2016. Relay zone evolution: a history of repeated fault propagation and linkage, central Corinth rift, Greece. Basin Res. 28, 34–56. doi:10.1111/bre.12101

Houghton, S.L., Roberts, G.P., Papanikolaou, I.D., McArthur, J.M., Gilmour, M.A., 2003. New 234U-230Th coral dates from the western Gulf of Corinth: Implications for extensional tectonics. Geophys. Res. Lett. 30, 2013. doi:10.1029/2003GL018112

Hubert-Ferrari, A., King, G., Armijo, R., Meyer, B., Papanastasiou, D., 1996. Fault re-activation, stress interaction and rupture propagation of the 1981 Corinth earthquake sequence. Earth Planet. Sci. Lett. 142, 573–585. doi:10.1016/0012-821X(96)00108-2

Hubert-Ferrari, A., King, G., Manighetti, I., Armijo, R., Meyer, B., Tapponnier, P., 2003. Long-term elasticity in the continental lithosphere; modelling the Aden Ridge propagation and the Anatolian extrusion process. Geophys. J. Int. 153, 111–132. doi:10.1046/j.1365-246x.2003.01872.x

Huguen, C., Mascle, J., Chaumillon, E., Kopf, A., Woodside, J., Zitter, T., 2004. Structural setting and tectonic control of mud volcanoes from the Central Mediterranean Ridge (Eastern Mediterranean). Marine Geology 209, 245–263. doi:10.1016/j.margeo.2004.05.002

Jackson, J.A., Gagnepain, J., Houseman, G., King, G.C.P., Papadimitriou, P., Soufleris, C., Virieux, J., 1982. Seismicity, normal faulting, and the geomorphological development of the Gulf of Corinth (Greece): the Corinth earthquakes of February and March 1981. Earth Planet. Sci. Lett. 57, 377–397. doi:10.1016/0012-821X(82)90158-3

Jackson, J., McKenzie, D., 1983. The geometrical evolution of normal fault systems. J. Struct. Geol. 5, 471–482. doi:10.1016/0191-8141(83)90053-6

Jacobshagen, V., Dürr, S., Kockel, F., Kopp, K.O., Kowalczyk, G., Berckhemer, H., Büttner, D., 1978. Structure and geodynamic evolution of the Aegean region. Alps, Apennines, Hellenides 38, 455–477.

Jamtveit, B., Ben-Zion, Y., Renard, F., Austrheim, H., 2018. Earthquake-induced transformation of the lower crust. Nature 556, 487–491. doi:10.1038/s41586-018-0045-y

Jolivet, L., 2001. A comparison of geodetic and finite strain pattern in the Aegean, geodynamic implications. Earth and Planetary Science Letters 187, 95–104. doi:10.1016/S0012-821X(01)00277-1

Jolivet, L., Brun, J.-P., 2010. Cenozoic geodynamic evolution of the Aegean. Int. J. Earth Sci. 99, 109–138. doi:10.1007/s00531-008-0366-4

Jolivet, L., Faccenna, C., Huet, B., Labrousse, L., Le Pourhiet, L., Lacombe, O., Lecomte, E., Burov, E., Denèle, Y., Brun, J.-P., Philippon, M., Paul, A., Salaün, G., Karabulut, H., Piromallo, C., Monié, P., Gueydan, F., Okay, A.I., Oberhänsli, R., Pourteau, A., Augier, R., Gadenne, L., Driussi, O., 2013. Aegean tectonics: Strain localisation, slab tearing and trench retreat. Tectonophysics 597–598, 1–33. doi:10.1016/j.tecto.2012.06.011

Jolivet, L., Labrousse, L., Agard, P., Lacombe, O., Bailly, V., Lecomte, E., Mouthereau, F., Mehl, C., 2010. Rifting and shallow-dipping detachments, clues from the Corinth Rift and the Aegean. Tectonophysics 483, 287–304. doi:10.1016/j.tecto.2009.11.001

Karymbalis, E., Ferentinou, M., Giles, P.T., 2016a. Use of morphometric variables and self-organizing maps to identify clusters of alluvial fans and catchments in the north Peloponnese, Greece. Geological Society, London, Special Publications 440. doi:10.1144/SP440.7

Karymbalis, E., Papanastassiou, D., Gaki-Papanastassiou, K., Ferentinou, M., Chalkias, C., 2016b. Late Quaternary rates of stream incision in Northeast Peloponnese, Greece. Front. Earth Sci. 10, 455–478. doi:10.1007/s11707-016-0577-0

Kent, E., Boulton, S.J., Whittaker, A.C., Stewart, I.S., Cihat Alçiçek, M., 2016. Normal fault growth and linkage in the Gediz (Alaşehir) Graben, Western Turkey, revealed by transient river long-profiles and slope-break knickpoints. Earth Surf. Processes Landforms. doi:10.1002/esp.4049

Keraudren, B., Sorel, D., 1987. The terraces of Corinth (Greece) — A detailed record of eustatic sea-level variations during the last 500,000 years. Mar. Geol. 77, 99–107. doi:10.1016/0025-3227(87)90085-5

King, G.C.P., Ouyang, Z.X., Papadimitriou, P., Deschamps, A., Gagnepain, J., Houseman, G., Jackson, J.A., Soufleris, C., Virieux, J., 1985. The evolution of the Gulf of Corinth (Greece): an aftershock study of the 1981 earthquakes. Geophys. J. Int. 80, 677–693. doi:10.1111/j.1365-246X.1985.tb05118.x

King, G., Ellis, M., 1990. The origin of large local uplift in extensional regions. Nature 348, 689–693.

King, G., Stein, R., Rundle, J., 1988. The Growth of Geological Structures by Repeated Earthquakes 1. Conceptual Framework. Journal of Geophysical Research: Solid Earth 93, 13307–13318. doi:10.1029/jb093ib11p13307

Koukouvelas, I.K., Aydin, A., 2002. Fault structure and related basins of the North Aegean Sea and its surroundings. Tectonics 21, 1046. doi:10.1029/2001TC901037

Koukouvelas, I.K., Stamatopoulos, L., Katsonopoulou, D., Pavlides, S., 2001. A palaeoseismological and geoarchaeological investigation of the Eliki fault, Gulf of Corinth, Greece. J. Struct. Geol. 23, 531–543. doi:10.1016/S0191-8141(00)00124-3

Kreemer, C., Chamot-Rooke, N., 2004. Contemporary kinematics of the southern Aegean and the Mediterranean Ridge. Geophysical Journal International 157, 1377–1392. doi:10.1111/j.1365-246X.2004.02270.x

Kusznir, N.J., Marsden, G., Egan, S.S., 1991. A flexural-cantilever simple-shear/pure-shear model of continental lithosphere extension: applications to the Jeanne d'Arc Basin, Grand Banks and Viking Graben, North Sea. Geological Society, London, Special Publications 56, 41–60.

Lacassin, R., Arnaud, N., Leloup, P.H., Armijo, R., Meyer, B., 2007. Syn- and post-orogenic exhumation of metamorphic rocks in North Aegean. eEarth 2, 51–63. doi:10.5194/ee-2-51-2007

Lajoie, K.R., 1986. Coastal tectonics. Active tectonics 95–124.

Lambotte, S., Lyon-Caen, H., Bernard, P., Deschamps, A., Patau, G., Nercessian, A., Pacchiani, F., Bourouis, S., Drilleau, M., Adamova, P., 2014. Reassessment of the rifting process in the Western Corinth Rift from relocated seismicity. Geophys. J. Int. 197, 1822–1844. doi:10.1093/gji/ggu096

Leeder, M.R., Mack, G.H., Brasier, A.T., Parrish, R.R., McIntosh, W.C., Andrews, J.E., Duermeijer, C.E., 2008. Late-Pliocene timing of Corinth (Greece) rift-margin fault migration. Earth Planet. Sci. Lett. 274, 132–141. doi:10.1016/j.epsl.2008.07.006

Leeder, M.R., Mark, D.F., Gawthorpe, R.L., Kranis, H., Loveless, S., Pedentchouk, N., Skourtsos, E., Turner, J., Andrews, J.E., Stamatakis, M., 2012. A "Great Deepening": Chronology of rift climax, Corinth rift, Greece. Geology 40, 999–1002. doi:10.1130/G33360.1

Leeder, M.R., Mc Neill, L.C., Ll Collier, R.E., Portman, C., Rowe, P.J., Andrews, J.E., Gawthorpe, R.L., 2003. Corinth rift margin uplift: New evidence from Late Quaternary marine shorelines. Geophysical Research Letters 30, 1611. doi:10.1029/2003GL017382

Leeder, M.R., Seger, M.J., Stark, C.P., 1991. Sedimentation and tectonic geomorphology adjacent to major active and inactive normal faults, southern Greece. J. Geol. Soc. London 148, 331–343. doi:10.1144/gsjgs.148.2.0331

Le Pichon, X., Angelier, J., 1981. The Aegean Sea. Philosophical Transactions of the Royal Society of London A: Mathematical, Physical and Engineering Sciences 300, 357–372.

Le Pichon, X., Kreemer, C., 2010. The Miocene-to-Present Kinematic Evolution of the Eastern Mediterranean and Middle East and Its Implications for Dynamics. Annu. Rev. Earth Planet. Sci. 38, 323–351. doi:10.1146/annurev-earth-040809-152419

Lister, G.S., Banga, G., Feenstra, A., 1984. Metamorphic core complexes of Cordilleran type in the Cyclades, Aegean Sea, Greece. Geology 12, 221–225. doi:2.0.CO;2">10.1130/0091-7613(1984)12<221:MCCOCT>2.0.CO;2

Lykousis, V., Sakellariou, D., Moretti, I., Kaberi, H., 2007. Late Quaternary basin evolution of the Gulf of Corinth: Sequence stratigraphy, sedimentation, fault–slip and subsidence rates. Tectonophysics 440, 29–51. doi:10.1016/j.tecto.2006.11.007

Lyon-Caen, H., Papadimitriou, P., Deschamps, A., Bernard, P., Makropoulos, K., Pacchiani, F., Patau, G., 2004. First results of the CRLN seismic network in the western Corinth Rift: evidence for old-fault reactivation. C. R. Geosci. 336, 343–351. doi:10.1016/j.crte.2003.12.004

Malartre, F., Ford, M., Williams, E.A., 2004. Preliminary biostratigraphy and 3D geometry of the Vouraikos Gilbert-type fan delta, Gulf of Corinth, Greece. C. R. Geosci. 336, 269–280. doi:10.1016/j.crte.2003.11.016

Manighetti, I., Campillo, M., Sammis, C., Mai, P.M., King, G., 2005. Evidence for self-similar, triangular slip distributions on earthquakes: Implications for earthquake and fault mechanics. J. Geophys. Res. 110, B05302. doi:10.1029/2004JB003174

Manighetti, I., King, G.C.P., Gaudemer, Y., Scholz, C.H., Doubre, C., 2001. Slip accumulation and lateral propagation of active normal faults in Afar. J. Geophys. Res. 106, 13667–13696. doi:10.1029/2000JB900471

Mats, V.D., 1993. The structure and development of the Baikal rift depression. Earth-Sci. Rev. 34, 81–118. doi:10.1016/0012-8252(93)90028-6

McKenzie, D., 1978. Active tectonics of the Alpine—Himalayan belt: the Aegean Sea and surrounding regions. Geophys. J. Int.

McKenzie, D., 1978a. Some remarks on the development of sedimentary basins. Earth and Planetary Science Letters 40, 25–32. doi:10.1016/0012-821X(78)90071-7

McKenzie, D., 1978. Active tectonics of the Alpine—Himalayan belt: the Aegean Sea and surrounding regions. Geophysical Journal International 55, 217–254.

McNeill, L.C., Collier, R.E.L., 2004. Uplift and slip rates of the eastern Eliki fault segment, Gulf of Corinth, Greece, inferred from Holocene and Pleistocene terraces. J. Geol. Soc. London 161, 81–92. doi:10.1144/0016-764903-029

McNeill, L.C., Cotterill, C.J., Henstock, T.J., Bull, J.M., Stefatos, A., Collier, R.E.L., Papatheoderou, G., Ferentinos, G., Hicks, S.E., 2005. Active faulting within the offshore western Gulf of Corinth, Greece: Implications for models of continental rift deformation. Geology 33, 241–244. doi:10.1130/G21127.1

McNeill, L.C., Shillington, D.J., Carter, G.D.O., Everest, J.D., Gawthorpe, R.L., Miller, C., Phillips, M.P., Ll. Collier, R.E., Cvetkoska, A., De Gelder, G., Diz, P., Doan, M.-L., Ford, M., Geraga, M., Gillespie, J., Hemelsdaël, R., Herrero-Bervera, E., Ismaiel, M., Janikian, L., Kouli, K., Le Ber, E., Li, S., Maffione, M., Mahoney, C., Machlus, M.L., Michas, G., Nixon, C.W., Oflaz, S.A., Omale, A.P., Panagiotopoulos, K., Pechlivanidou, S., Sauer, S., Seguin, J., Sergiou, S., Zakharova, N.V., Green, S., 2019. High-resolution record reveals climate-driven environmental and sedimentary changes in an active rift. Scientific Reports. doi:10.1038/s41598-019-40022-w

McNeill, L., Shillington, D., Carter, G., Everest, J., Green, S., 381 Scientists, E., 2018. Preliminary results from IODP Expedition 381: Development of the active Corinth Rift, Greece, EGU General Assembly Conference Abstracts. adsabs.harvard.edu.

Mechernich, S., Schneiderwind, S., Mason, J., Papanikolaou, I.D., Deligiannakis, G., Pallikarakis, A., Binnie, S.A., Dunai, T.J., Reicherter, K., 2018. The Seismic History of the Pisia Fault (Eastern Corinth Rift, Greece) From Fault Plane Weathering Features and Cosmogenic 36 Cl Dating. J. Geophys. Res. [Solid Earth] 123, 4266–4284. doi:10.1029/2017JB014600

Moretti, I., Lykousis, V., Sakellariou, D., Reynaud, J.-Y., Benziane, B., Prinzhoffer, A., 2004. Sedimentation and subsidence rate in the Gulf of Corinth: what we learn from the Marion Dufresne's long-piston coring. C. R. Geosci. 336, 291–299. doi:10.1016/j.crte.2003.11.011

Morley, C.K., 1989. Extension, detachments, and sedimentation in continental rifts (with particular reference to East Africa). Tectonics 8, 1175–1192. doi:10.1029/TC008i006p01175

Morrison, J., Anderson, J.L., 1998. Footwall refrigeration along a detachment fault: implications for the thermal evolution of core complexes. Science 279, 63–66.

Nixon, C.W., McNeill, L.C., Bull, J.M., Bell, R.E., Gawthorpe, R.L., Henstock, T.J., Christodoulou, D., Ford, M., Taylor, B., Sakellariou, D., Ferentinos, G., Papatheodorou, G., Leeder, M.R., Collier, R.E.L.I., Goodliffe, A.M., Sachpazi, M., Kranis, H., 2016. Rapid spatiotemporal variations in rift structure during development of the Corinth Rift, central Greece. Tectonics 35, 2015TC004026. doi:10.1002/2015TC004026

Ori, G.G., 1989. Geologic history of the extensional basin of the Gulf of Corinth (?Miocene-Pleistocene), Greece. Geology 17, 918–921. doi:2.3.CO;2">10.1130/0091-7613(1989)017<0918:GHOTEB>2.3.CO;2

Palyvos, N., Lemeille, F., Sorel, D., Pantosti, D., Pavlopoulos, K., 2008. Geomorphic and biological indicators of paleoseismicity and Holocene uplift rate at a coastal normal fault footwall (western Corinth Gulf, Greece). Geomorphology 96, 16–38. doi:10.1016/j.geomorph.2007.07.010

Palyvos, N., Pantosti, D., De Martini, P.M., Lemeille, F., Sorel, D., Pavlopoulos, K., 2005. The Aigion–Neos Erineos coastal normal fault system (western Corinth Gulf Rift, Greece): Geomorphological signature, recent earthquake history, and evolution. J. Geophys. Res. 110, B09302. doi:10.1029/2004JB003165

Palyvos, N., Pantosti, D., Zabci, C., D'Addezio, G., 2007. Paleoseismological Evidence of Recent Earthquakes on the 1967 Mudurnu Valley Earthquake Segment of the North Anatolian Fault Zone. Bull. Seismol. Soc. Am. 97, 1646–1661. doi:10.1785/0120060049

Pantosti, D., De Martini, P.M., Koukouvelas, I., Stamatopoulos, L., Palyvos, N., Pucci, S., Lemeille, F., Pavlides, S., 2004. Palaeoseismological investigations of the Aigion Fault (Gulf of Corinth, Greece). C. R. Geosci. 336, 335–342. doi:10.1016/j.crte.2003.12.005

Papazachos, C., Kiratzi, A., Papazachos, B., 1992. Rates of active crustal deformation in the Aegean and the surrounding area. Journal of Geodynamics 16, 147–179. doi:10.1016/0264-3707(92)90024-M

Pavlides, S.B., Koukouvelas, I.K., Kokkalas, S., Stamatopoulos, L., Keramydas, D., Tsodoulos, I., 2004. Late Holocene evolution of the East Eliki fault, Gulf of Corinth (Central Greece). Quaternary International 115–116, 139–154. doi:10.1016/S1040-6182(03)00103-4

Pearce, F.D., 2015. Seismic imaging of the western Hellenic subduction zone : the relationship between slab composition, retreat rate, and overriding lithosphere genesis. Massachusetts Institute of Technology Thesis.

Reilinger, R., McClusky, S., Paradissis, D., Ergintav, S., Vernant, P., 2009. Geodetic constraints on the tectonic evolution of the Aegean region and strain accumulation along the Hellenic subduction zone. Tectonophysics 488, 22–30. doi:10.1016/j.tecto.2009.05.027

Resor, P.G., Pollard, D.D., 2012. Reverse drag revisited: Why footwall deformation may be the key to inferring listric fault geometry. J. Struct. Geol. 41, 98–109. doi:10.1016/j.jsg.2011.10.012

Rietbrock, A., Tiberi, C., Scherbaum, F., Lyon-Caen, H., 1996. Seismic slip on a low angle normal fault in the Gulf of Corinth: Evidence from high-resolution cluster analysis of microearthquakes. Geophysical Research Letters 23, 1817–1820. doi:10.1029/96gl01257

Rigo, A., Lyon-Caen, H., Armijo, R., Deschamps, A., Hatzfeld, D., Makropoulos, K., Papadimitriou, P., Kassaras, I., 1996. A microseismic study in the western part of the Gulf of Corinth (Greece): Implications for large-scale normal faulting mechanisms. Geophys. J. Int. 126, 663–688.

Rohais, Joannin, Sébastien, Colin, J.-P., Suc, J.-P., Guillocheau, F., Eschard, R., 2007. Age and environmental evolution of the syn-rift fill of the southern coast of the gulf of Corinth (Akrata-Derveni region, Greece). Bulletin de la Société Géologique de France 178, 231–243. doi:10.2113/gssgfbull.178.3.231

Rohais, S., Eschard, R., Ford, M., Guillocheau, F., Moretti, I., 2007. Stratigraphic architecture of the Plio-Pleistocene infill of the Corinth Rift: Implications for its structural evolution. Tectonophysics 440, 5–28. doi:10.1016/j.tecto.2006.11.006

Rohais, S., Moretti, I., 2017. Structural and Stratigraphic Architecture of the Corinth Rift (Greece): An Integrated Onshore to Offshore Basin-Scale Synthesis, in: Roure, F., Amin, A.A., Khomsi, S., Al Garni, M.A.M. (Eds.), Lithosphere Dynamics and Sedimentary Basins of the Arabian Plate and Surrounding Areas, Frontiers in Earth Sciences. Springer International Publishing, pp. 89–120. doi:10.1007/978-3-319-44726-1_5

Rosenbloom, N.A., Anderson, R.S., 1994. Hillslope and channel evolution in a marine terraced landscape, Santa Cruz, California. J. Geophys. Res. 99, 14013–14029. doi:10.1029/94JB00048

Sachpazi, M., Clément, C., Laigle, M., Hirn, A., Roussos, N., 2003. Rift structure, evolution, and earthquakes in the Gulf of Corinth, from reflection seismic images. Earth Planet. Sci. Lett. 216, 243–257. doi:10.1016/S0012-821X(03)00503-X

Sachpazi, M., Galvé, A., Laigle, M., Hirn, A., Sokos, E., Serpetsidaki, A., Marthelot, J.-M., Pi Alperin, J.M., Zelt, B., Taylor, B., 2007. Moho topography under central Greece and its compensation by Pn time-terms for the accurate location of hypocenters: The example of the Gulf of Corinth 1995 Aigion earthquake. Tectonophysics 440, 53–65. doi:10.1016/j.tecto.2007.01.009

Sakellariou, D., Lykousis, V., Alexandri, S., Kaberi, H., Rousakis, G., Nomikou, P., Georgiou, P., Ballas, D., 2007. Faulting, seismic-stratigraphic architecture and Late Quaternary evolution of the Gulf of Alkyonides Basin–East Gulf of Corinth, Central Greece. Basin Res. 19, 273–295. doi:10.1111/j.1365-2117.2007.00322.x

Sakellariou, D., Lykousis, V., Papanikolaou, D., 1998. Neotectonic structure and evolution of the gulf of Alkyonides, central Greece. Bulletin of the Geologic Society of Greece 32, 241–250.

Scholz, C.H., Contreras, J.C., 1998. Mechanics of continental rift architecture. Geology 26, 967–970. doi:2.3.CO;2">10.1130/0091-7613(1998)026<0967:MOCRA>2.3.CO;2

Schwanghart, W., Scherler, D., 2014. TopoToolbox 2 – MATLAB-based software for topographic analysis and modeling in Earth surface sciences. Earth Surf. Dynam. 2, 1–7. doi:10.5194/esurf-2-1-2014

Scott, A.T., Pinter, N., 2003. Extraction of Coastal Terraces and Shoreline-Angle Elevations from Digital Terrain Models, Santa Cruz and Anacapa Islands, California. Phys. Geogr. 24, 271–294. doi:10.2747/0272-3646.24.4.271

Seger, M., Alexander, J., 2009. Distribution of Plio-Pleistocene and Modern Coarse-Grained Deltas South of the Gulf of Corinth, Greece, in: Frostick, L.E. (Ed.), Tectonic Controls and Signatures in Sedimentary Successions (Special Publication 20 of the IAS). John Wiley & Sons, p. 37.

Snyder, N.P., Whipple, K.X., Tucker, G.E., Merritts, D.J., 2000. Landscape response to tectonic forcing: Digital elevation model analysis of stream profiles in the Mendocino triple junction region, northern California. Geol. Soc. Am. Bull. 112, 1250–1263. doi:2.0.CO;2">10.1130/0016-7606(2000)112<1250:LRTTFD>2.0.CO;2

Sorel, D., 2000. A Pleistocene and still-active detachment fault and the origin of the Corinth-Patras rift, Greece. Geology 28, 83–86. doi:2.0.CO;2">10.1130/0091-7613(2000)28<83:APASDF>2.0.CO;2

Stefatos, A., Papatheodorou, G., Ferentinos, G., Leeder, M., Collier, R., 2002. Seismic reflection imaging of active offshore faults in the Gulf of Corinth: their seismotectonic significance. Basin Research 14, 487–502.

Stein, R.S., Barrientos, S.E., 1985. Planar high-angle faulting in the basin and range: Geodetic analysis of the 1983 Borah Peak, Idaho, earthquake. J. Geophys. Res., Publ. 90, 11355. doi:10.1029/JB090iB13p11355

Stewart, I., 1996. Holocene uplift and palaeoseismicity on the Eliki fault, Western Gulf of Corinth, Greece. Annals of Geophysics 39.

Stewart, I., Vita-Finzi, C., 1996. Coastal uplift on active normal faults: the Eliki Fault, Greece. Geophysical Research Letters 23, 1853–1856.

Taylor, B., Weiss, J.R., Goodliffe, A.M., Sachpazi, M., Laigle, M., Hirn, A., 2011. The structures, stratigraphy and evolution of the Gulf of Corinth rift, Greece: Structures, stratigraphy and evolution of GoC. Geophys. J. Int. 185, 1189–1219. doi:10.1111/j.1365-246X.2011.05014.x

Tetreault, J.L., Buiter, S.J.H., 2018. The influence of extension rate and crustal rheology on the evolution of passive margins from rifting to break-up. Tectonophysics 746, 155–172. doi:10.1016/j.tecto.2017.08.029

Tiberi, C., Diament, M., Lyon-Caen, H., King, T., 2001. Moho topography beneath the Corinth Rift area (Greece) from inversion of gravity data. Geophys. J. Int. 145, 797–808. doi:10.1046/j.1365-246x.2001.01441.x

Turner, J.A., Leeder, M.R., Andrews, J.E., Rowe, P.J., Van Calsteren, P., Thomas, L., 2010. Testing rival tectonic uplift models for the Lechaion Gulf in the Gulf of Corinth rift. J. Geol. Soc. London 167, 1237–1250. doi:10.1144/0016-76492010-035

van der Beek, P., 1997. Flank uplift and topography at the central Baikal Rift (SE Siberia): A test of kinematic models for continental extension. Tectonics 16, 122–136. doi:10.1029/96TC02686

Verrios, S., Zygouri, V., Kokkalas, S., 2004. Morphotectonic Analysis in the Eliki Fault Zone (Gulf of Corinth, Greece). Bulletin of the Geological Society of Greece 36, 1706–1715. doi:10.12681/bgsg.16578

Wallace, R.E., 1978. Geometry and rates of change of fault-generated range fronts, north-central Nevada. J. Res. US Geol. Surv 6, 637–650.

Walsh, J.J., Watterson, J., 1988. Analysis of the relationship between displacements and dimensions of faults. J. Struct. Geol. 10, 239–247. doi:10.1016/0191-8141(88)90057-0

Wernicke, B., 1981. Low-angle normal faults in the Basin and Range Province: nappe tectonics in an extending orogen. Nature 291, 645–648.

Whipple, K.X., Tucker, G.E., 1999. Dynamics of the stream-power river incision model: Implications for height limits of mountain ranges, landscape response timescales, and research needs. J. Geophys. Res: Solid Earth 104, 17661–17674.

Whittaker, A.C., Attal, M., Cowie, P.A., Tucker, G.E., Roberts, G., 2008. Decoding temporal and spatial patterns of fault uplift using transient river long profiles. Geomorphology 100, 506–526. doi:10.1016/j.geomorph.2008.01.018

Whittaker, A.C., Boulton, S.J., 2012. Tectonic and climatic controls on knickpoint retreat rates and landscape response times. J. Geophys. Res. 117, F02024. doi:10.1029/2011JF002157

Whittaker, A.C., Walker, A.S., 2015. Geomorphic constraints on fault throw rates and linkage times: Examples from the Northern Gulf of Evia, Greece. J. Geophys. Res. Earth Surf. 120, 2014JF003318. doi:10.1002/2014JF003318

Willemse, E.J.M., 1997. Segmented normal faults: Correspondence between three-dimensional mechanical models and field data. J. Geophys. Res. 102, 675–692. doi:10.1029/96JB01651

Wobus, C., Whipple, K.X., Kirby, E., Snyder, N., Johnson, J., Spyropolou, K., Crosby, B., Sheehan, D., 2006. Tectonics from topography: Procedures, promise, and pitfalls. Geological Society of America Special Papers 398, 55–74. doi:10.1130/2006.2398(04)

Zelt, B.C., Taylor, B., Sachpazi, M., Hirn, A., 2005. Crustal velocity and Moho structure beneath the Gulf of Corinth, Greece. Geophys. J. Int. 162, 257–268. doi:10.1111/j.1365-246X.2005.02640.x

Ziegler, P.A., 1988. Evolution of the Arctic-North Atlantic and the Western Tethys: A visual presentation of a series of Paleogeographic-Paleotectonic maps. AAPG Mem. 43, 164–196.

Supplementary Material

Supplementary Material A. Data integration into a new map

We used a composite Digital Elevation Model (DEM) with 20 m horizontal resolution onland and 50 m offshore to produce the topobathymetry. The onland DEM results from correcting the voids and gaps of a 30m-resolution AW3D30 DSM (ALOS) with 30m-resolution ASTER GDEM V2 (ASTER). We merged the result with commercial 20m-resolution SPOT5 DEM covering the southern and east sectors of the rift (inset in Fig. 6), and use a 50 m horizontally-resolved bathymetric data (Sakellariou et al., 2011) in the offshore. We manipulated the resulting composite DEM for several purposes. Firstly, we derive hypsometric contours, which are highlighted with darker colours every 500 m onland and 250 m offshore (Fig. 6). We also use the DEM to produce the stack swath profiles, analyse footwall topography and relief, and perform fluvial geomorphologic analyses.

Focal mechanisms of earthquakes with Mw > 5 since 1965 are shown and, whenever possible, scaled by their magnitude (Taymaz et al., 1991, and the references therein; Rigo et al., 1996; Taylor et al., 2011; Lambotte et al., 2014). The geologic map of Pliocene and younger rocks contains modifications from that of Armijo et al. (1996), which in turn is modified from Dufaure and Zamanis (1979) and Bornovas et al. (1983). We have improved the mapping of the basin in the west rift using the map of Bussolotto et al. (2015). The Hellenic units, regarded as basement for the purposes of this contribution, were also mapped (as in Taylor et al., 2011). To map active faults, we used a selection of onland faults mapped by other contributions (Dart et al., 1994; Armijo et al., 1996; De Martini et al., 2004; McNeill and Collier, 2004; Palyvos et al., 2005; Sakellariou et al., 2007; Maroukian et al., 2008; Roberts et al., 2009; Jolivet et al., 2010; Lambotte et al., 2014; Beckers et al., 2015; Ford et al., 2016; Karymbalis et al., 2016b), and own mapping, using our composite DEM, SPOT images and fieldwork.

We used available reflection seismic lines (McNeill et al., 2005; Sakellariou et al., 2007; Bell et al., 2008, 2009; Taylor et al., 2011; Charalampakis et al., 2014; Lambotte et al., 2014; Beckers et al., 2015; Bussolotto et al., 2015) to create the offshore fault map. Fault selection, remapping and hierarchy are based on fault activity during the Holocene. We identify fault activity in the onshore faults on the basis of the presence of a topographic offset and for the offshore faults, we used seafloor offset or presence of a fault tip close to the seafloor. With the aforementioned means, we produce a 5-level fault hierarchy at the scale of the whole rift, based on relief difference on both sides of the fault and expressed as distinctive stroke

thickness in the fault traces (Figs. 6 & 8). We also mapped numerous known faults without topographic expression, i.e. no Holocene activity, that are commonly mapped in studies of the area. We classified them as 4th or 5th level depending on the cross-consistency (both in the presence and position) of their mapping by those contributions. Comparison with the detailed offshore fault mapping based on the reinterpretation of seismic data presented in Nixon et al. (2016) leads to overall satisfactory levels of agreement. Departures come from our different consideration of what constitutes an "active" fault (Suppl. material B).

We also mapped the topsets of the perched Gilbert-type deltas using available stratigraphic maps (Dart et al., 1994; Rohais et al., 2007; Backert et al., 2010; Ford et al., 2016), satellite imagery and Google Earth (Fig. 6). In the case of Akrata and Aigio, where the topsets of the Gilbert deltas are not clearly distinguished from marine terrace levels, we mapped the topsets as the upper marine terrace level. Some known deltaic bodies that have not mappable topsets, or topsets that are difficult to discern from levels of marine terraces were not mapped. Mapping of the alluvial fans and present deltas is based on Karymbalis et al. (2016a) and Ford et al. (2016) (Fig. 6).

We use the marine terraces of De Gelder et al. (2018) mapped from a 2m-resolution DEM derived from Pleiades tri-stereo satellite imagery (De Gelder et al., 2015) using MicMac software (Rosu et al., 2015). This map of marine terraces covers a relevant coastal area in the southeast rift margin (De Gelder et al., 2019) and marine terraces mapped outside of this area were redrawn to adapt the objects for better fits with the slope and hillshade maps (Armijo et al., 1996; Houghton et al., 2003; De Martini et al., 2004; McNeill and Collier, 2004; Andrews et al., 2007; Maroukian et al., 2008; Roberts et al., 2009).

River drainages of each catchment were manually mapped tracing ridges by means of 5 m equal-height contour lines derived from our 20-m resolution DEM. Windgaps and traces of the paleo-river network were also mapped by these means at some locations, but are not systematically mapped throughout the rift. The river networks were obtained with TopoToolbox 2.0 (Schwanghart and Scherler, 2014), and the result was modified manually for larger accuracy and aesthetic reasons in the flat regions of the internally drained basins of Feneos, Stymfalia and Skotini.

Supplementary Material B. Comparison of offshore fault maps in the Corinth Rift

In a recent effort, Nixon et al. (2016) compiled and reinterpreted a large data set of reflection seismic data into an offshore fault map of the rift. Our map of active faults in the offshore is overall in very good agreement with their fault map, with the exception of three areas of mismatch. Probably the most important mismatch is that in Nixon et al. (2016)'s contribution considers the Derveni Fault and Lykoporia Fault as the "switching point" between the pure N-S western part and the ENE-WSW eastern part of the rift. Such a change in fault orientation is not questionable, but we are dubitative about its location during Holocene times, given that the eastern end of Derveni Fault, as Nixon et al. (2016) mapped it, would cut several isopachs in a Holocene depocenter map (Watkins et al., 2018) without appreciable depocenter localization. Our map suggests that this fault has a better alignment with the Lykoporia Fault to the east, at least for Quaternary times. Similarly, Nixon et al. (2016) mapped significant faults in the northern sector of the gulf, behind the main antithetic faults, in what they named Central West and Central East sectors. Although these faults show some displacements in their Nixon et al. (2016)'s Fig. 5, they have no expression in the seafloor. Moreover, these faults have no associated depocenter in Holocene times (Watkins et al., 2018), and thus are not mapped in our contribution. Finally, we found discrepancies in the trends of the faults around the islands in the Alkyonides Gulf, striking roughly either E-W (Nixon et al., 2016) or ENE-WSW (this contribution). We keep our original interpretation for faults with Holocene activity, since their orientation is agreement with the elongation of the islands in the Alkyonides Gulf, as well as with the bathymetry, and with a Holocene depocenter map (Watkins et al., 2018).

Supplementary Material C. Analysis of topobathymetry with stacked swaths

Topography-based morphotectonic evidence provides a first-order understanding of the degree and time-scale of activity of contributing structures in settings where tectonic forcing outpaces climatic and erosive factors (e.g., Armijo et al., 1986; Klinger et al., 2000; Densmore et al., 2004). Stacked swath profiles now allow for topographic assessment at the scale of large, orogen-scale objects. Armijo et al. (2015) originally used stacked swath profiles to illustrate the major morphological features of the Central Andes coastal margin, an exercise either difficult or entirely impossible with other means.

A stacked swath profile contains a significant number of consecutive parallel swath profiles derived from topographic data, commonly Digital Elevation Models (DEMs), plot together as hairlines orthogonally to their strike. By stacking swath profiles, the resulting profile highlights a "2.5D" view of topographic coherence in depth, allowing the distinction of large-scale structural and morphological features that are continuous over large scales. Stacked swath profiles in this contribution are produced as a pile of parallel swath profiles of dynamically defined width. Swath width is the result of dividing DEM width along the projection line by chosen number of swaths.

Three stacked swath profiles show the topobathymetry across the central and west rift (Fig. 10), from the southern shoulder drainage divide to passed the northern margin coast. Each stacked swath looks westwards perpendicular to the strike of particular fault segments (Fig. 7), i.e. Central Rift FA, Eliki FA, and Aigio FA (A, B & C in Fig. 10). Overall perpendicular to the aforementioned stacked swaths, each of the three stacked swath profiles providing a view along the rift southern shoulder (Fig. 11) extents from Loutraki to Psathopyrgos, looking towards the fault front roughly to the SSW (Fig. 7). The stacked swath profiles cover the topography of the entire drainage divide, the topography at ~21 km of the bounding fault, and the bathymetry until further north than the deepest basin floor (A, B and C in Fig. 11).
Two stacked swath profiles show the topography and one the bathymetry of the Corinth Rift southern flank in a view parallel to the border fault (Fig. 11). Each stacked swath spans from Loutraki to Psathopyrgos looking towards the fault front roughly to the SSW (Fig. 7 for reference), including the relief of southern shoulder drainage divide, and that within ~21 km of the rift-bounding fault ("fault-related" relief - see Suppl. material E), and the rift bathymetry, until further north than the deepest basin floor (A, B and C in Fig. 11).

Supplementary Material D. Analysis of detachment-limited river long profiles

Research attests that rock uplift rate or erosion rate are functionally related to river channel steepness, when normalized by upstream contributing drainage area (e.g., Snyder et al., 2000; DiBiase et al., 2010). This suggests that the relative rate of uplift or erosion can be approximated to river channel steepness, a relationship that can be described theoretically by quasi-physical stream power incision model (e.g., Howard, 1994). The detachment-limited stream power incision model describes river bed elevation change in time (dz/dt) as a function of upstream drainage area ($\propto$ discharge) (Whipple and Tucker, 1999; Tucker and Whipple, 2002) and local channel slope. Combined with mass conservation it takes the form of

$$dz/dt = U \cdot E = U - K \cdot A^m \cdot S^n \, .$$

Assuming that rock-uplift (U) and erosion rate (E) are equal leads to a local channel slope (S) defined by

$$S = (U/K)^{1/n} \cdot A^{-(m/n)},$$

A being the drainage area upstream, K a dimensional coefficient that encloses incision, substrate, climate and hydrology of erosion (e.g., Whipple, 2004), and m and n positive constants dependent on channel geometry, basin hydrology, and erosion processes (Howard, 1994; Whipple and Tucker, 1999; Whipple, 2004).

Supplementary Material E. Footwall relief calculus, errors and uncertainties

We analyse the along-strike distribution of footwall relief deriving the position of the first topographic break of slope in footwall topography (in a similar fashion than Whittaker and Walker, 2015). We calculated the envelope of footwall relief projecting 20-m resolution DEM data perpendicularly towards the bounding fault along its strike. For that, we defined a polygon of ~21 km measured inland orthogonally to the strike of each fault segment (Fig. 7) with the aim of covering the area of the topographic break-of-slope (sited <20km, often ~15km). We use a ~20m-wide topographic swath every 20 m perpendicular to the fault trace (~5000 in total), and project the footwall relief along fault strike. For the west rift, where the trace of the bounding faults can be mapped with confidence and errors are minimal, we calculated three trends in footwall relief, corresponding to the three different strikes of their respective fault arrays (Fig. 15; East Eliki in red, N095°E; West Eliki in blue, N105°E; Aigio in green, N120°E). We then used N105°E to calculate the footwall relief over the entire southern shoulder (Fig. 16).

We minimized errors related with the DEMs, but other uncertainties were not avoidable. We graphically attach an estimated uncertainty derived from two factors: confidence in accurate mapping of the fault and discrepancy between fault strike and chosen direction of projection (Figs. 7 & 13). The discrepancy between projection plane, representing the average fault strike, and the real fault strike is neglectable in the western rift, and increases for the central rift, where we estimate a maximum associated uncertainty of ±50 m in the vertical that is not explicitly shown in the figures. A second uncertainty exist in the calculus of the footwall relief derived from potential inaccuracies in the position of the fault trace, which are minimal in the west rift, and increase eastwards where the fault lays underwater (Fig. 6). We estimate a maximum uncertainty of ±250 m in the vertical for the central rift due to this effect, in combination with the unconstrained behavior of the footwall relief sector that grows underwater. Farther east than Kiato town, the departure of the bounding fault basinward away from the coast (Fig. 6) results in uncertainties that are difficult to estimate, and we performed no calculus. With this exception, we are confident that the tectonic signal significantly overpasses the uncertainties at the scale of interest.

Supplementary Material F. Reconstruction of vertical motions in time: Data constraints and manipulation, errors and uncertainties

Time constraints are based on the sea level highstands MIS 5e (124 ka), MIS 7e (240 ka), MIS 9e (326 ka) for the marine terraces paleoshoreline angles. Ages assigned for the foreset-topset contacts of Gilbert deltas are uncertain as they lack absolute dating (e.g., Gawthorpe et al., 2017b) and are based on disputed correlations (cf. Ford et al., 2016; Rohais and Moretti, 2017). For foreset-topset contacts of Pleistocene Gilbert deltas, we used a ~700 ka age proposed in Ford et al. (2016) for the abandonment by footwall uplift of the Middle Group deltas. We include in this group the Kolokotronis and Klimenti deltas, of potentially different age, to avoid effects in relation to the location of deltas with respect to the master fault (see Gawthorpe et al., 2017a). The age of the Mavro Gilbert delta is also disputed. We set the age of abandonment of the foreset-topset contact of Mavro to ~1 Ma (as in Armijo et al., 1996), although a significantly wider age bracket (1-2 Ma) is plausible. See details leading to this choice on section 3.1.

In this review, we project coeval morphotectonic markers of the southern rift margin (Fig. 13) towards the strike of the bounding fault(s). For the paleoshoreline angles of marine terraces, we follow Railsback et al. (2015) nomenclature for sea level highstands and Masson-Delmotte et al.(2010) for highstand ages, i.e. MIS 5e (~124 ka), MIS 7e (~240 ka) and MIS 9e (~326 ka). Paleoshoreline angles belong to time-correlated and/or dated marine terraces with maximum heights at six locations close to the bounding fault(s) (e.g., Houghton et al., 2003; De Martini et al., 2004; McNeill and Collier, 2004; De Gelder et al., 2019) (Fig. 6 & 7), and the ages of Gilbert-type deltas come from Ford et al. (2016).

In the eastern locations of Xy1 and Xy2, paleoshoreline angles of the same sea level highstands lay at considerably different elevations and distances from the main fault (e.g., Armijo et al., 1996). The easternmost location, Xy1 lays at lower elevations and farther from the bounding fault than any other paleoshoreline angle (Figs. 6, 9A & 17, Table 3). At Xy2, we used the MIS 5e level closest to the main fault and obtained the elevations of MIS 7e and MIS 9e that lay above it using best-fitting quadratic curves of extrapolated shoreline angles further away from the fault (as in De Gelder et al., 2019). Red circles are MIS 9e at Xy1, Xy2 and Ps, and an undifferentiated MIS 9 in other locations (Fig. 17).

For the reconstructions in Figs. 18A & 19A, we represent the position of the Gilbert deltas topset-foreset contact as a single point calculated as the average, both in the vertical and the horizontal, of the points in Fig. 17. We calculated the relative uplift rate of paleo-

shoreline angles of flights of marine terraces at our six chosen locations (Fig. 18B; Table 3). To aid comparison among fault vertical motions, we reduce to one third the height difference calculated for markers uplifting from ~700 ka to 326 ka, and ~1 Ma to ~700 ka, i.e. we maintain time-steps of approx. 110 ka. We also put forward an estimation of paleo-relief before bounding fault formation (blue lines in Fig. 18A), subtracting the envelopes of maximum relief within the south rift margin drainage and within ~21 km from the bounding fault (Figs. 7 & 11), after simplifying both surfaces. In this rough reconstruction of paleo-relief, maximum and minimum paleo-relief envelopes connect local highs and lows respectively purposely neglecting details of the relict relief. We note that the different distances from these relief envelopes to the bounding fault, as well as the effects of erosion and denudation neglected in this comparison may add a few hundred meters of uncertainty. Accounting for these corrections would invariably lead to larger paleo-reliefs, and thus we consider the paleo-relief estimation with care and as a minimum.

Reconstruction based on the marine terraces may be complicated by the interplay between depositional and erosional terraces, and the lack of accurate dating, given that most ages are inferred. Similarly, reconstruction based on the foreset-topsets Gilbert delta contacts have reduced levels of accuracy. Errors may exist in relation to Gilbert delta assigned age, cartography and vertical variations in the position of their foreset-topset boundary. We estimate that the associated uncertainty ranges between 5% and 20%, but we performed no specific quantification. Similarly, we also note that, for most cases, marine terraces are located closer to the bounding fault than delta fans, and thus, under the same fault slip rates, inferred rates of vertical motions for the deltas will be comparatively lower. Despite the aforementioned potential errors and uncertainties, we expect an accurate relative timing of events and satisfactory levels of precision in overall trends at the scale considered.

Supplementary Material G to K. Shapefiles and KML files

We provide shapefiles and KML files of topobathymetric DEM (Suppl. material G), active faults at 5-level hierarchy (Suppl. material H), marine terraces (Suppl. material I), Gilbert-delta topsets (Suppl. material J), and river streams and their catchments (Suppl. material K).

Supplementary data to this article can be found online at
https://doi.org/10.1016/j.earscirev.2019.102919
or by getting in contact with the main author at
geo.david.fernandez@gmail.com

Supplementary Material References

Andrews, J.E., Portman, C., Rowe, P.J., Leeder, M.R., Kramers, J.D., 2007. Sub-orbital sea-level change in early MIS 5e: New evidence from the Gulf of Corinth, Greece. Earth Planet. Sci. Lett. 259, 457–468.

Armijo, R., Lacassin, R., Coudurier-Curveur, A., Carrizo, D., 2015. Coupled tectonic evolution of Andean orogeny and global climate. Earth-Sci. Rev. 143, 1–35.

Armijo, R., Meyer, B., King, G.C.P., Rigo, A., Papanastassiou, D., 1996. Quaternary evolution of the Corinth Rift and its implications for the Late Cenozoic evolution of the Aegean. Geophysical Journal International 126, 11–53.

Armijo, R., Tapponnier, P., Mercier, J.L., Han, T.-L., 1986. Quaternary extension in southern Tibet: Field observations and tectonic implications. J. Geophys. Res. 91, 13803–13872.

Backert, N., Ford, M., Malartre, F., 2010. Architecture and sedimentology of the Kerinitis Gilbert-type fan delta, Corinth Rift, Greece. Sedimentology 57, 543–586.

Beckers, A., Hubert-Ferrari, A., Beck, C., Bodeux, S., Tripsanas, E., Sakellariou, D., De Batist, M., 2015. Active faulting at the western tip of the Gulf of Corinth, Greece, from high-resolution seismic data. Mar. Geol. 360, 55–69.

Bell, R.E., McNeill, L.C., Bull, J.M., Henstock, T.J., 2008. Evolution of the offshore western Gulf of Corinth. Geol. Soc. Am. Bull. 120, 156–178.

Bell, R.E., Mc Neill, L.C., Bull, J.M., Henstock, T.J., Collier, R.E.L., Leederz, M.R., 2009. Fault architecture, basin structure and evolution of the Gulf of Corinth Rift, central Greece. Basin Res. 21, 824–855.

Bornovas, J., Rondogianni-Tsiambaou, T., kai Metalleutikōn Ereunōn, A.I.G., 1983. [Geological map of Greece 1: 500000]; Geōlogikos chartēs tēs Ellados. IGME.

Bussolotto, M., Benedicto, A., Moen-Maurel, L., Invernizzi, C., 2015. Fault deformation mechanisms and fault rocks in micritic limestones: Examples from Corinth rift normal faults. J. Struct. Geol. 77, 191–212.

Charalampakis, M., Lykousis, V., Sakellariou, D., Papatheodorou, G., Ferentinos, G., 2014. The tectono-sedimentary evolution of the Lechaion Gulf, the south eastern branch of the Corinth graben, Greece. Mar. Geol. 351, 58–75.

Dart, C.J., Collier, R.E.L., Gawthorpe, R.L., Keller, J.V.A., Nichols, G., 1994. Sequence stratigraphy of (?)Pliocene-Quaternary synrift, Gilbert-type fan deltas, northern Peloponnesos, Greece. Mar. Pet. Geol. 11, 545–560.

De Gelder, G., Fernández-Blanco, D., Lacassin, R., Armijo, R., Delorme, A., Jara-Muñoz, J., Melnick, D., 2015. Corinth terraces re-visited: Improved paleoshoreline determination using Pleiades-DEMs. Geotectonic Research 97, 12–14.

De Gelder, G., Fernández-Blanco, D., Melnick, D., Duclaux, G., Bell, R.E., Jara-Muñoz, J., Armijo, R., Lacassin, R., 2019. Lithospheric flexure and rheology determined by climate cycle markers in the Corinth Rift. Sci. Rep. 9, 4260.

De Martini, P.M., Pantosti, D., Palyvos, N., Lemeille, F., McNeill, L., Collier, R., 2004. Slip rates of the Aigion and Eliki Faults from uplifted marine terraces, Corinth Gulf, Greece. C. R. Geosci. 336, 325–334.

Densmore, A.L., Dawers, N.H., Gupta, S., Guidon, R., Goldin, T., 2004. Footwall topographic development during continental extension. J. Geophys. Res. 109, F03001.

DiBiase, R.A., Whipple, K.X., Heimsath, A.M., Ouimet, W.B., 2010. Landscape form and millennial erosion rates in the San Gabriel Mountains, CA. Earth Planet. Sci. Lett. 289, 134–144.

Dufaure, J.-J., Zamanis, A., 1979. Un vieux problème géomorphologique: les niveaux bordiers au sud du Golfe de Corinthe (An old geomorphological problem: the levels developed on the southern border of the gulf of Corinth). Bulletin de l'Association de géographes français 56, 341–350.

Ford, M., Hemelsdaël, R., Mancini, M., Palyvos, N., 2016. Rift migration and lateral propagation: evolution of normal faults and sediment-routing systems of the western Corinth rift (Greece). Geological Society, London, Special Publications 439. doi:10.1144/SP439.15

Gawthorpe, R.L., Andrews, J.E., Collier, R.E.L., Ford, M., Henstra, G.A., Kranis, H., Leeder, M.R., Muravchik, M., Skourtsos, E., 2017a. Building up or out? Disparate sequence architectures along an active rift margin—Corinth rift, Greece. Geology 45, 1111–1114.

Gawthorpe, R.L., Leeder, M., Kranis, H., Skourtsos, E., Andrews, J., Henstra, G., Mack, G., Muravchik, M., Turner, J., Stamatakis, M., 2017b. Tectono-sedimentary evolution of the Plio-Pleistocene Corinth rift, Greece. Basin Res.

Houghton, S.L., Roberts, G.P., Papanikolaou, I.D., McArthur, J.M., Gilmour, M.A., 2003. New 234U-230Th coral dates from the western Gulf of Corinth: Implications for extensional tectonics. Geophys. Res. Lett. 30, 2013.

Howard, A.D., 1994. A detachment-limited model of drainage basin evolution. Water Resour. Res. 30, 2261–2285.

Jolivet, L., Labrousse, L., Agard, P., Lacombe, O., Bailly, V., Lecomte, E., Mouthereau, F., Mehl, C., 2010. Rifting and shallow-dipping detachments, clues from the Corinth Rift and the Aegean. Tectonophysics 483, 287–304.

Karymbalis, E., Ferentinou, M., Giles, P.T., 2016a. Use of morphometric variables and self-organizing maps to identify clusters of alluvial fans and catchments in the north Peloponnese, Greece. Geological Society, London, Special Publications 440. doi:10.1144/SP440.7

Karymbalis, E., Papanastassiou, D., Gaki-Papanastassiou, K., Ferentinou, M., Chalkias, C., 2016b. Late Quaternary rates of stream incision in Northeast Peloponnese, Greece. Front. Earth Sci. 10, 455–478.

Klinger, Y., Avouac, J.P., Abou Karaki, N., Dorbath, L., Bourles, D., Reyss, J.L., 2000. Slip rate on the Dead Sea transform fault in northern Araba valley (Jordan). Geophys. J. Int. 142, 755–768.

Lambotte, S., Lyon-Caen, H., Bernard, P., Deschamps, A., Patau, G., Nercessian, A., Pacchiani, F., Bourouis, S., Drilleau, M., Adamova, P., 2014. Reassessment of the rifting process in the Western Corinth Rift from relocated seismicity. Geophys. J. Int. 197, 1822–1844.

Maroukian, H., Gaki-Papanastassiou, K., Karymbalis, E., Vouvalidis, K., Pavlopoulos, K., Papanastassiou, D., Albanakis, K., 2008. Morphotectonic control on drainage network evolution in the Perachora Peninsula, Greece. Geomorphology 102, 81–92.

Masson-Delmotte, V., Stenni, B., Pol, K., Braconnot, P., Cattani, O., Falourd, S., Kageyama, M., Jouzel, J., Landais, A., Minster, B., Barnola, J.M., Chappellaz, J., Krinner, G., Johnsen, S., Röthlisberger, R., Hansen, J., Mikolajewicz, U., Otto-Bliesner, B., 2010. EPICA Dome C record of glacial and interglacial intensities. Quat. Sci. Rev. 29, 113–128.

McNeill, L.C., Collier, R.E.L., 2004. Uplift and slip rates of the eastern Eliki fault segment, Gulf of Corinth, Greece, inferred from Holocene and Pleistocene terraces. J. Geol. Soc. London 161, 81–92.

McNeill, L.C., Cotterill, C.J., Henstock, T.J., Bull, J.M., Stefatos, A., Collier, R.E.L., Papatheoderou, G., Ferentinos, G., Hicks, S.E., 2005. Active faulting within the offshore western Gulf of Corinth, Greece: Implications for models of continental rift deformation. Geology 33, 241–244.

Nixon, C.W., McNeill, L.C., Bull, J.M., Bell, R.E., Gawthorpe, R.L., Henstock, T.J., Christodoulou, D., Ford, M., Taylor, B., Sakellariou, D., Ferentinos, G., Papatheodorou, G., Leeder, M.R., Collier, R.E.L.I., Goodliffe, A.M., Sachpazi, M., Kranis, H., 2016. Rapid spatiotemporal variations in rift structure during development of the Corinth Rift, central Greece. Tectonics 35, 2015TC004026.

Palyvos, N., Pantosti, D., De Martini, P.M., Lemeille, F., Sorel, D., Pavlopoulos, K., 2005. The Aigion–Neos Erineos coastal normal fault system (western Corinth Gulf Rift, Greece): Geomorphological signature, recent earthquake history, and evolution. J. Geophys. Res. 110, B09302.

Rigo, A., Lyon-Caen, H., Armijo, R., Deschamps, A., Hatzfeld, D., Makropoulos, K., Papadimitriou, P., Kassaras, I., 1996. A microseismic study in the western part of the Gulf of Corinth (Greece): Implications for large-scale normal faulting mechanisms. Geophys. J. Int. 126, 663–688.

Roberts, G.P., Houghton, S.L., Underwood, C., Papanikolaou, I., Cowie, P.A., van Calsteren, P., Wigley, T., Cooper, F.J., McArthur, J.M., 2009. Localization of Quaternary slip rates in an active rift in 10 5 years: An example from central Greece constrained by 234 U- 230 Th coral dates from uplifted paleoshorelines. J. Geophys. Res. 114, 393.

Rohais, S., Eschard, R., Ford, M., Guillocheau, F., Moretti, I., 2007. Stratigraphic architecture of the Plio-Pleistocene infill of the Corinth Rift: Implications for its structural evolution. Tectonophysics 440, 5–28.

Rohais, S., Moretti, I., 2017. Structural and stratigraphic architecture of the Corinth Rift (Greece): An integrated onshore to offshore basin-scale synthesis, in: Roure, F., Amin, A.A., Khomsi, S., Al Garni,

M.A.M. (Eds.), Lithosphere Dynamics and Sedimentary Basins of the Arabian Plate and Surrounding Areas, Frontiers in Earth Sciences. Springer International Publishing, Cham, pp. 89–120.

Rosu, A.-M., Pierrot-Deseilligny, M., Delorme, A., Binet, R., Klinger, Y., 2015. Measurement of ground displacement from optical satellite image correlation using the free open-source software MicMac. ISPRS J. Photogramm. Remote Sens. 100, 48–59.

Sakellariou, D., Lykousis, V., Alexandri, S., Kaberi, H., Rousakis, G., Nomikou, P., Georgiou, P., Ballas, D., 2007. Faulting, seismic-stratigraphic architecture and Late Quaternary evolution of the Gulf of Alkyonides Basin–East Gulf of Corinth, Central Greece. Basin Res. 19, 273–295.

Sakellariou, D., Lykousis, V., Rousakis, G., 2011. Holocene seafloor faulting in the Gulf of Corinth: The potential for underwater paleoseismology. 2nd INQUA-IGCP-567 International Workshop on Active Tectonics, Earthquake Geology, Archaeology and Engineering. Corinth, Greece.

Schwanghart, W., Scherler, D., 2014. TopoToolbox 2 – MATLAB-based software for topographic analysis and modeling in Earth surface sciences. Earth Surf. Dynam. 2, 1–7.

Snyder, N.P., Whipple, K.X., Tucker, G.E., Merritts, D.J., 2000. Landscape response to tectonic forcing: Digital elevation model analysis of stream profiles in the Mendocino triple junction region, northern California. Geol. Soc. Am. Bull. 112, 1250–1263.

Taylor, B., Weiss, J.R., Goodliffe, A.M., Sachpazi, M., Laigle, M., Hirn, A., 2011. The structures, stratigraphy and evolution of the Gulf of Corinth rift, Greece: Structures, stratigraphy and evolution of GoC. Geophys. J. Int. 185, 1189–1219.

Taymaz, T., Jackson, J., McKenzie, D., 1991. Active tectonics of the north and central Aegean Sea. Geophysical Journal International 106, 433–490.

Tucker, G.E., Whipple, K.X., 2002. Topographic outcomes predicted by stream erosion models: Sensitivity analysis and intermodel comparison. J. Geophys. Res. 107, 2179.

Watkins, S.E., Whittaker, A.C., Bell, R.E., McNeill, L.C., Gawthorpe, R.L., Brooke, S.A.S., Nixon, C.W., 2018. Are landscapes buffered to high-frequency climate change? A comparison of sediment fluxes and depositional volumes in the Corinth Rift, central Greece, over the past 130 k.y. Geological Society of America Bulletin. doi:10.1130/B31953.1

Whipple, K.X., 2004. Bedrock rivers and the geomorphology of active orogens. Annu. Rev. Earth Planet. Sci. 32, 151–185.

Whipple, K.X., Tucker, G.E., 1999. Dynamics of the stream-power river incision model: Implications for height limits of mountain ranges, landscape response timescales, and research needs. J. Geophys. Res: Solid Earth 104, 17661–17674.

Whittaker, A.C., Walker, A.S., 2015. Geomorphic constraints on fault throw rates and linkage times: Examples from the Northern Gulf of Evia, Greece. J. Geophys. Res. Earth Surf. 120, 2014JF003318.